Reflective optics-based line-scanning spectral domain optical coherence tomography system

Mohammad Abu Hana Mustafa Kamal

A Thesis
In the Department
of
Mechanical and Industrial Engineering

Presented in Partial Fulfillment of the Requirements
For the Degree of
Doctor of Philosophy (Mechanical and Industrial Engineering) at
Concordia University
Montreal, Quebec, Canada

September 2011

CONCORDIA UNIVERSITY
SCHOOL OF GRADUATE STUDIES

This is to certify that the thesis prepared

By: **Mohammad Abu Hana Mustafa Kamal**

Entitled: **Reflective optics-based line-scanning spectral domain optical coherence tomography system**

and submitted in partial fulfillment of the requirements for the degree of

DOCTOR OF PHILOSOPHY (Mechanical Engineering)

complies with the regulations of the University and meets the accepted standards with respect to originality and quality.

Signed by the final examining committee:

______________________________________Chair
Dr. J.X. Zhang
______________________________________ External Examiner
Dr. K. Venkatakrishnan
______________________________________ External to Program
Dr. A. Bagchi
______________________________________ Examiner
Dr. R. Sedaghati
______________________________________ Examiner
Dr. R. Wuthrich
______________________________________Thesis Co-Supervisor
Dr. S. Narayanswamy
______________________________________Thesis Co-Supervisor
Dr. M. Packirisamy

Approved by
Dr. W-F. Xie, Graduate Program Director

September 2, 2011 ______________________________________
Dr. Robin A.L. Drew, Dean
Faculty of Engineering & Computer Science

ABSTRACT

Reflective optics-based line-scanning spectral domain optical coherence tomography system

Mohammad Abu Hana Mustafa Kamal, Ph.D.

Concordia University, 2011

Optical Coherence Tomography (OCT) is a high-resolution non-invasive and non-contact imaging technology. Traditionally, multi-axis spot-focused scanning is used for transverse scanning to obtain a two or three-dimensional OCT image. This increases the time to acquire an image and imaging performance is affected by motion artifacts. Moreover, lenses are used in the *state-of-the-art* OCT systems that reduce the axial resolution due to chromatic aberration, and affect the imaging quality due to distorted scan field.

In order to avoid the problems mentioned above, the objective of the present thesis is to develop a reflective optics-based line-scan spectral domain OCT system for high-quality three-dimensional imaging. Cylindrical mirror used in this thesis for focusing eliminates chromatic aberration and provides a flat scan field. Line scanning reduces the requirement of scanning to one axis and thereby making the image acquisition faster. A novel reflective optics based line-scanning system with a spectrometer has been designed, and also the scanning system has been verified experimentally.

The design of the scanner includes analytical and optical modeling of the proposed scanning configuration, along with the development of experimental setup and validation. Scanning system parameters that affect the imaging quality were studied and selected in the design. In addition, optical modeling of a reflective optics spectrometer was carried out, and an analytical model was developed for spectral domain OCT signal processing. Marechal criterion of Strehl Ratio above 0.8 was used as a benchmark to evaluate the imaging quality of the proposed system.

To validate the line scanning model, an experimental setup consisting of a 53nm spectral bandwidth light source with cylindrical mirrors of 25.85mm and 51.7mm focal lengths was developed. Scanning was performed in both tangential and sagittal directions. The improvement in imaging performance by using sagittal scanning was demonstrated. It was also proved experimentally that the mirror focusing is insensitive variations in beam positions.

ACKNOWLEDGEMENTS

I would like to thank my supervisors, Dr. Sivakumar Narayanswamy and Dr. Muthukumaran Packirisamy, for their guidance, support, and continuous encouragement throughout my doctoral study. I am grateful to have been offered the opportunity to work in their labs and given the project to develop a *state-of-the-art* of reflective optics based optical imaging system for coherence tomography application.

I would also like to thank the past and the present members of the Optical Microsystems laboratory for their expertise, assistance and support. Specially thanks to my friends Dr. Etienne, Jayan, and Roozbeh for their help.

Finally, I would like to thank my family and friends for their unconditional support during my studies. My profound gratitude goes to my wife Sultana Begum, for her patience, understanding, and unconditional support and help.

This thesis is dedicated to my parents, my wife, and my son Sami Bin Kamal who was born during the first semester (Fall 2007) of my doctoral study.

Table of Contents

Chapter 6: Optimized line-scanning system parameters 125

List of abbreviations

AC	Achromatic lens
BFL	Back focal length
BS	Beam splitter
C	Collimator
CA	Chromatic aberration
CL	Cylindrical lens
CM	Cylindrical mirror
CT	Computed Tomography
D	Detector
EFL	Effective focal length
EOCT	Endoscopic optical coherence tomography
ERF	Error function
FD-OCT	Fourier-domain optical coherence tomography
FFT	Fast Fourier Transform
FO	Focusing optics
FPP	Focal plane position
FWHM	Full-width-at-half-maximum
G	Grating
LSF	Line spread function
LS-OCT	Line-scan optical coherence tomography
MEMS	Micro-electro-mechanical-system

Mm	Millimetre
MRI	Magnetic Resonance Imaging
MTF	Modulation transfer function
NA	Numerical aperture
OCT	Optical Coherence Tomography
ROC	Radius of curvature
SD-OCT	Spectral-domain optical coherence tomography
SLD	Superluminescent diode
SM	Scanning mirror
SNR	Signal-to-noise ratio
SR	Strehl ratio
SS-OCT	Swept-source optical coherence tomography
TD-OCT	Time-domain optical coherence tomography
µm	Micrometer
2D	Two-dimensional
3D	Three-dimensional

List of symbols

a	On axis focal length of the cylindrical mirror (Chapter 1)
a	Line spread in the focusing direction (Chapter 4)
A	Pixel area
b	Confocal parameter (Chapter 1)
b	Line spread in line direction (Chapter 4)
d	Distance between scanner and cylindrical mirror
D	Beam diameter
f	Focal length
I_D	Detected interference signal
I_r	Intensity of reference arm
I_s	Intensity of sample arm
k	Wave number
$k_{(i_x, j_y)}$	Wave number of (i_x, j_y)*th pixel*
L_s	Scan length
l_s	Line size on the sample
l_{CCD}	Line size on the detector
m	Diffraction order
N	Number of pixel
r	Radius of curvature
R_r	Power spectral density from the reference arm

R_s	Power spectral density from the sample arm
$R_{fall\text{-}off}(z)$	Sensitivity fall-off
z_r	Reference arm path length
z_s	Sample arm path length
$2z_R$	Depth scan range
$2\omega_0$	Minimum focal spot size
λ	Center wavelength
θ	Scan angle
ϕ	Angle between the incident and the reflected beam
$\delta\lambda$	Spectral resolution
$\Delta\lambda$	Spectral bandwidth
Δx	Transverse resolution in the focusing direction
Δy	Transverse resolution in the line direction
Δz	Axial resolution
ΔN_x	Pixel size in the x-axis of the CCD
ΔN_y	Pixel size in the y-axis of the CCD
(j_x, j_y)	Pixel coordinate
$I(x_{j_x} y_{j_y})$	Intensity of pixel (j_x, j_y)

List of Figures

List of Tables

Chapter 1: Introduction and literature review

1.1 Introduction

The most common biomedical imaging modalities include X-ray radiography, ultrasound imaging, X-ray computed tomography (CT), magnetic resonance imaging (MRI), confocal microscopy, etc. Most of these techniques permit three-dimensional visualization but the resolution is limited for standard clinical applications. For example, ultrasound imaging can penetrate tens of millimeters but the resolution is typically from 100μm to 1mm. High frequency sound waves are required for finer resolution ultrasound, but high frequencies are strongly attenuated in biological tissues [1]. Moreover, poor transducer-air coupling prevents the use of ultrasound for high-resolution endoscopic applications. CT scans involve potentially hazardous ionizing radiation, as do plain radiographs and fluoroscopy. Magnetic resonance imaging (MRI) is bulky and expensive. Confocal microscopy technique can achieve submicron resolution, but the penetration depth is less than 1mm. Optical coherence tomography (OCT) is an optical technology currently emerging as a promising new addition to biomedical imaging because of its high speed and high resolution. The resolution of OCT is 1μm to 15μm, which is much finer than most biomedical imaging techniques, and depth of penetration of OCT is about 2 to 3mm. Depth of focus of OCT imaging can be increased by employing a dynamic focusing system [2]. Consequently, OCT has higher resolution than ultrasound and higher penetration than confocal microscopy. Hence it fills the gap between ultrasound and confocal microscopy. Comparison between the resolution and the penetration depth of different types of biomedical imaging systems is shown in Figure 1.1.

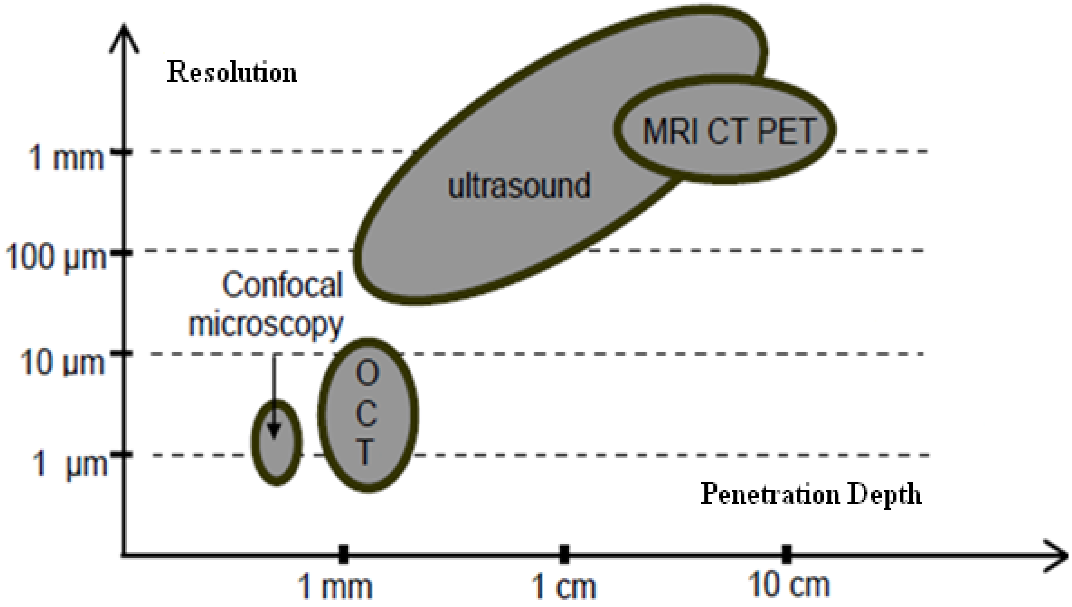

Figure 1.1: Resolution & penetration depth of different biomedical imaging techniques [3].

1.2 Brief history and applications

Huang et al. [4] first demonstrated OCT imaging *in vitro* in the human retina in 1991. Since that time, OCT has been used in rapidly emerging applications of various fields in clinical medicine and materials science research. The performance and capabilities of OCT imaging technology have also improved dramatically in recent years which include the development of real-time imaging [5-7], high performance, and reliability at lower cost [8]. Today OCT is widely used clinically because it provides *in vivo* images with higher resolution than possible with any other biomedical imaging techniques. In addition to ophthalmology, biomedical applications of OCT include the dentistry [9], gastrointestinal endoscopy [10], optical biopsy [11], dermatology [12], respiratory tract [13], gynaecology [14], and tissue engineering studies [15, 16]. OCT catheters and endoscopes have been drawing more attention for future clinical applications [17, 18]. Endoscopic OCT has successfully been used to capture subsurface images of segments of the mucosal tissues of internal organs in the respiratory, urinary, pulmonary, gastrointestinal, and reproductive systems [17, 19]. On the other hand, nonmedical applications of OCT include artworks diagnostics [20, 21], polymer or fiber composite materials investigations etc. to name a few [22-24].

1.3 Endoscopic OCT

Currently the most clinically successful application for an OCT is in the area of ophthalmology. Endoscopic OCT (EOCT) imaging shows great potential for non-invasive, *in vivo* clinical applications [25]. An endoscopic optical biopsy using OCT was first reported in 1997 by Tearney et al [26]. In the same year, endoscopic OCT imaging was also reported by A. M. Sergeev et al. [17]. Rotary fiber optics scanning using a micro prism was used for the first endoscopic OCT system [26]. In 2001, Pan Y. et al. [27] first introduced micro-electro-mechanical system-based scanning (MEMS) for the miniaturization of an OCT probe.

Reliable, compact, and portable design is essential for the convenient access of internal organs. This is a challenging task for endoscopic scanning. Scanners with high-resolution, high-speed, large scan range and lightweight that consume less energy are desirable for endoscopic imaging applications. The challenges for high speed scanning include the optical, engineering, and biological aspects of endoscopic imaging [17]. Various types of scanner configurations, including forward scanner [28], side sector scanner, side linear, and circumferential scanner, were reported [29] for endoscopic imaging by integrating MEMS and fiber optics technology. Side and circumferential imaging endoscopic OCT probes are suitable for imaging within tubular organs, such as vascular systems, gastrointestinal tracts, breast ducts, and urinary tracts. Forward-imaging OCT probes can be very useful in providing tissue structural information ahead of the catheter probe, such as for image-guided biopsy or device placement [28].

1.4 Overview of OCT principle

OCT is a high-resolution non-invasive and non-contact imaging technology. OCT performs high-resolution imaging of the internal microstructure in material and biological systems by measuring backscattered or back reflected light from a semi transparent sample. OCT imaging is analogous to ultrasound imaging, but it measures backscattered light intensity instead of sound waves. OCT imaging is commonly performed by using a Michelson interferometer configuration with a low coherence light source, as shown in Figure 1.2. Low coherent light is split into two arms, known as the reference arm and the sample arm. A beam splitter in a free space optics system or in a fiber-optic coupler in a fiber-based system is used to split the beam. The backscattered light from the sample arm and the reflection coming back from the reference mirror are recombined in the beam splitter and directed towards a detector [1, 30-33].

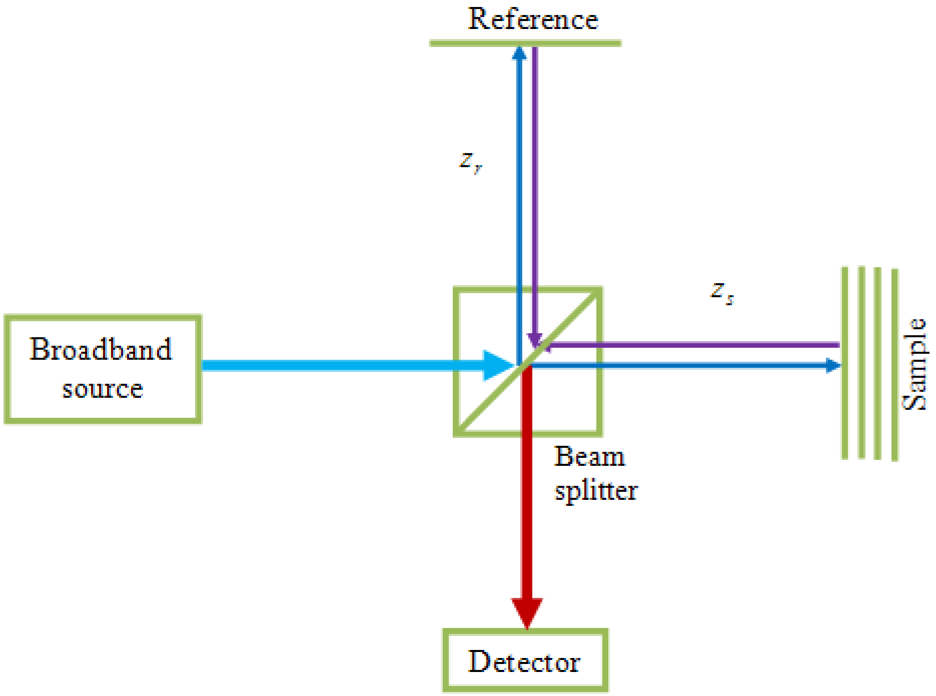

Figure 1.2: Schematic of low coherence interferometry.

The interference happens only when the optical path lengths of light in both the reference arm and sample arm are matched to within the coherence length of the light source [1, 31]. The detected interference signal 'I_D' is expressed by:

$$I_D = R_r + R_s + 2\sqrt{R_r R_s}\cos(2kz_r - 2kz_s) \tag{1.1}$$

Here, R_r and R_s represent the reflectivity of the reference arm and the sample arm respectively. kz_r and kz_s represent the path lengths of the reference arm and the sample arm respectively. Depending on which detecting system and which signal processing is used, the OCT system is broadly classified into the following categories:

1. Time domain OCT (TD-OCT)
2. Fourier domain OCT (FD-OCT)
    a. Spectral domain OCT (SD-OCT)
    b. Swept source OCT (SS-OCT)

1.4.1 Time domain OCT (TD-OCT)

Conventional TD-OCT is the first generation OCT system where, the reference arm is moved to perform the depth scan, as shown in Figure 1.3. To obtain 3D image data of the sample, a beam is required to scan across the surface of the sample using a scanner mirror. During the transverse scanning, the reference mirror performs the depth scanning (A-scan) on the sample and a photo detector records the interference signal for further processing. For each depth location, the reference mirror is moved over a defined range to perform the axial scan while the scanner mirror is held immobile. The transverse scanning is commonly performed by using a Galvo mirror scanner or by using a micro-electro-mechanical-system (MEMS) mirror scanner. Since the depth scan data is collected by moving the reference mirror with a time-varying location, this method is called time domain optical coherence tomography (TD-OCT).

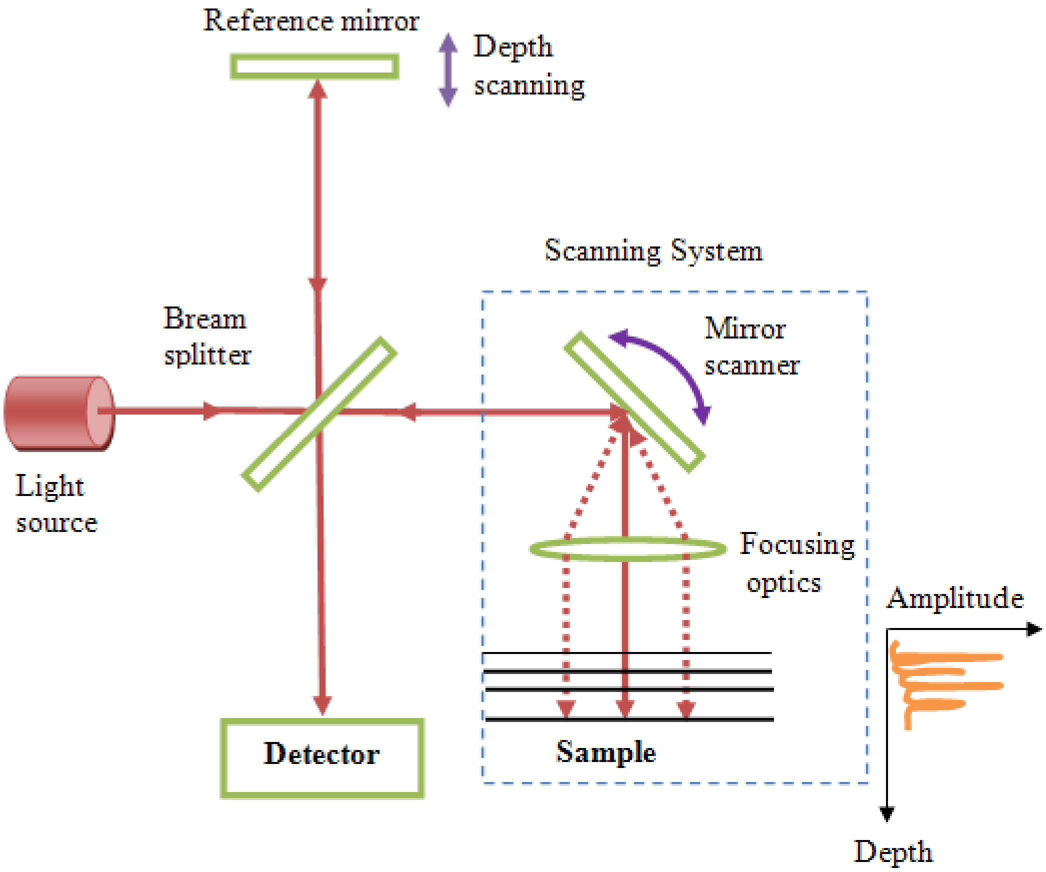

Figure 1.3: The Schematic of a Time Domain OCT system.

1.4.2 Fourier domain OCT (FD-OCT)

In the time-domain scheme, the axial scan (A-scan) data is acquired by successively changing the depth of the coherence gate and by recording the interference at each depth. A more efficient scheme for acquiring interference data was suggested and first realized in 1995 by Fercher et al. [34]. This scheme involves simultaneously detecting the interference from all depths within the sample. This method is referred to as a Fourier-Domain OCT (FD-OCT). In the FD-OCT, the reference arm is fixed, and, therefore, no moving parts are required to obtain the depth scan data. Hence, the FD-OCT increases the data acquisition speed when compared to the TD-OCT. Moreover, the FD-OCT provides a better signal-to-noise ratio when compared with the TD-OCT [35]. FD-OCT systems can be spectrometer-based or swept-source based, as discussed in the following sections.

a. Spectral domain OCT (SD-OCT)

In an SD-OCT, the depth encoded spectral signal is acquired from the entire depth by the grating-based spectrometer. Therefore, it does not require any mechanical scanner to perform axial scanning while the transverse scanning is performed by the scanner, as is shown in Figure 1.4. In this configuration, the scanner arm performs the transverse scan while the spectrally encoded A-scan data is acquired by the spectrometer.

The spectrometer is a key component in the development of SD-OCT systems. In SD-OCT, the interference data is acquired by using a spectrometer and is then processed by using the Fast Fourier Transform (FFT) method. The spectrometer used for SD-OCT consists of a diffractive grating, a collimating and focusing optic, and a detector array. The depth scan range of the SD-OCT is limited by this sensitivity fall-off, which is determined by the pixel size of the detector array and the optics that is used in the spectrometer. The sensitivity fall-off could be improved by improving the spectrometer design [36]. The depth-dependent sensitivity fall-off of the SD-OCT depends on the quality of the spectrometer. Different types of processing algorithms have been developed to improve the sensitivity fall-off of the SD-OCT [37, 38].

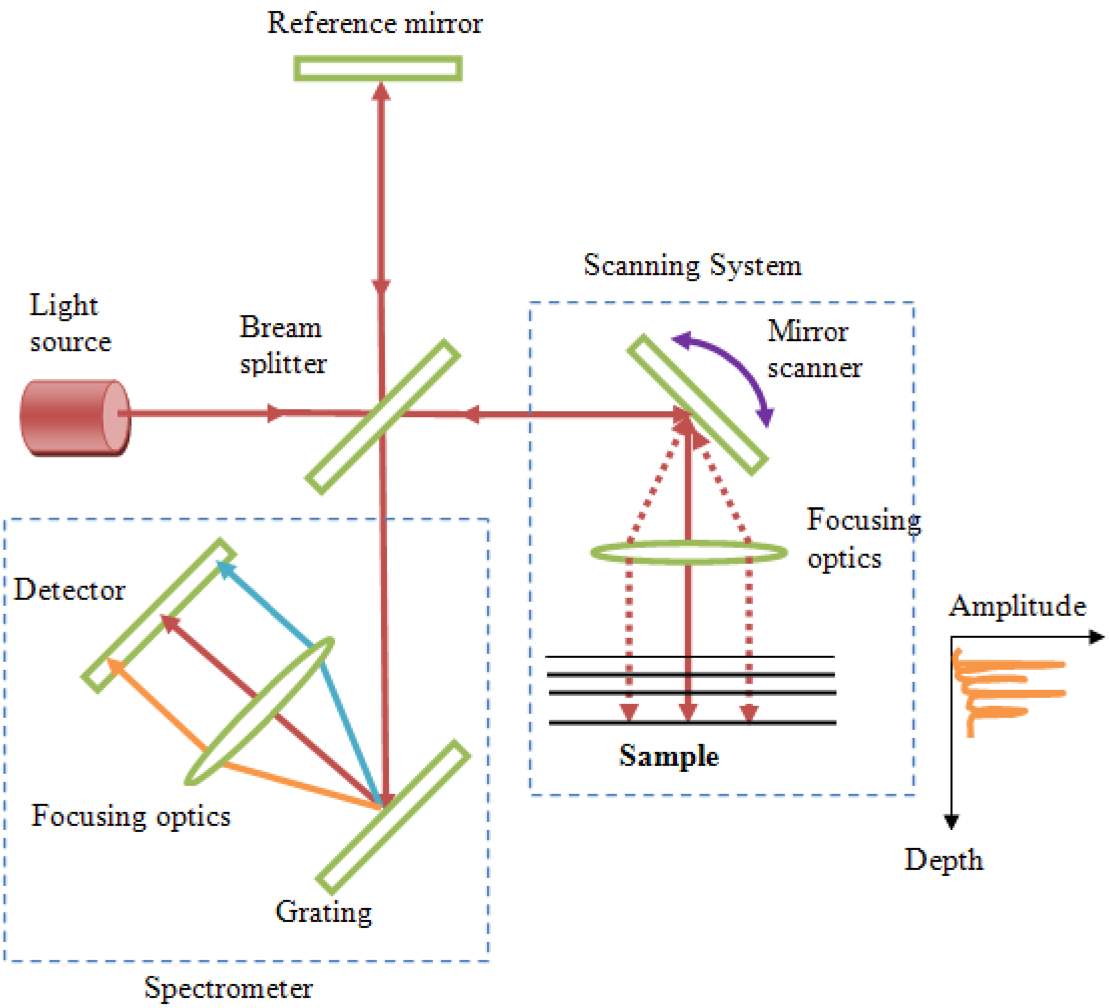

Figure 1.4: Schematic of SD-OCT system.

Chromatic aberration, spot profile, and the detector array resolution are the driving factors in the design of a high quality spectrometer [1, 39]. A refractive optics-based spectrometer is commonly used in SD-OCT imaging, reducing imaging quality because of chromatic aberration. Recently, astigmatism-corrected reflective optics based on a Czerny-Turner spectrometer configuration with an off-the-shelf cylindrical lens has been reported [40-42]. However, this spectrometer was designed for a flying spot scanning imaging system.

b. Swept source OCT (SS-OCT)

In this configuration, the depth scans (A-scan) are performed by sweeping the individual wavelength spectrum coming from the broadband source. A photo detector is used to record the interference signal and further processed to retrieve the depth profile. A similar lateral scanning (B-scan) like a TD-OCT or a SD-OCT is performed in the transverse direction of the sample. The schematic of the SS-OCT configuration is shown in Figure 1.5.

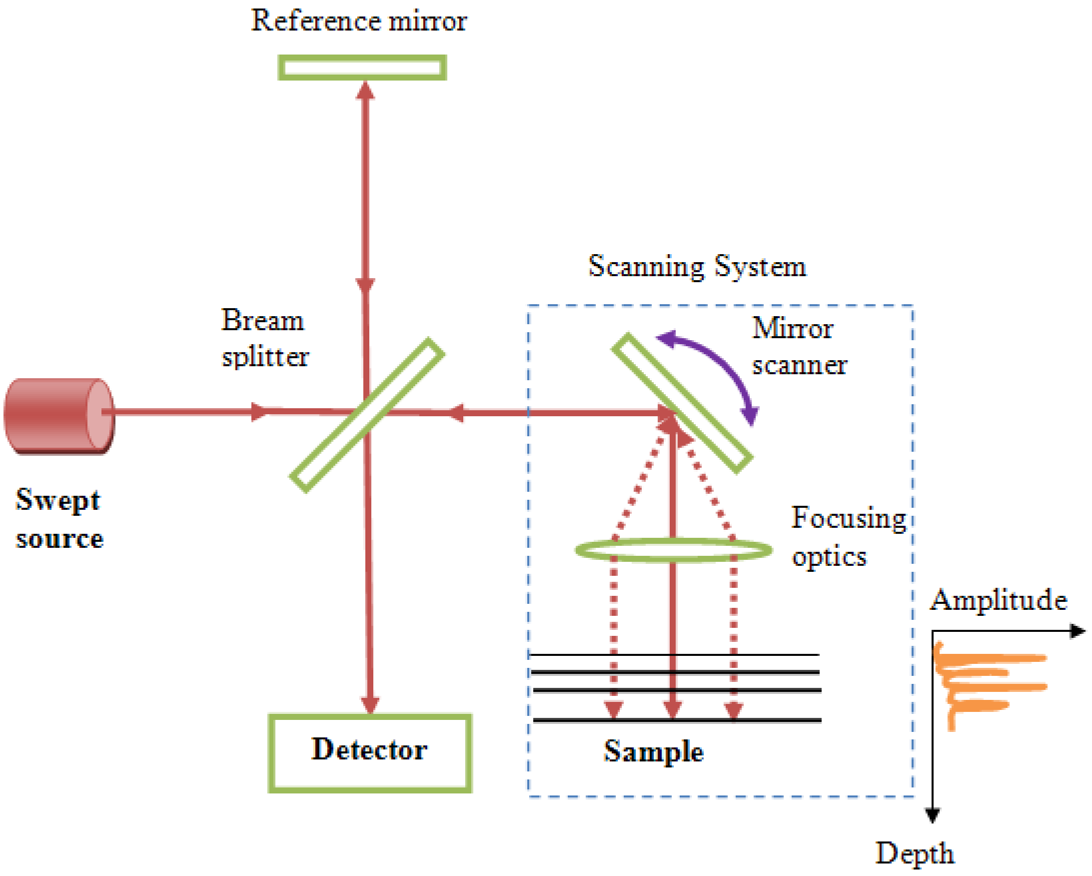

Figure 1.5: Schematic of SS-OCT system.

1.5 OCT scanning protocols

For 3D imaging, a depth scan and two other transverse scans are necessary with flying spot scanning. Depending on the direction, the OCT scanning protocols are named as the A-scan, B-scan, C-scan, and T-scan [33, 43, 44]. Figure 1.6 shows the 3D OCT scanning protocols. These scanning protocols are discussed briefly in this section.

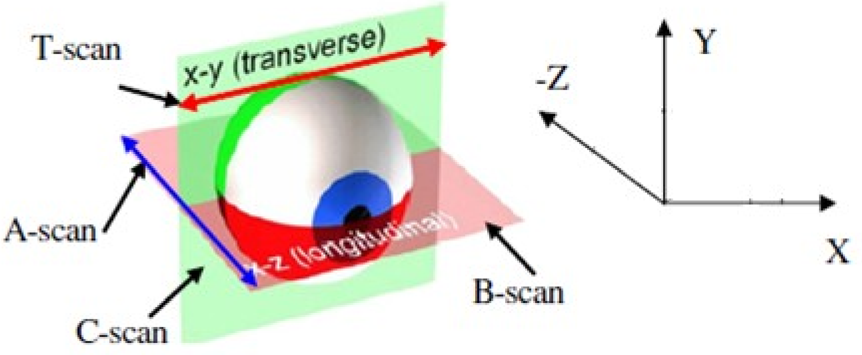

Figure 1.6: 3D OCT scanning protocols [43].

One-dimensional (1D) cross-sectional scanning is performed in the depth direction (Z-axis), which is known as the A-scan shown in Figure 1.7 (a). In the TD-OCT, the A-scan is performed by scanning the reference mirror along the optical axis whereas the spectrally encoded entire depth A-scan data is captured by using a grating spectrometer or by using a swept source in the FD-OCT. No mechanical scanner is required in FD-OCT acquisition.

To perform 2D cross-sectional scanning, a single-axis mechanical scanner is required with flying spot scanning. Depth priority transverse scanning is known as the B-scan, during which, first, the A-scan is performed by using reference mirror scanning, and then the transverse scan is performed by using a mechanical scanner as shown in Figure 1.7(b). Transverse priority scanning is known as the T-scan. 2D cross-sectional scanning is performed by multiple T-scans, which is known as the C-scan as shown in Figure 1.7(c). When transverse priority scanning is performed in the depth direction, the scanning protocol is called the T-scan based B-scan as shown in Figure 1.7(d). In Figure1.7 the scanning priority direction is indicated by fast scanning whereas another direction is indicated by slow scanning.

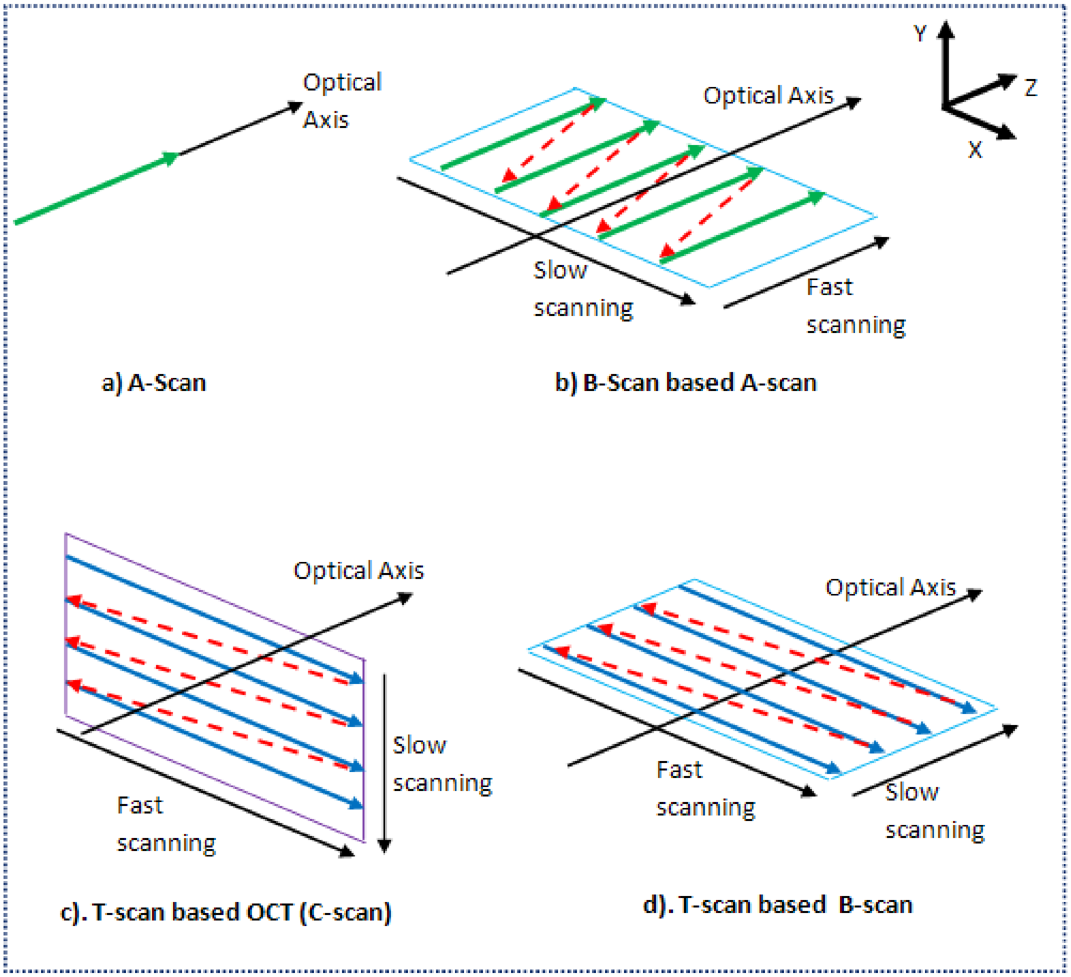

Figure 1.7: OCT scanning protocols.

3D scanning can be performed by using multiple B-scan based A-scans, C-scans, or T-scan based B-scans. While single-axis scanners are sufficient for 2D cross-sectional imaging with a flying spot, a two-axis mechanical scanner is required to perform 3D imaging resulting in a reduced scanning speed. Moreover, distortion errors [45] and motion artifacts [46], such as the ones induced by eye or body motion, affect the imaging quality while flying spot scanning is performed.

Recently (2005) Line-scan OCT (LS-OCT), also referred as parallel OCT, was reported for high-speed imaging [47-54]. Most of these developments use external stage movement for lateral scanning with a pre-objective/post-objective scanner configuration. Nakamura Y et al [47] integrated a galvanometer scanner with LF-OCT for transverse scanning.

1.6 OCT system design

OCT is a modular technology consisting of various hardware and software. Major modules in the OCT system are those for the light source, the imaging engine, the scanning system, the control interface, and the data acquisition and processing. In order to achieve a higher imaging performance, high quality opto-mechanical design is required. As an example, a smaller probe is most useful for endoscopic OCT imaging. Therefore, miniaturization of the scanning system is mandatory. Figure 1.8 shows the major modules of an OCT system from a system point of view. The requirements of the laser source, imaging engine, and control modules are briefly discussed in the following sub-sections.

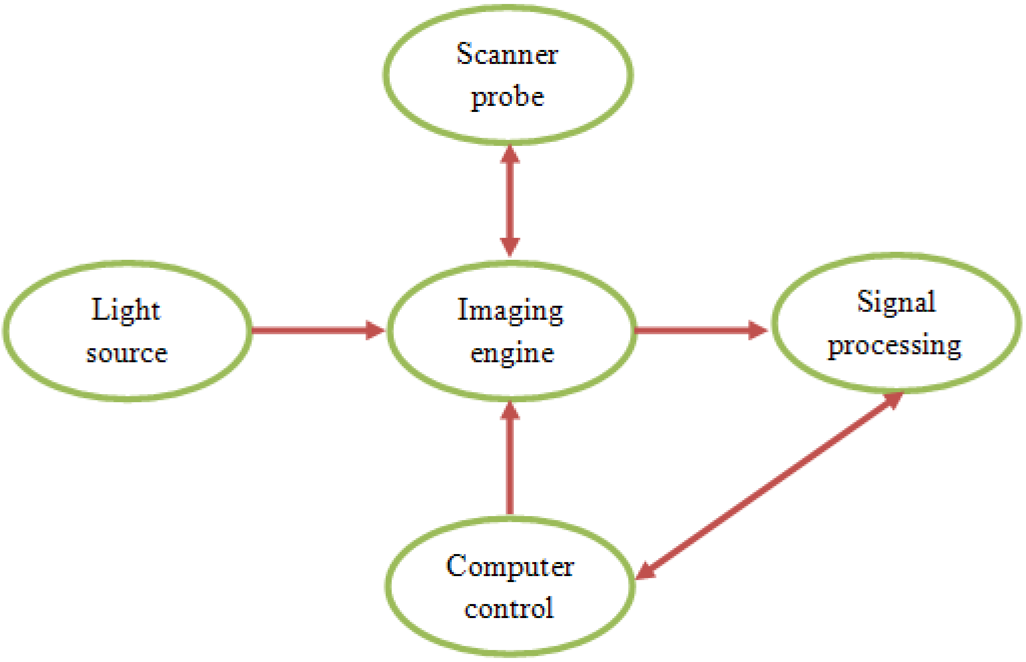

Figure 1.8: Modular representation of OCT imaging technology components.

1.6.1 Light source

Axial resolution of an OCT system is determined by the spectral bandwidth of the light source. The basic requirement of the light source for OCT imaging is that the light source has a short coherence length and, therefore, a higher spectral band. Transverse resolution and depth of focus of the OCT imaging also depends on the wavelength of the light source, and this relationship is discussed in Section 1.7. Superluminescent diodes (SLD) or semiconductor-based light sources are commonly used in OCT. Femtosecond lasers are powerful light sources for ultrahigh resolution OCT imaging since they can generate larger bandwidths across a range of wavelengths in the near infrared.

When light is propagating through tissue, it is attenuated by scattering and absorption. Light scattering decreases when longer wavelengths are used, but the absorption of light due to water content is considerably higher at longer wavelengths. So there is a trade-off when choosing the wavelength. Another issue is the dispersion, which is the difference in the velocity of light for different wavelengths. The dispersion causes the degradation of axial resolution. In the case of water, for example, the dispersion is zero for a wavelength of about 1050nm [55].

Therefore, wavelength selection depends on a particular application. In OCT imaging, light sources with center wavelengths ranging from 800 to 1300nm are used commonly. Such wavelengths can be generated by using solid-state femtosecond lasers, such as the Ti: Al_2O_3, Nd: Glass or Yb fiber, and Cr: Forsterite lasers [1, 10, 56]. It is also important to note that the longer wavelengths increase imaging depth, but reduce the transverse resolution [57].

1.6.2 Imaging engine

Various types of the OCT imaging engines have been developed since its invention. In the first generation OCT imaging, a reference optical delay scanning interferometer is used and this system is known as time domain (TD) OCT. Spectral domain (SD) is the second generation OCT. It acquires spectrally encoded depth information by using a grating spectrometer or source wavelength sweeping. The second generation OCT has a higher acquisition speed and better sensitivity compared to the TD-OCT. Other OCT imaging engines include a Doppler OCT which is used for flow imaging [58] and polarization sensitive or insensitive OCT that was developed to image the birefringence properties of the structure [59].

1.6.3 Scanner probe/ Beam delivery system

The OCT beam-delivery probe is a complex opto-mechanical system consisting of a scanner mirror and focusing optics. The scanner probe design depends on a particular application. For example, a miniaturized probe is useful for endoscopic OCT imaging. Several OCT modalities developed in free-space optics and fiber optics use a galvanometer scanner. However, these systems are bulky and impractical for endoscopic uses because of the size restriction. MEMS technology offers the advantages of a small size at high scanning speeds. It can also be used to miniaturize OCT imaging probes [18, 26, 27, 60-67]. The integration of MEMS and fiber optics technology with a compatible catheter/endoscope represents essential steps towards enabling OCT to become a powerful tool for diagnosis, monitoring, and guidance in the use of *in vivo* applications [17, 26, 68, 69]. The miniaturized OCT systems can be integrated with a wide range of existing biomedical instruments such as endoscopes, catheters, laparoscopes, or needles that enable imaging inside the body. Because of the above-mentioned advantages of MEMS technology, it would be possible to integrate micro-mirrors, micro-motors and micro-lenses with non-endoscopic systems instead of a galvanometer scanner for high speed OCT scanning [2, 70-72]. Most of the MEMS scanners are actuated by electrostatic, [2, 26, 61, 64, 70], thermal, [64, 71, 72] or magnetic methods [67]. However, resolution, scanning/data acquisition speed, sensitivity, and penetration depth are still challenging tasks in OCT technology.

A wide range of platforms and probes has been developed for OCT imaging, including ophthalmoscopes, microscopes, handheld probes, miniature flexible catheters, and endoscopes. These imaging probes could be used separately or in conjunction with other medical imaging instruments such as endoscopes. They could permit internal body imaging in a wide range of organ systems.

1.6.4 Computer control system

Different types of hardware are used in the OCT to perform scanning. Delay line scanning is used in the reference arm to perform the A-scan with the TD-OCT configuration whereas a swept source is used to perform the A-scan with an SS-OCT configuration. A single-axis or two-axis scanner is used for B-scans to acquired 2D or 3D image data. A Galvo mirror or a MEMS mirror scanner is commonly used for B-scans. In addition, data acquisition hardware is used to record the interference signal. Therefore, a software control system is required to sequence and control the hardware and visualize the structure of the scanned sample.

1.6.5 Signal processing

In an SD-OCT, the depth encoded spectral signal is acquired from the entire depth by the grating-based spectrometer. Here, the scanner arm performs the transverse scan while the spectrally encoded A-scan data is acquired by the spectrometer as a function of wavelength (λ). Data processing in the SD-OCT is based on discrete Fourier transformation (FT) of the interference signal. First, the acquired signal is resampled from the wavelength to the wave number space $\left(k = \frac{2\pi}{\lambda}\right)$, and then FT operation is performed to generate axial profile of the sample. Flow chart of the SD-OCT data processing is shown in Figure 1.9.

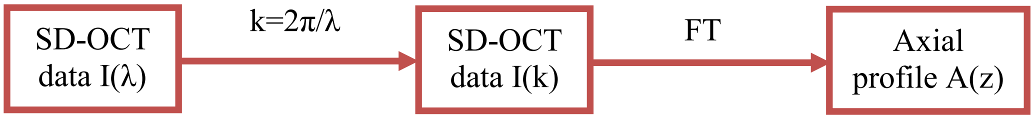

Figure 1.9: Axial profile generation flow chart

Spectrally encoded interference signal in the wave number space is expressed by [1, 35, 37, 38, 73]:

$$I(k) = S(k)\left(\begin{array}{l} R_r + \sum_{s_i} R_{s_i} + 2\sqrt{R_r}\sum_{s_i}\sqrt{R_{s_i}}\cos(2k(z_r - z_{s_i})) + \\ 2\sum_{s_i}\sum_{s_j \neq s_i}\sqrt{R_{s_i}R_{s_j}}\cos(2k(z_{s_i} - z_{s_j})) \end{array}\right) \qquad (1.2)$$

Here, $S(k)$ is the source spectral intensity distribution, R_r is the reflectivity of the reference arm mirror, R_{s_i} and R_{s_j} are the reflectivity in the i^{th} and j^{th} layers of the sample, z_r and z_{s_i} are optical path length of the reference arm and i^{th} layer of the sample. Axial profile of the sample can be retrieved by performing a discrete Fourier transform of Equation (1.2).

$$A(z) = \left|FT^{-1}[I(k)]\right| = \Gamma(z) \otimes \left(\begin{array}{l} R_r\delta(0) + \sum_{s_i} R_{s_i}\delta(0) + 2\sqrt{R_r}\sum_{s_i}\sqrt{R_{s_i}}\delta(z \pm z_{s_i}) + \\ 2\sum_{s_i}\sum_{s_j \neq s_i}\sqrt{R_{s_i}R_{s_j}}\delta(z \pm z_{s_i s_j}) \end{array}\right) \qquad (1.3)$$

Here Γ(z), is the envelope of the coherence function of the source spectrum. The first two terms within the brackets of the Equation (1.3) are non-interferometric contributions, known as DC components. The third term within the brackets in Equation (1.3) is the cross-correlation term that is desired for OCT imaging which contains the axial reflectivity profile of the sample. The last term within the brackets in Equation (1.3) represents the mutual interference of reflectors within the sample layers, and this is known as auto-correlation term.

1.7 OCT system design parameters

The OCT is based on the principle of low coherence interferometry. It uses a broad spectral band light source for high resolution imaging. By contrast with conventional microscopy, OCT resolution is decoupled in the axial and transverse directions. The axial resolution of the OCT is determined by the spectral bandwidth of the broadband source whereas the transverse resolution is determined by the numerical aperture (NA) of the scanner arm. Though the axial and transverse resolutions are decoupled in the OCT imaging, in TD-OCT the depth scan range is still determined by the NA of the scanner arm, whereas in FD-OCT it is dependent only on the spectrometer resolution.

a. ***Axial resolution*** **(Δz):** The axial resolution of the OCT system is the ability to resolve two reflecting boundaries that are closely spaced in the axial or depth direction. Axial resolution of the OCT system is expressed by:

$$\Delta z = \frac{2\ln 2}{\pi}\frac{\lambda^2}{\Delta\lambda} \tag{1.4}$$

Where, $\Delta\lambda$ is the full width at half maximum (FWHM), and λ is the center wavelength of the light source. The dependence of axial resolution of the light source based on the spectral bandwidth and the center wavelength is shown in Figure 1.10.

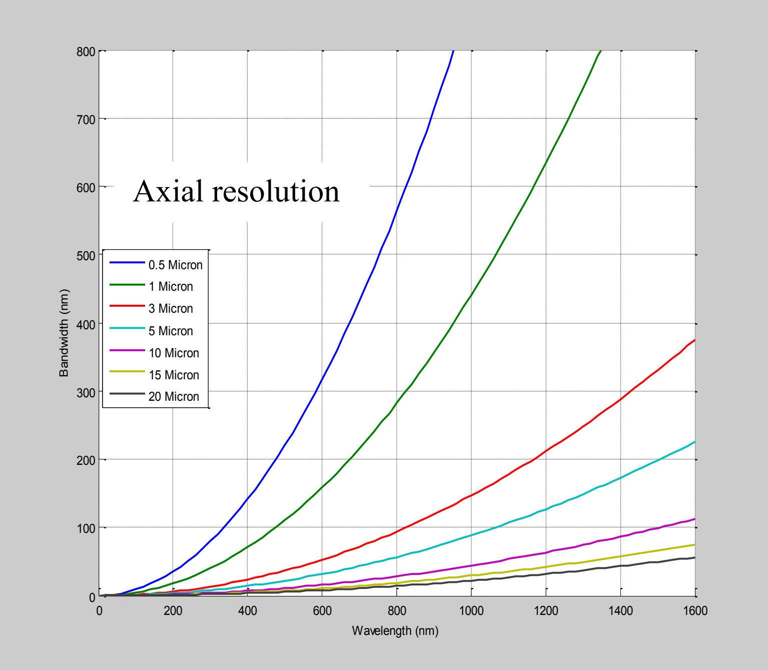

Figure 1.10: Variation of bandwidth against wavelength for different axial resolutions.

b. ***Transverse resolution* (Δy):** The distance between any two spots in the transverse plane at which the points are just separately resolvable is known as the transverse resolution. Diffraction limited transverse resolution can be measured by the distance between two point spread functions (PSF), as shown in Figure 1.11. Therefore, the transverse resolution for the flying spot OCT is determined by the diffraction limited spot size of the focused light beam, which is expressed by:

$$\Delta y = \frac{4}{\pi}\frac{\lambda f}{D} \qquad (1.5)$$

Where, D is the beam size on the objective lens, λ is the center wavelength of the light source, and f is the effective focal length of the focusing optics. High transverse resolution can be obtained by using a high numerical aperture (NA) and therefore a smaller focal spot size.

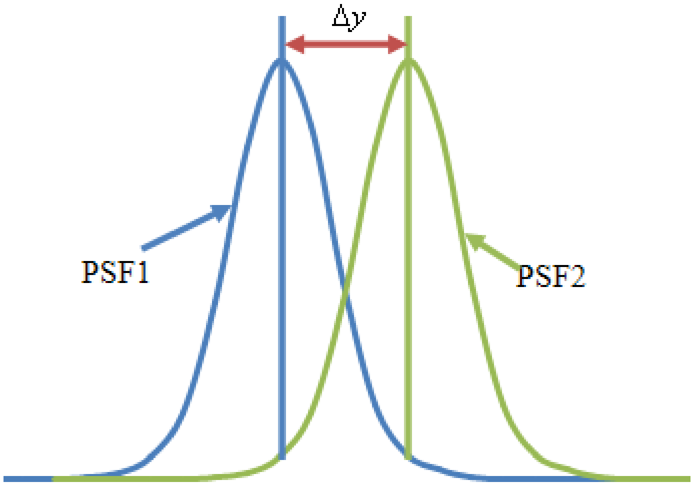

Figure 1.11: Diffraction limited transverse resolution.

c. ***Scan depth (2z_R):*** In TD-OCT, the depth scan range is determined by the numerical aperture (NA) of the scanner arm whereas in FD-OCT the depth scan range is determined by the spectrometer resolution. Therefore, in TD-OCT, the depth scan range is the confocal parameter of the system, which is twice that of the Rayleigh range $2z_R$ as expressed by:

$$2z_R = \frac{8\lambda}{\pi}\frac{f^2}{D^2} = \frac{\pi \Delta y^2}{2\lambda} \tag{1.6}$$

Where, Δy is the transverse resolution and λ is the center wavelength of the light source. Increasing the transverse resolution by using high NA produces a lower depth scan for OCT imaging [57]. Figure 1.12 shows the trade-off between the transverse resolution and the scan depth of the OCT imaging. Dynamic focusing OCT systems have the ability to increase the depth of focus as well as the transverse resolution [30, 31]. Impact of wavelength on transverse resolution and depth of focus is shown in Figure 1.13.

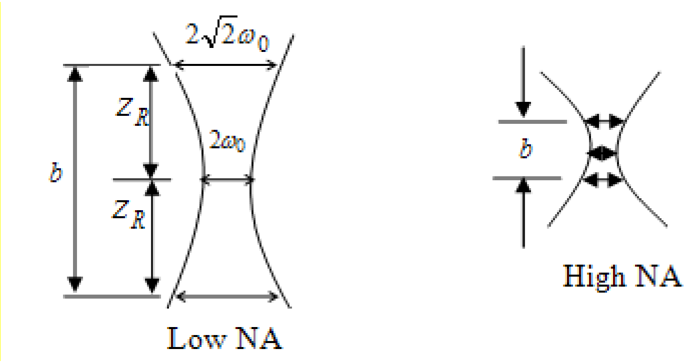

Figure 1.12: Trade-off between the transverse resolution and depth of focus ($2\omega_0$ is the minimum focal spot size, z_R is the Rayleigh range, and b is the confocal parameter).

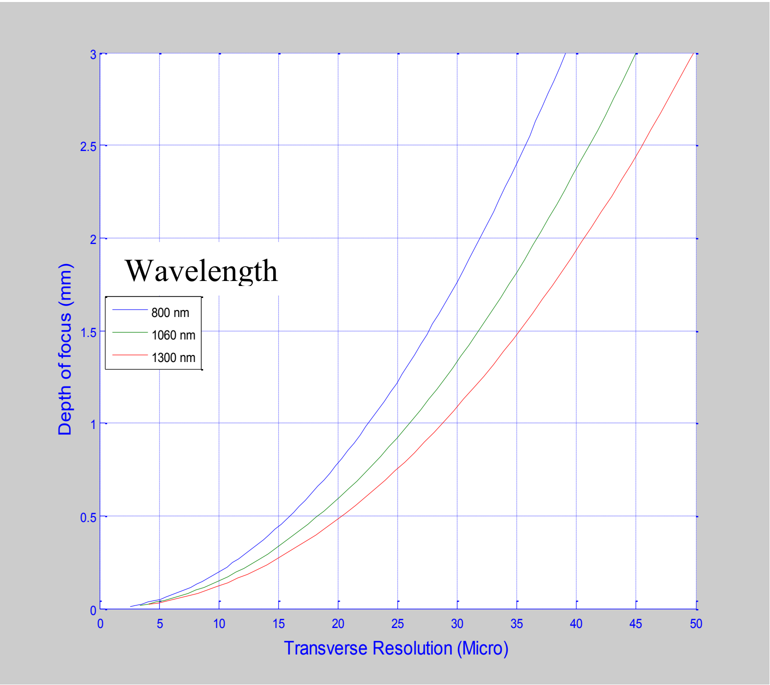

Figure 1.13: Variation of depth of focus against transverse resolution for different wavelengths.

The depth scan range in the FD-OCT depends on the spectral resolution of the spectrometer. The depth scan range [30] of the SD-OCT is expressed by:

$$Z_R = \frac{1}{4}\frac{{\lambda_c}^2}{\delta\lambda}N_x \tag{1.7}$$

Where, λ_c is the center wavelength of the broadband light source, $\delta\lambda$ is the spectral range covered in the spectrometer detector, and N_x is the number of pixels of the detector in the spectrum disperses direction. Therefore, in the line-field SD-OCT system, the transverse resolution in the line direction and the depth scan range are determined by the spectrometer whereas the transverse resolution in the focusing direction is determined by the scanner arm focusing system.

d. ***Sensitivity/ Signal-Noise-Ratio (SNR):*** The sensitivity of an OCT system, also called the optical dynamic range, can be defined as the ratio of the signal power generated by a perfectly reflecting mirror P to the noise of the system. The signal-to-noise ratio (SNR) is expressed by [33]:

$$SNR = 10\log\left(\frac{\eta P}{2h\nu NEB}\right) \tag{1.8}$$

Where, η is the detector quantum efficiency, $h\nu$ is the photon energy, P is the signal power, and NEB is the noise equivalent bandwidth of the electronic filter used to demodulate or detect the signal. High image acquisition speeds or higher image resolutions require higher optical powers for a given SNR. Noise is generated by the light source, the interferometer, and the detector. 90-100 dB sensitivity is desired for good quality OCT imaging [74].

1.8 Line scanning and flying spot scanning

In LS-OCT, a collimated beam is focused by using a cylindrical optics as a line on the sample. Focused line size in the focusing direction is determined by the NA of the focusing optics whereas the other direction remains the same as the collimated beam size. A single axis mechanical scanner is required to obtain 2D image data using flying spot scanning. The beam moves through multiple positions to perform B-scans as shown in Figure 1.14(a). To obtain the 3D image data, a 2-axis scanner is required as shown in Figure 1.14(c).

On the other hand, cross-sectional imaging data can be obtained by using line-focus scanning with SD acquisition without requiring a mechanical scanner, as shown in Figure 1.14(b). The B-scan is covered by the focused line length. 3D image data can thus be obtained by using line scanning with SD acquisition by integrating just a single axis scanner to perform the T-scans, as shown in Figure 1.14(d). As a result, line-filed scanning increases the scanning speed while maintaining the sensitivity advantage of flying spot scanning with SD acquisition [40].

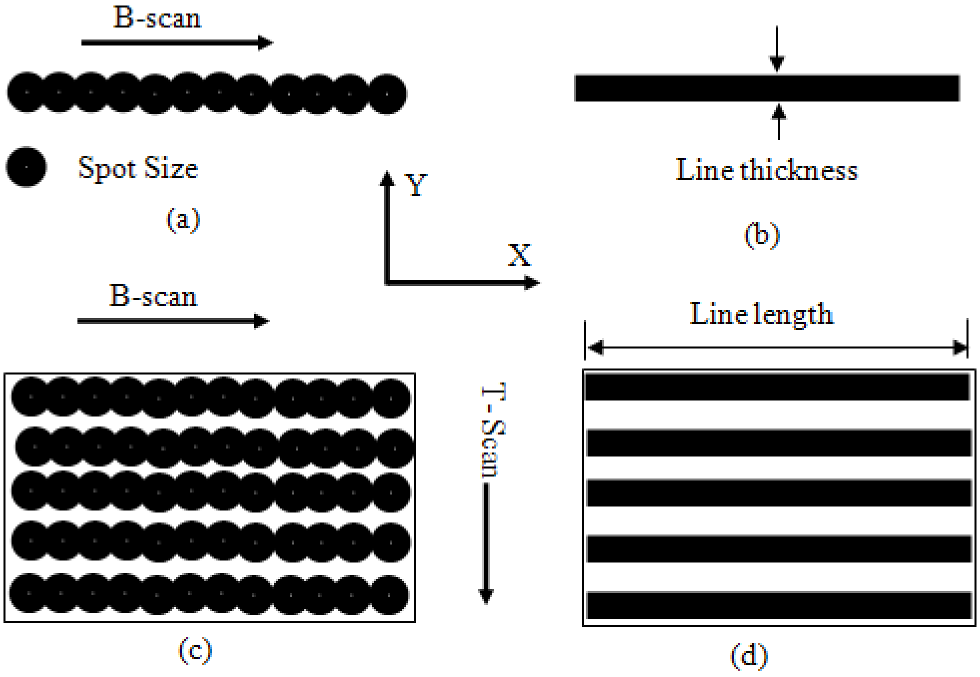

Figure 1.14: (a) 1D scan with flying spot, (b) 1D scan with line-scan, (c) 2D scan with flying spot, and (d) 2D scan with line scan.

Moreover, flying spot scanning reduces the image quality owing to image distortion errors caused by motion artifacts, such as eye or body motion as shown in Figure 1.15. B-scans, which are required to generate cross-sectional image data, can be eliminated in LS OCT. Hence, the advantages of line scanning compared to flying spot scanning include increase in scanning speed, in addition to reduction in scanning distortion errors and motion artifacts.

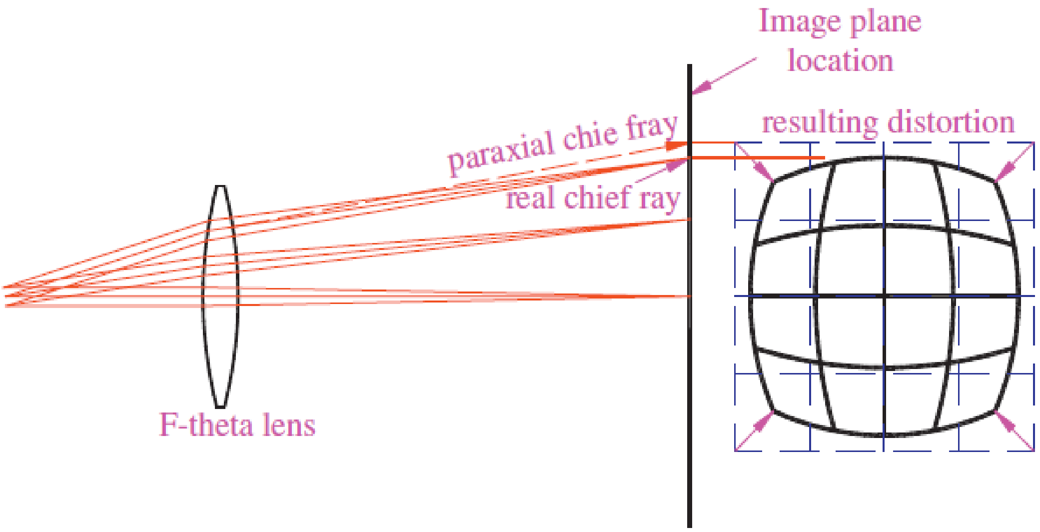

Figure 1.15: Image distortion due to flying spot scanning [45].

In line-scan OCT, transverse resolution is defined independently in the focusing direction and in the line direction [47, 48]. Resolution in the focusing direction is the same as the transverse resolution with flying spot scanning, discussed in Section 1.7, whereas the resolution in the line direction is determined by the detector resolution. The transverse resolution in the line direction is determined according to the Nyquist theorem, which is expressed by:

$$\Delta x = 2l_s \frac{M}{N} \tag{1.10}$$

Here, $M = \frac{l_s}{l_{CCD}}$, l_s is the size of the focused line beam in the object and l_{CCD} is the line size observed in the CCD detector or the detector field of view. N is the number of pixels of the CCD detector.

1.9 Refractive optics and reflective optics OCT

OCT imaging system consists of many different optical elements. Traditionally, lenses are being utilized in OCT imaging for focusing the beam in the scanner and in the spectrometer arm. In the free-space or fiber-based OCT, number of collimating lens, focusing lens and mirrors are used. Every single optical element contributes to the imaging performance of the OCT system. A fiber-optics based OCT system configuration is shown in Figure 1.16. Collimating lenses and focusing lenses reduce the imaging quality of the OCT system due to the chromatic aberration (CA). Moreover, imaging quality is reduced because of the defocus within the scan range. Achromatic lenses can reduce the chromatic aberration if the beam is on its optical axis, but it is completely ineffective if the beam moves away from the optical axis. In the OCT system, off-axis movement of the beam on the focusing lens is required to scan a sample in the scanner arm, while in the spectrometer arm, the beam is dispersed across the cross section of the lens owing to grating dispersion prior to the lens itself. These two lenses are identified as FO in Figure 1.16. This issue is usually minimized by employing either telecentric or aspheric lenses in OCT imaging. However, these lenses are expensive, and they require complex design in order to maximize their performance. Moreover, system-specific design is required for various wavelength ranges.

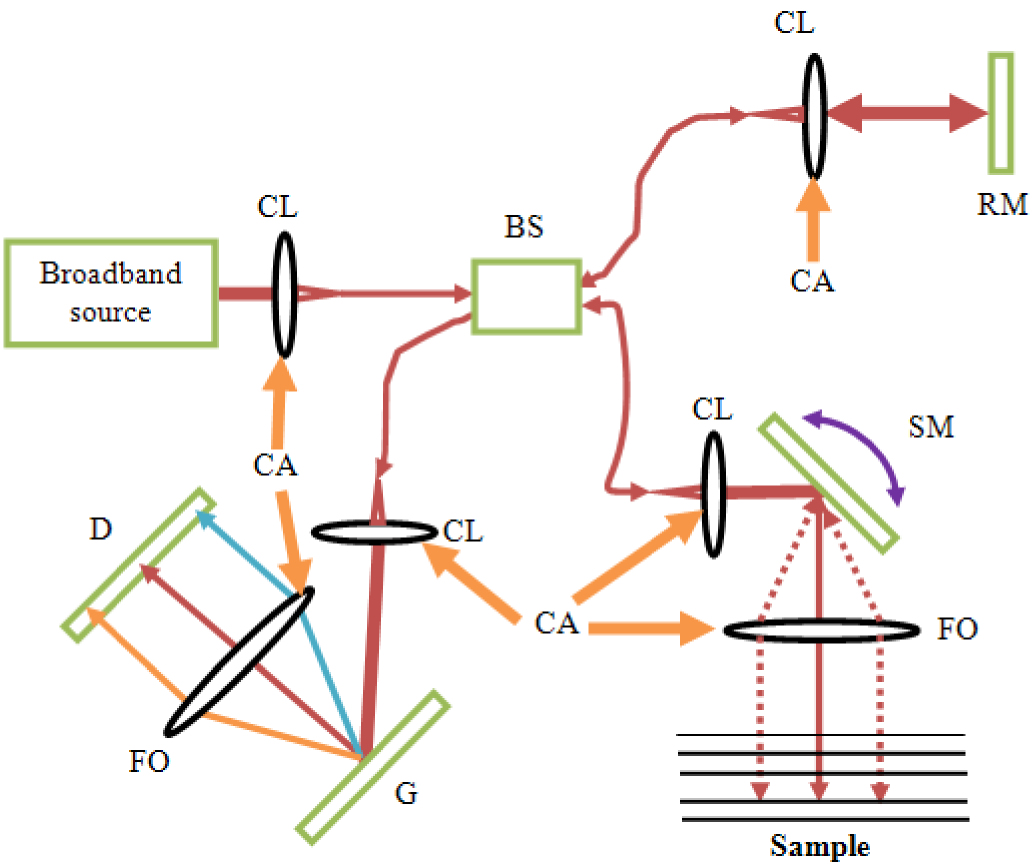

Figure 1.16: Fiber optics OCT system. (CL-collimating lens; BS-beam splitter; RM-reference mirror; SM-scanning mirror; FO-focusing optics; G-grating; D-detector; CA-chromatic aberration).

The performance of the optical system is expressed in various ways. The commonly used quality matrix of an optical system includes spot diagram, Strehl ratio, aberrations, distortion, illumination distribution, modulation transfer function (MTF), encircled energy, etc. [60, 75, 76]. Comparison of the performance of the reflective optics and the refractive optics imaging systems is presented in the following sub-sections.

1.9.1 Chromatic aberration

The refractive optics contains mainly lenses that are made of glass. The index of refraction of the glass and other transmitting materials changes with the wavelength of light. The result is aberrations, which change as a function of the wavelength, known as chromatic aberrations. The effective focal length (EFL) of the shorter wavelength is smaller than that of the longer wavelength for a specific lens. Figure 1.17 shows the wavelength dependent EFL positions with a broad spectral bandwidth light source.

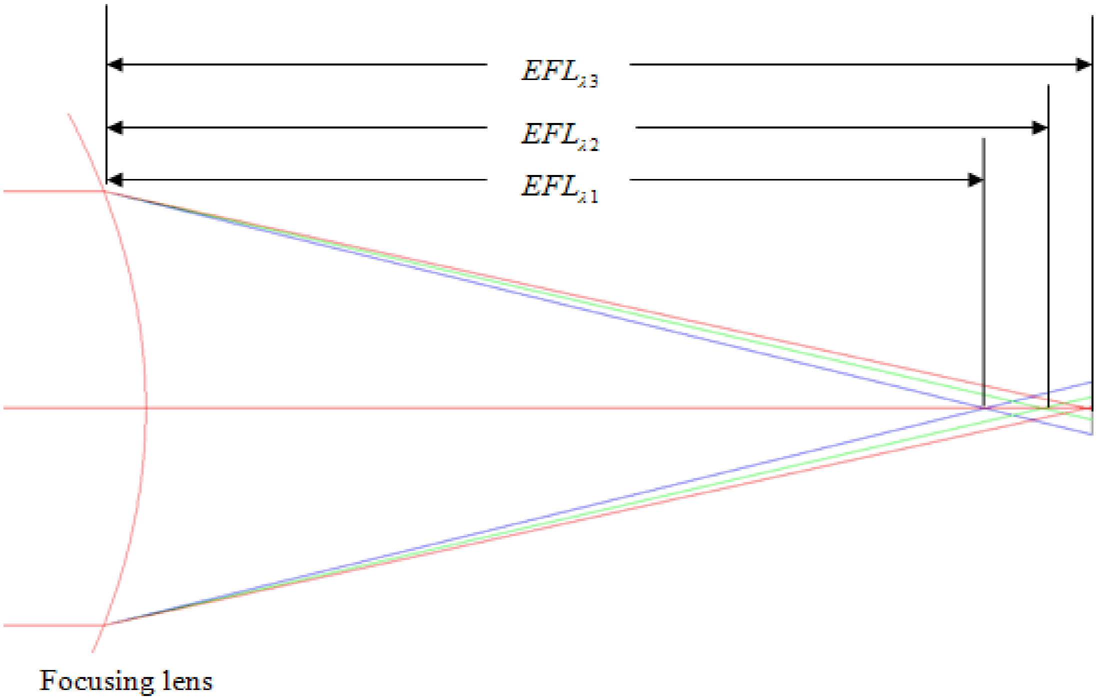

Figure 1.17: Wavelength dependent ELF positions of a broad spectral band light source

$\lambda 1 < \lambda 2 < \lambda 3$

The state-of-the-art of OCT technology uses an ultra broad spectral bandwidth light source for high axial resolution. Lenses are commonly used in OCT imaging. Due to the chromatic aberration, lens focusing reduces the axial resolution of OCT imaging [39].

The effect of chromatic aberration with a conventional lens and a custom-made achromatic lens is shown in Figure 1.18 [39]. Spectra are presented as a function of focusing distance. In the case of standard lenses, effective optical bandwidths change spatially thereby changing axial resolution as seen in Figure 1.18(a). This problem is corrected when using a custom made achromatic lens for the specific wavelength band as can be seen in Figure 1.18(b).

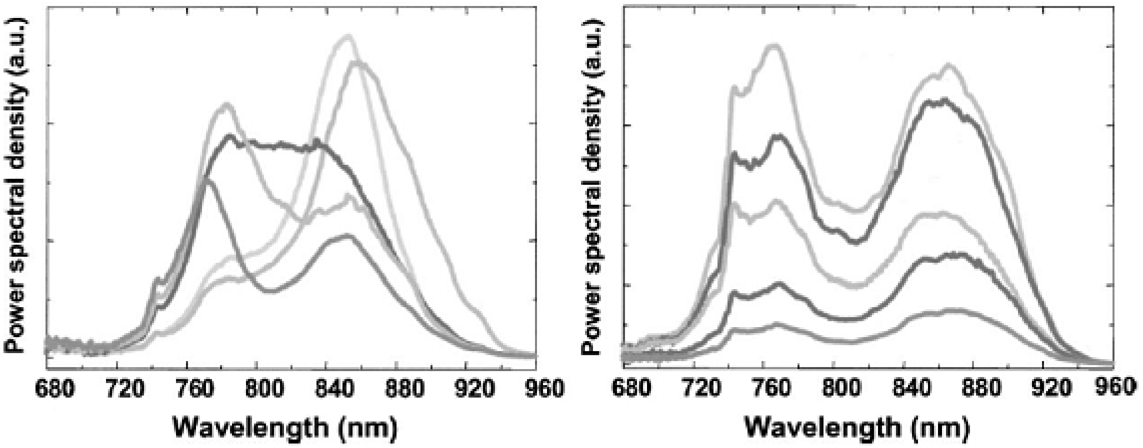

(a) (b)

Figure 1.18: Effects of chromatic aberration (a) with conventional lens and (b) specially designed achromatic lens [39].

On the other hand, reflective optics focusing eliminates the chromatic aberration due to its insensitivity to broadband spectrum [77, 78], and hence the image quality is enhanced. The ELF position of a 200nm spectral bandwidth light with a centre wavelength of 830nm is shown in Figure 1.19. Focusing using mirror maintains zero chromatic focal shifts for any spectral bandwidth [79]. Therefore, a system-specific design is not required while using mirror focusing.

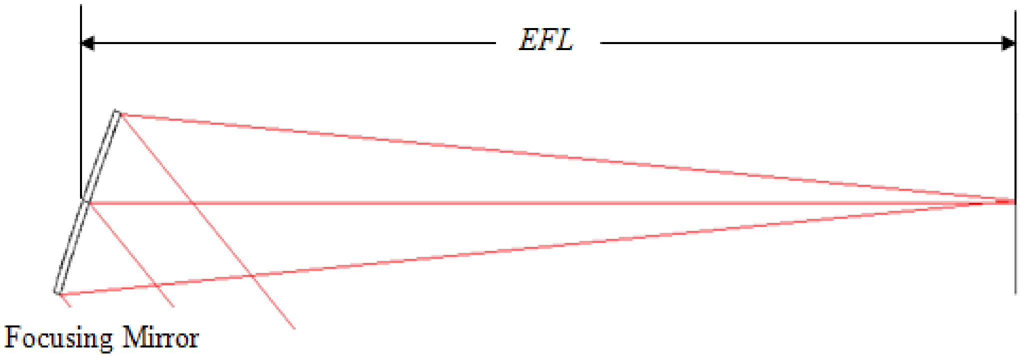

Figure 1.19: Wavelength independent ELF position of a broad spectral band light source using mirror focusing.

1.9.2 Distortion and scan field flatness

For 2D or 3D OCT imaging, a focused beam is required to move across the sample surface to perform the B-scan in flying spot scanning. Depending on the geometrical configuration, the scanning system is classified as objective scanning, pre-objective scanning, and post-objective scanning [79, 80]. These types of scanning are commonly used to perform the B-scans of the OCT imaging. In the pre-objective configuration, a scanning mirror is placed before the focusing lens. This type of scanner gives high-speed beam modulation on flat field scanning. However, a complex lens system design is required. High-speed beam modulation is also possible with post-objective scanning, where a scanning mirror is placed after the focusing lens. A simple lens system is sufficient in the case of post-objective configuration, but the scan field is curved [77, 81, 82]. Moreover, because of the lens used for the B-scans, lens focusing generates a distorted image field, as discussed in Section 1.8.

1.9.3 Strehl ratio (SR)

The Strehl ratio is one of the key parameters used for assessing optical system imaging quality [60, 83, 84]. The Strehl ratio is a quantity that provides information about the flatness of the wavefront, and therefore, the quality of the optical system. This is the ratio of the peak intensity in the diffraction pattern of an aberrated spread function to the peak intensity in the diffraction pattern of the same aberration free spread function. The SR is measured from the aberrated central intensity (I_A) of spread function to the central intensity in the aberration free (I_{AF}) of spread function, which is expressed by $SR = \frac{I_A}{I_{AF}}$.

The solid line in Figure 1.20 shows an aberration-free spread function whereas the dotted line shows an aberrated spread function. In ideal conditions, in an aberration-free optical system, the SR value is 1. However, according to the Marechal condition an SR of 0.8 or higher is required for a good quality optical system [85]. The shape and size are determined by the pupil size, the effective focal length (EFL) of the focusing optic, the wavelengths, and the geometric configuration of the system. The shape and size of the spread function determine the transverse resolution of the system. The transverse resolution is measured at the full-width-at-half-maximum (FWHM) of the spread function. The FWHM of the aberration-free spread function and aberrated spread functions are indicated by Δy in Figure 1.20.

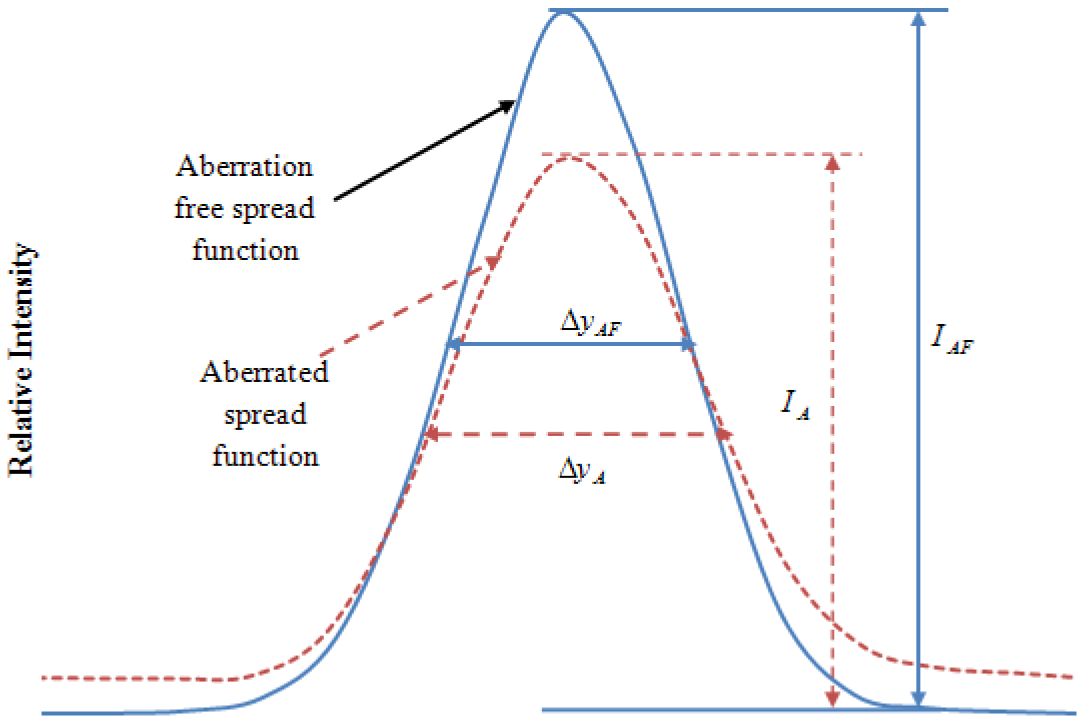

Figure 1.20: Intensity distribution of an aberration free vs. aberrated spread function.

Ultra broad spectral band light source is required for ultrahigh axial resolution whereas lateral resolution is determined by the optics used in the scanning system. The refractive optic is commonly used in OCT imaging. As discussed in Section 1.9.1, refractive optics focusing reduces the imaging quality due to the chromatic aberration. Moreover, in OCT, B-scans are performed in order to image 2D or 3D structures. Uniformity of the imaging quality throughout the scan range is required to maintain the transverse resolution, which is measured at the FWHM of the spread function.

1.10 Thesis motivation

OCT is a cross-sectional imaging technology. Traditionally spot-focused scanning is used for transverse (B-scan) scanning to obtain a two-dimensional (2D) or three-dimensional

OCT image. 2D cross-sectional OCT image can be obtained by using a single-axis scanner, and for acquiring 3D image data a two-axis scanner is required. Mechanical scanning in the transverse direction increases the time to acquire an image and may limit clinical applications. Moreover, imaging performance is affected due to the scanning distortion errors and motion artifacts.

Alternatively, parallel detection, such as line-scan (LS) OCT [47, 48, 52, 53, 86] and full-field has been developed for high speed imaging. Full-field OCT (FF-OCT) is not suitable for endoscopic OCT imaging [87]. 2D OCT image can be obtained by using a line scanning without any mechanical scanner, while 3D image can be obtained by integrating a single-axis scanner. Hence, line scanning system is relatively faster compared to the spot focused scanning. Most of the developed LS-OCT systems implemented either external sample movement [48] or galvanometer [47, 86] mirror for transverse scanning. Therefore, these systems are bulky and impractical for endoscopic scanning.

In addition, lenses were used in the developed LS-OCT systems. Effective focal length of the conventional lens varies with wavelength of the light source. Ultra-broad spectral band light is used for ultra high resolution OCT imaging. However, conventional lenses focus this ultra broadband spectrum in different focal plane. Because of that the axial resolution of the system degrades [39]. Specially designed telecentric or aspheric lenses are needed to reduce this chromatic aberration to improve the imaging performance, making the systems expensive.

Endoscopic 3D-OCT imaging is challenging because it requires the development of miniature beam scanning technologies that would enable two-dimensional raster scanning with a flying spot or one-dimensional scanning with LS-OCT. LS is a promising technology for high speed OCT imaging. Line scan OCT systems developed thus far are based on refractive optics, i.e. lenses are used for scanning system as well as spectrometer, thereby causing errors due to chromatic aberration and scan field distortion as discussed earlier. In order to eliminate the errors due to chromatic aberration and distorted scan field, and to achieve faster and finer imaging capability, line scan OCT with reflective optics is proposed in this thesis.

1.11 Thesis objective and scope

Objective of this thesis is to develop a reflective optics-based line-scan spectral domain OCT (SD-OCT) system for high-quality three-dimensional endoscopic imaging applications. Target scan range is 2mm X 2mm X 2mm in the x, y, and z direction respectively. The specific objectives of the proposed research are:

1. Design and development a reflective optics based line scanning system for OCT imaging:
    a. Development of a mathematical model for reflective optics based line scanning system.
    b. Optical design and simulation of the reflective optics based line scanning system
    c. Comparison of the imaging performance of the proposed scanning system with that of the refractive optics based scanning systems.

    d. Experimental validation of the proposed line scanning system.
    e. Parametric study of scanning system and imaging quality enhancement.

2. Design of a reflective optics based spectrometer for line scan SD-OCT imaging:
    a. Optical modeling of the reflective optics based spectrometer.
    b. Comparison of the imaging performance of the proposed spectrometer with that of the refractive optics spectrometers.
    c. Development of an analytical model for line-scan SD-OCT signal processing.

1.12 Thesis contribution

The main contribution of this work to the field of OCT imaging is to utilize reflective optics instead of traditional refractive optics for high quality imaging. Figure 1.21 (a) shows the proposed system configuration and Figure 1.21(b) shows the layout of endoscopic OCT scanning system. Specific contribution of the present thesis:

- The proposed line scanning will increase the imaging speed few folds compared to the flying spot scanning as discussed in Section 1.8. As a result it will reduce the motion artifacts such as eye and body motion.
- Line-scanning will eliminate one axis of scanning. Hence, focused line will be with the reduced scanning distortion errors in one direction as discussed in Section 1.9.2.
- In contrast to the previous approaches, the proposed system will be able to scan a flat field [88, 89] by using off-axis cylindrical mirror, which will reduce the

scanning distortion errors in the other directions. Therefore, combination of focused line and cylindrical mirror will give a high quality imaging.

- Effective focal length of the cylindrical mirror is insensitive to the spectral bandwidth of the light source [77, 78]. As the cylindrical mirror focuses the whole spectral band in the same plane it will result in the elimination of the chromatic aberration. Hence, axial resolution of the OCT will not be degraded as discussed in Section 1.9.1.
- This proposed scanning system can be utilized for OCT imaging applications with sub-micron axial resolution, in general. With the ability to miniaturize the proposed scanning system, this can have an impact in endoscopic imaging applications, in particular.
- In addition, the proposed reflective optics spectrometer will improve the depth dependant sensitivity fall-off.

Complete reflective optics line-scan endoscopic OCT will allow clinicians a powerful tool they need for real time diagnosis, monitoring, and guidance in the use of *in vivo* applications with a high imaging quality.

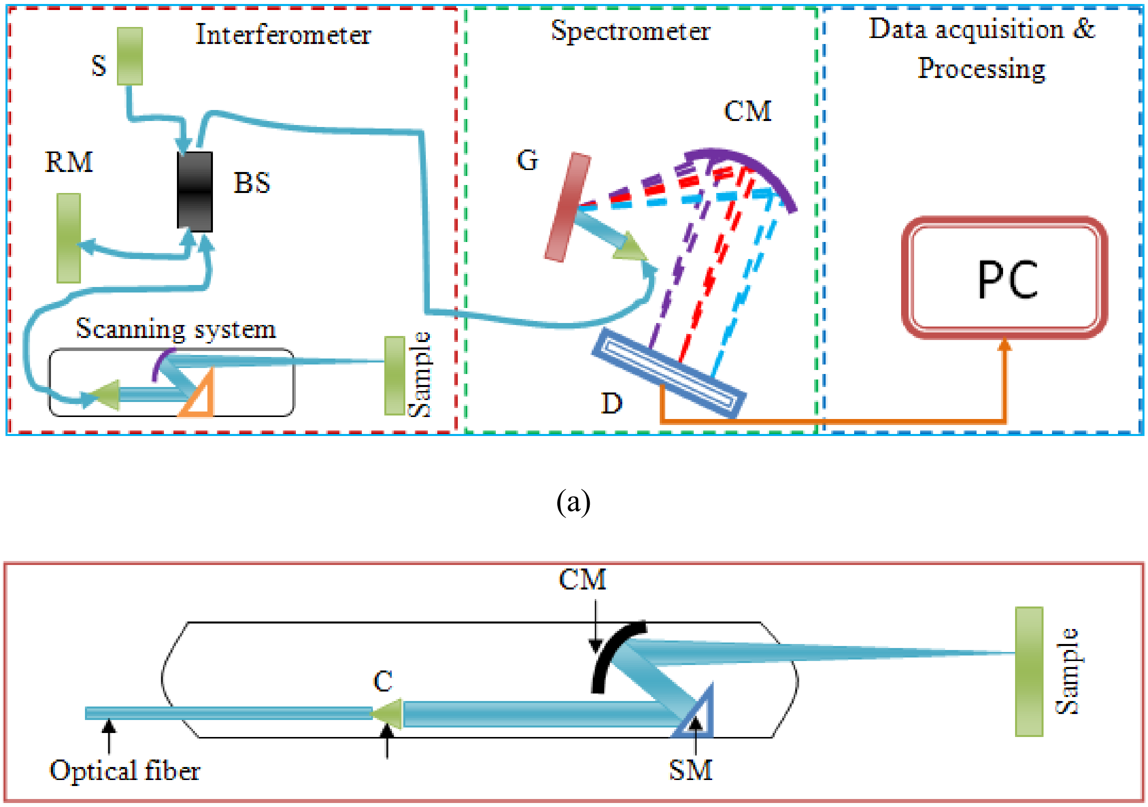

(a)

(b)

Figure 1.21: (a) Reflective optics based line-scan SD-OCT setup and (b) Scanning system. (S-source, BS-beam splitter, RM-reference mirror, G- Grating, CM-Cylindrical mirror, CM-cylindrical mirror, SM-scanner mirror, C-collimator, and PC-personal computer).

1.13 Organization of the thesis in manuscript-based format

This manuscript-based thesis is organized in seven chapters. In the present chapter, a brief introduction about medical imaging, the history and applications of OCT imaging, a literature review, the motivation, the scope and objective of this thesis are presented. The comprehensive but brief literature review includes the basic principle of OCT, scanning protocols, overview of the line-scan OCT system, OCT system design requirements, and imaging quality matrix. Chapter 2 to Chapter 6 are duplicated from three published conference articles, one published journal article, and two submitted journal articles. The chapters are organized in a cohesive manner to address the objectives of the thesis defined in Section 1.11 and formatted according to “Thesis Preparation and Thesis Examination Regulations (version-2011)” of the School of Graduate Studies at Concordia University. In the duplicated articles, sections, figures, equations, and tables are numbered according to the thesis preparation regulations. A single comprehensive reference list rather than individual papers reference list is presented in Reference section. Conclusions of the thesis and the future recommendations are presented in Chapter 7.

Chapter 2 is based on the following article presented in Photonics North 2009 conference and published in the SPIE proceedings [90].

Kamal M., Narayanswamy S., and Packirisamy M., “Optical modeling of a line-scan optical coherence tomography system for high-speed three-dimensional endoscopic imaging”, Proceedings of SPIE Vol. 7386, 738607

The optical and analytical modeling of a line-scan optical coherence tomography (LS-OCT) system for high-speed three-dimensional (3D) endoscopic imaging is reported. To avoid complex lens system and image distortion errors, an off-axis cylindrical mirror is used for focusing the line illumination on the sample surface and a micro mirror scanner is integrated with the proposed configuration for transverse scanning. The beams are swept on the cylindrical mirror by the micro mirror rotation and finally focused on the sample surface for transverse scanning. A 2mm by 3.2mm en-face scanning is configured with a 2mm focused line and ±3° scanning mirror rotation. The proposed configuration also has the capability of dynamic focusing by the movement of the cylindrical mirror without changing the transverse resolution. The cylindrical mirror enhances the image quality by reducing the aberration. The system is capable of real-time 3D imaging with 5µm and 10 µm axial and transverse resolutions, respectively.

Chapter 3 presents the following article published in the Journal of Applied Optics [79]. *Kamal M., Narayanswamy S., and Packirisamy M., "Optical design of a line-focused forward-viewing scanner for optical coherence tomography", Appl. Opt.* ***49,*** *6170-6178 (2010).*

Optical design of a line focused forward-viewing optical coherence tomography (OCT) scanner for high-speed endoscopic imaging is reported. To avoid complex lens system, an off-axis cylindrical mirror is used for focusing the line illumination onto the sample surface. Due to its insensitivity to broadband spectrum, mirror focused scanner improves the image quality compared to the lens focused scanner. In this work, a feasibility study is carried out to use reflective optics focused line scanner in OCT imaging instead of the traditional refractive optics scanner. Strehl ratio, chromatic focal shift and field analysis were carried out for plano-convex cylindrical lens, achromatic cylindrical lens and cylindrical mirror focused scanners. The ZEMAX optical modeling analysis show that mirror focused scanning provides better Strehl ratio in comparison to plano-convex cylindrical lens focused scanning and the Strehl ratio is comparable to achromatic cylindrical lens focus scanning. However, field analysis on the edges of the focusing elements within the scan range, show that mirror focused scanning more robust when compared to the cylindrical achromatic lens. Overall, mirror focused scanner shows better performance compared to lenses.

Chapter 4 presents two articles presented in Photonics North 2010 [91] and in Photonics North 2011[92] conferences, and also signal processing of line-scan SD-OCT.

Since this chapter contains two conference proceedings publications, the contents have been modified to reduce repetitions. Section 4.1 presents modified introduction from two papers. Section 4.2 presents the following article presented in Photonics North 2010 conference and published in the SPIE proceeding.

Kamal M., Narayanswamy S., and Packirisamy M., "Design of a spectrometer for all-reflective optics based line scan Fourier domain optical coherence tomography", Proceedings of SPIE Vol. 7750, 775020 (2010)

Optical design of a spectrometer for all-reflective optics based line scan Fourier domain optical coherence tomography (FD-OCT) imaging has been reported in this work for high-speed scanning. FD-OCT imaging data acquisition offers significantly improved imaging speed in the depth direction compared to conventional time domain optical coherence tomography (TD-OCT). On the other hand, line focused scanning improve imaging speed in the transverse direction compare to commonly used flying spot scanning. Combination of FD-OCT acquisition and line focused scanner can give higher imaging speed. Spectrometer is a critical sub-module in FD-OCT system. Apart from the spectrometer optical resolution, and detector array resolution, the chromatic aberration should be considered to design a high-quality FD-OCT imaging spectrometer. The proposed imaging spectrometer consists of a planer reflective grating, off-axis parabolic cylindrical mirror and a CCD array detector. Mirror focusing reduces the chromatic aberration because of its insensitivity to the wavelength of the laser beam, therefore the spectrometer image quality enhanced by the reflective optics focusing. Spot profile fall-off characteristic was analyzed by using ZEMAX optical design software.

Section 4.3 presents the following article presented in Photonics North 2011 conference and to be published in SPIE proceedings.

Kamal M., Narayanswamy S., and Packirisamy M., "Design of spectrometer for high-speed line field optical coherence tomography" Paper number: PN11-PN100-51(in press)

The quality of the spectrometer affects the sensitivity fall-off, axial resolution, and depth scan range, therefore overall performance of the spectral domain optical coherence tomography (SD-OCT) imaging. Chromatic aberration, optical resolution, and detector array resolution are the key design consideration for high-quality OCT spectrometer. Traditionally refractive optics spectrometer is used in SD-OCT. In the present work, the optical design of the reflective optics spectrometer and of the refractive optics spectrometers is reported for high-speed line field optical coherence tomography imaging. The performance of the spectrometers was compared by using the ZEMAX optical design software. The ZEMAX optical modeling analysis shows that the reflective optics spectrometer provides better performance by comparison with the refractive optics spectrometer.

Section 4.4 presents an analytical model of line-scan SD-OCT signal processing, algorithm of signal processing, and construction example of A-scan profile (unpublished work).

Chapter 5 presents the following article submitted to Journal of Optics [93].

Kamal M., Narayanswamy S., and Packirisamy M., "An off-axis cylindrical mirror focused line scanning system with high imaging quality for broad spectral band", Manuscript ID - JOPT/400149/PAP/148632 (Accepted on August 22nd, 2011).

An ultra-broad bandwidth light source is utilized in optical coherence tomography (OCT) for an ultra-high axial resolution. A lens-focused scanning system is commonly used in the OCT imaging. The effective focal length of the lens varies as a function of the wavelength and hence it focuses a broadband spectrum in different focal planes. This variation eventually reduces the axial resolution of the OCT imaging. These variations become even more significant at higher transverse resolution. In the present article, a cylindrical mirror-focused line scanning system for high quality imaging is presented. The imaging quality of the developed system was evaluated using optical design software and tested experimentally with 50.8mm and 25.4mm focal length cylindrical mirrors. A broadband light source with a center wavelength of 843nm and a spectral bandwidth of 53nm was used. The scanning system meets the Marechal criterion by providing a high Strehl ratio (SR) within the 2mm target scan range. Moreover, the developed cylindrical mirror focused scanning is robust and insensitive to minor beam path variations and this was proved experimentally.

Chapter 6 presents the following article submitted to Journal of Biomedical Optics [94].

Kamal M., Narayanswamy S., and Packirisamy M., "Optimized off-axis cylindrical mirror-focused line-scanning system for OCT imaging applications", Manuscript ID-JBO 11373 (under review).

The parameters of an off-axis cylindrical mirror-focused line-scanning system were studied to optimize the flatness of the 2mm scan field. The scanning system parameters included the beam size, the distance between the scanning and the focusing mirror, the angle between the incident beam and the reflected beam, the optical scan angle, and the effective focal length of the cylindrical mirror. Because of the off-axis line-scanning system configuration, the scanning could be carried out either in the tangential (Y-scan) or in the sagittal (X-scan) plane. A 53nm spectral bandwidth light source was used to evaluate the imaging performance of the scanning system. Since reflective optics is employed in this work for focusing, the scanning system could be used with a higher spectral bandwidth light source for optical coherence tomography (OCT) applications. The effect of angle between of the incident and reflected beams, distance between the mirrors, focal length of the cylindrical mirror, and scanning directions, on the flatness of the scan field were studied. It was proved that the sagittal scanning is least sensitive to variations in scanning system parameters and thus it provides maximum flexibility in design.

Chapter 7 presents conclusion summary of the thesis work and future recommendations.

Chapter 2: Analytical modeling of a line scanning system

This chapter is based on an article published in SPIE conference proceedings [90]. This chapter covers the objective '1a' and '1b' of the "Objective and scope of the thesis" in Section 1.11.

2.1 Introduction

Optical coherence tomography (OCT) is a rapidly expanding technology in biomedical imaging because it allows real-time, *in vivo* imaging of tissue morphology and pathology without any post processing of the specimens [4]. Axial resolution, transverse resolution, depth of focus, sensitivity etc. are the characteristic parameters for designing an OCT system. Axial resolution of an OCT system define by $\Delta z = \frac{2\ln 2}{\pi}\frac{\lambda^2}{\Delta\lambda}$, where $\Delta\lambda$ is the bandwidth and λ is the center wavelength of the light source; and transverse resolution define by $\Delta y = \frac{4}{\pi}\frac{\lambda f}{D}$, where f is the effective focal length of the objective and D is the spot size in the objective. Therefore, axial resolution depends on the light source spectral bandwidth and transverse resolution depends on the numerical aperture (NA) of the focusing optics. Besides, depth of focus $2z_R = \Delta y^2/\lambda$ of OCT imaging also depends on the NA, which is typically 2 to 3mm. However, depth of focus decreases proportionally while transverse resolution increased with high NA focusing system. Hence, there have a trade-off between the depth of focus and the transverse resolution. Higher transverse resolution with extended depth for three-dimensional imaging can achieve by the dynamic focusing [2, 95]. In addition to the extended scan depth high-speed required for three-dimensional *in vivo* imaging.

High-speed scanning is essential to reduce or omit the motion artifacts of the image, for example eye motion, body motion etc. Parallel detection, which includes line-scan [47, 48, 52, 53] and full field [96], is a recently developed technology for high-speed scanning. In contrast to traditional OCT, where a flying spot modulates in transverse directions by a two-axis scanner onto a target to generate *en- face* image data. Line-scan OCT (LS-OCT) acquires *en-face* image data by modulating a focused line onto the target in one direction therefore only 1D scanner is required, which tremendously enhance the scanning speed [47], as well as reduce the scanning distortion errors [45]. Most of the developed LS-OCT systems implemented either external sample movement [48] or galvanometer [47, 86] mirror for transverse scanning. Therefore, these systems are bulky and impractical for endoscopic scanning.

A wide variety of endoscopic OCT (EOCT) probe configurations has been developed, including forward scanner, side scanner and circumferential scanner [28]. These EOCT probes could be integrates with other existing biomedical imaging tools or use independently for *in vivo* imaging. The developed EOCT probes use either pre-objective configuration where the scanning mirror placed before the focusing lens or post-objective scanner configuration where scanning mirror placed after the focusing lens. These types of configurations either need complex lens system design or give a curve scan field. Moreover, aberrations also reduce the image quality from these configurations. A parabolic mirror focusing configuration, which is commonly use in the laser printer [88], the astronomical telescope [97], the X-ray collimator [89], and the confocal microscopy [78], can be used in the OCT system for focusing the line beams, flat scan field. Mirror focusing also reduces the chromatic aberration because of the insensitivity to the wavelength of the laser beams [77, 78], therefore image quality can be enhanced by the reflective optics focusing system.

In this chapter, the use of off-axis parabolic cylindrical mirror in the optical design of a forward scanning system with line focused for EOCT scanning that is capable to high-speed there-dimensional OCT imaging is presented. Motion artifacts and distortion reduced by the high-speed line scanning and the image quality enhanced by the reflective optics. To the best of authors' knowledge, this is the first demonstration of the reflection optics focused LS-OCT design for high-speed EOCT scanning.

2.2 Endoscopic OCT model

An Endoscopic OCT (EOCT) scanner is a complex optomechanical system. The main optical function of the EOCT scanner is to deliver and focus the incoming beam onto the target sample, and collect the backscattered light from the sample and back to detector through the beam splitter for processing and reconstruction. In view of mechanical design, the main purpose of the EOCT scanner is to modulate the beams onto the sample for lateral scanning. Essential mechanical requirements of an EOCT scanner probe are probe size; scanning rate and target scan rage. Probe size depends on associated mechanical components of the probe such as mirror. Micro-electro-mechanical (MEMS) mirror can be used to miniaturize the endoscopic OCT system. MEMS mirror size is not only the controlling factor for the EOCT probe size but also the target scan range. The scanning rate is another important issue because of high-speed requirements for endoscopic imaging. . Scan angle of the scanner and the effective focal length of the focusing mirror optimization are essential to maximize the scanner scanning performance and minimize the probe size for a target scans range. Reflective optics based OCT scanner analytical modeling, optical modeling, and system performance analysis are presented in this chapter.

2.2.1 Mathematical model

Consider the scanner configuration as shown in Figure 2.1(a) laser beam incident on a scanner mirror N is reflected onto a parabolic cylindrical mirror at a point O, which is finally focused onto the target at R. Here the parabolic cylindrical mirror works as an f-θ mirror, therefore a focusing mirror. Angle between the incident and the reflected beams for both mirrors is 'ϕ'. Distance between two mirrors is d and effective focal plane position of the focusing mirror is at a distance f. If the scanner mirror modulates the beam at an angle θ at P (z, y) with respect to z-y coordinate system (P (Z, Y) with respect to Z-Y coordinate system), it is focused onto the target sample at Q on the focal plane of the focusing mirror. Due to the optical beams modulation at an angle of θ or the scanner mirror rotation $\theta/2$, the focused line position shifted from R to Q, which essentially gives the image height or scan length L_s. Coordinate transformation for scanner parameter formulation is shown in Figure 2.1(b).

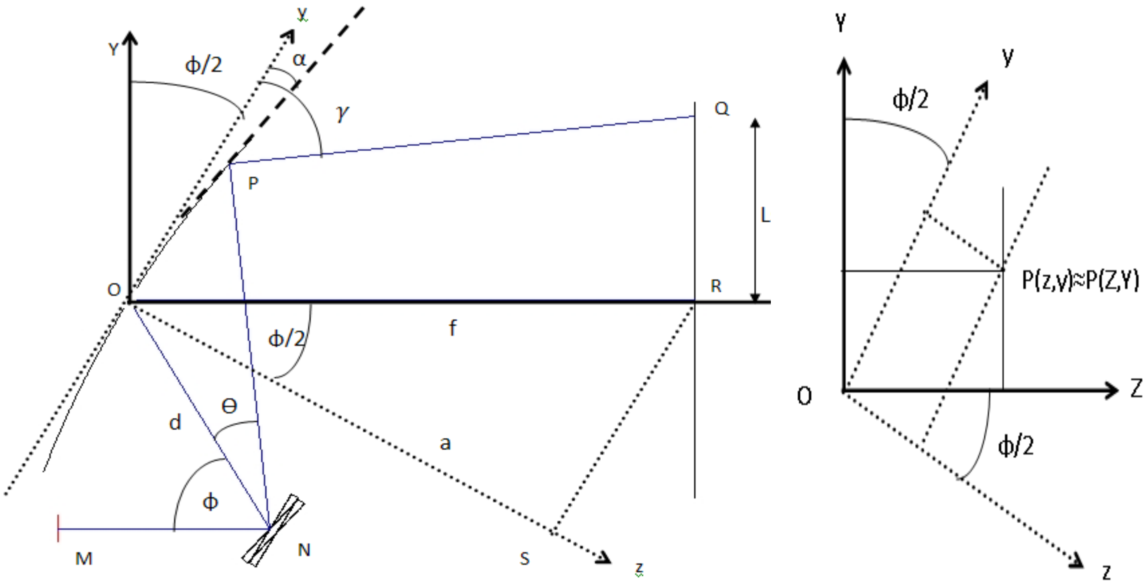

(a) (b)

Figure 2.1: a) Scanner configuration; b) Coordinate transformation

The effective focal of the focusing mirror is *f*, a toroidal surface [98] is used as parabolic mirror, which is described as:

$$z = \frac{cy^2}{1+\sqrt{1-(1+k)c^2y^2}} \tag{2.1}$$

Here, conic constant for parabolic surface, $k=1$ and the curvature $c = \frac{1}{r} = \frac{1}{2a}$, where, $a = f\cos(\phi/2)$, because of the off-axis configuration.

From equation (2.1),

$$z = \frac{y^2}{4a} \tag{2.2}$$

Now, tangent at point P is,

$$\tan\alpha = \frac{dz}{dy} = \frac{y}{2a} \tag{2.3}$$

From the scanner geometry,

$$\frac{y + z\tan\left(\frac{\phi}{2} + \theta\right)}{\sin\theta} = \frac{d}{\cos\left(\frac{\phi}{2} + \theta\right)} \tag{2.4}$$

By substituting z in Equation (2.4)

$$y + \frac{y^2}{4a}\tan\left(\frac{\phi}{2} + \theta\right) = \frac{d\sin\theta}{\cos\left(\frac{\phi}{2} + \theta\right)}$$

$$y^2 + y\left(4a\cot\left(\frac{\phi}{2} + \theta\right)\right) = \frac{4ad\sin\theta}{\sin\left(\frac{\phi}{2} + \theta\right)}$$

$$y = -2a\cot\left(\frac{\phi}{2} + \theta\right) + 2\sqrt{a^2\cot^2\left(\frac{\phi}{2} + \theta\right) + \frac{ad\sin\theta}{\sin\left(\frac{\phi}{2} + \theta\right)}} \tag{2.5}$$

Now, considering the Figure 2.1(b) for coordinate transformation from z-y to Z-Y coordinate system:

$$Z = y\sin(\phi/2) - z\cos(\phi/2) \tag{2.6}$$

$$Y = y\cos(\phi/2) - z\sin(\phi/2) \tag{2.7}$$

Again, the angle of incident at point P = angle of reflection $= \left(\left(\frac{\phi}{2} + \theta\right) - \alpha\right)$

The gradient angle γ of the reflecting laser beam given by, $\gamma = \frac{\pi}{2} - \left(\left(\frac{\phi}{2} + \theta\right) - \alpha\right)$

$$\tan\left(\frac{\pi}{2} - \frac{\phi}{2} - \gamma\right) = \frac{L_S - Y}{f - Z}$$

$$L_s = Y + (f - Z)\tan(\theta - 2\alpha) \tag{2.8}$$

Scan length L_s can be calculate from Equation (2.8) by substituting α, Y and Z from Equation (2.3), (2.6) and (2.7) for any scan angle of θ and effective focal length f. The EOCT probe was designed to be used in a LS-OCT system that operates with a laser source of 1060nm center wavelength and 100nm spectral bandwidth, corresponding to 5µm theoretical axial resolution. The scanner mirror placed at angle *(ϕ)* of 20º with the collimated laser beam. A 14.93mm effective focal length *(f)* focusing mirror placed at a distance *(d)* of 10mm from the scanner mirror. By using above mathematical formulation for the scanner, for a scan angle ($\theta/2$) of ±3º the theoretical scan length (L_s) is 3.02mm. In order to verify the scanner analytical model ZEMAX optical modeling program is utilized. A 2mm incident beam used in this configuration that gives 10µm transverse resolution with the current focusing configuration.

2.2.2 Optical model

ZEMAX optical design program used for optimization of the scanner performance. The program contains features and tools to design, optimize, and analyze any optical system [98]. Effective focal length of the focusing mirror, and the distance between focusing and scanner mirror, optimized for best focal line position for scanning a target scan length with a scan angle of ±3º. These optimized parameters ultimately fixed the minimum size of the scanner mirror and the focusing mirror therefore size of the entire EOCT probe for a particular beam size. In ZEMAX lens data editor, the focusing mirror surface defined with “Toroidal” surface types and the scanning mirror surface defined with “Standard” surface types. Radius, thickness values between surfaces and conic constant of the toroidal surface needed in lens data editor. In order to determine the best focusing performance, the focusing mirror radius of curvature, thickness (effective focal plane distance), and distance between the scanner mirror and the focusing mirror was defined as a variable. A 2 mm diameter pupil “Gaussian” apodization types, conic constant [98] “-1” for parabolic surface and default “Merit Function” defined for best focusing performance optimization. First, the model was optimized for 13 different focal plane positions of within scan angle from -3° to +3° with an interval of 0.5° for the best-focused line position. Figure 2.2(a) shows the optical model of the scanner configuration and Figure 2.2(b) shows ZEMAX shaded model. Focal plane position variation with in this scan range discuss in the performance analysis section.

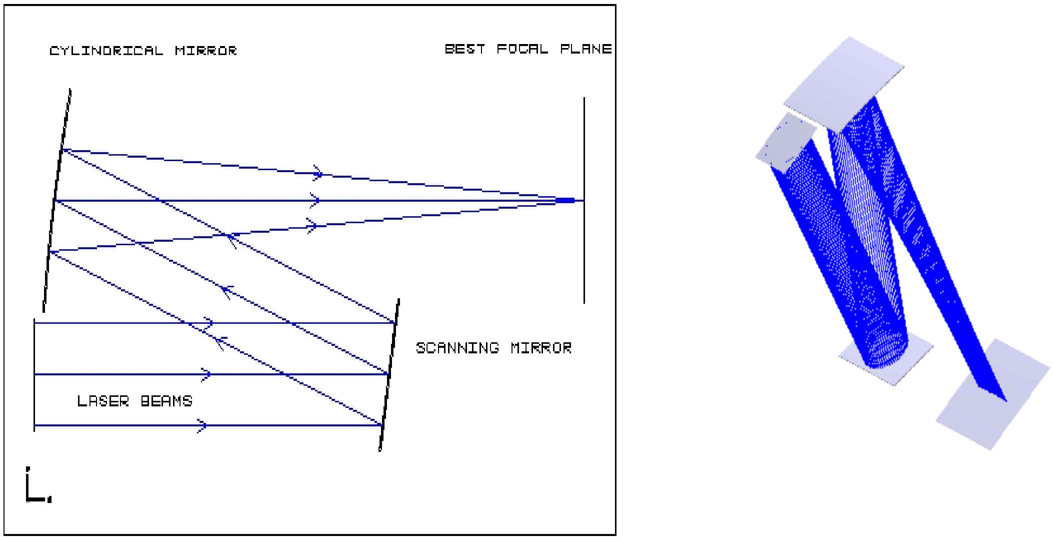

(a)

(b)

Figure 2.2: (a) Scanner layout of ZEMAX model, (b) ZEMAX shaded model of focused line on best focal plane

Again, the model was optimized for best focused with a fixed focused line position for the same scanner scan positions, detail result presented in the performance analysis section. Figure 2.3(a) shows the optical arrangement of the ZEMAX model, two extreme ends, and one arbitrary position within the scans range. Figure 2.3(b) shows the scans rage in the ZEMAX shaded model. This optimization gives scan range of 2mm×3.20mm for scanner scan angle of ±3° with a 2mm beam size. The Strehl ratio for these optimizations recorded for each scanner position, which also discuss in the performance analysis section.

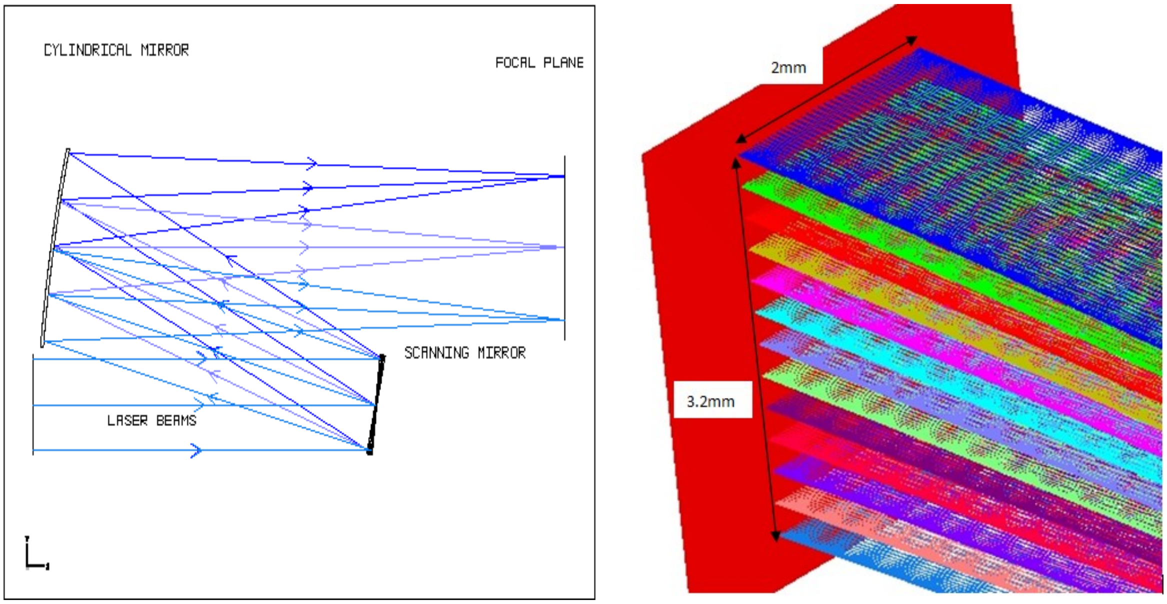

(a) (b)

Figure 2.3: (a) Scanner layout of ZEMAX model, (b) ZEMAX shaded model of focused line configuration on the image plane

2.3 Performance analysis

The performance of the optical system expressed in various ways. The spot diagram, modulation transfer function (MTF), encircled energy, Strehl ratio, irradiance distribution, ray aberration etc. [60, 75, 76], most commonly used for performance analysis. For the proposed EOCT imaging system, scan field flatness also a parameter for the system performance evaluation. One of the objectives of this work is to implement the reflective optics focusing instated of pre-objective/ post-objective scanner configuration for flat scan field and reduces the data processing complexity. Due to the flat scan field the imaging system also maintain a constant transverse resolution throughout the scans range. For, λ=1060nm, $\Delta\lambda$=100nm, D=2mm and ZEMAX optimized the best focal plane position f=14.93mm and axial resolution 5µm and transverse resolution 10µm. The aberration characteristic of the system was measured from the ZEMAX model in terms of Strehl ratio, which is varies from 0.967 to 0.998 within the scan rage of ±3º. Figure 2.4(a) shows the system depth of scan range from ZEMAX model. Minimum spot size and two extreme ends of the depth of focusing range indicated by A, B' and B'' respectively in both figure. Depth scan range of the system is 150µm with current configuration. Beyond this range, the beams are more diverging which was verified by the ZEMAX defocus analysis as shown in Figure 2.4(b).

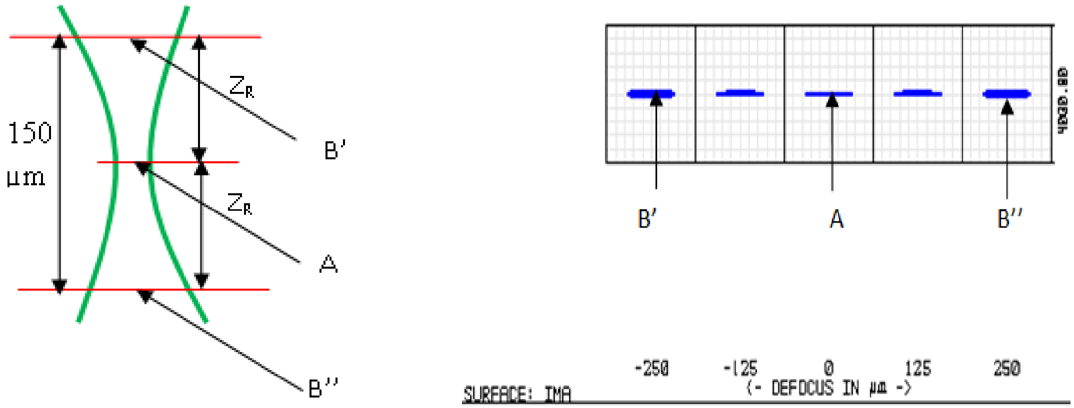

(a) (b)

Figure 2.4: (a) Depth scan range and (b) Spot diagram in depth scan range.

Figure 2.5 shows the variation of the effective focal plane or scans field flatness of the proposed scanning system. With the present configuration, for ±3° scanning angle the scan range is 2mm×3.2 mm and the effective focal plane positions variation is 9µm. This gives a very good argument for the scan field flatness because the depth scans range is 150µm with the current configuration.

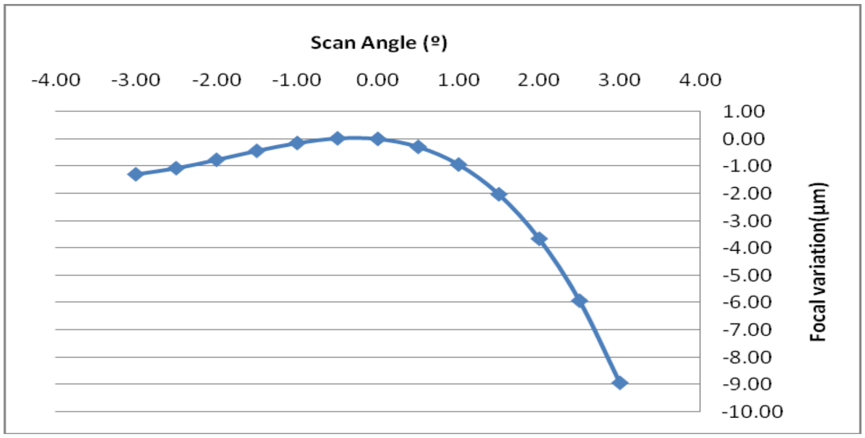

Figure 2.5: Scan field flatness.

2.4 Conclusions

A line scan EOCT (LS-OCT) imaging probe analytical and optical design demonstrated for high-speed scanning. Theoretical scans range 2mm×3.02mm for scan angle of ±3º but ZEMAX gives the scans range of 2mm×3.2mm for the same scan angle. The variation between the analytical and optical model scans rang approximately 5%. With the current focusing configuration the depth of scan range 150µm, which can be extend dynamically by moving the focusing mirror for three-dimensional imaging. The axial and transverse resolution of the proposed EOCT imaging system is 5µm and 10µm, respectively. Future work includes reflective optics based spectrometer modeling for building all-reflective optics EOCT imaging system.

Having completed the mathematical modeling of the reflective optics based line scanner, optical simulation and comparison of the imaging performance with refractive optics based line scanners is presented in the following chapter.

Chapter 3: Optical design of a line scanning system

This chapter is based on the manuscript published in the Journal of Applied Optics [79], where the optical design of refractive and reflective optic based scanning system and performance comparison are presented. This chapter covers the objective ‘1c’ of the “Objective and scope of the thesis” in Section 1.11.

3.1 Introduction

Optical Coherence Tomography (OCT) is a rapidly expanding technology in biomedical imaging as it facilitates real-time, *in vivo* imaging of tissue morphology and pathology without any post processing of the specimens [4]. Axial resolution, transverse resolution, depth of focus, sensitivity, etc. are the characteristic parameters that are used for designing an OCT system. Axial resolution of an OCT system depends on bandwidth and center wavelength of the light source while transverse resolution and depth of focus depend on the numerical aperture (NA) of the focusing optics. Since depth of focus decreases with increase in the transverse resolution while using high NA optics there usually is a trade-off between the two. However, higher transverse resolution with extended depth for three-dimensional imaging can be achieved by dynamic focusing [2, 95]. In addition to the extended scan depth, high-speed is required for three-dimensional real time *in vivo* imaging. High-speed scanning is essential to reduce or eliminate the motion artifacts of the image, such as, eye or body motion. For high speed imaging in OCT, recent works include line-scanning [47, 48, 52, 53] and full field imaging [96]. In contrast to traditional OCT, where a two axis scanner acquires en-face image data by modulating a flying spot onto a target in transverse directions, a line-scan OCT (LS-OCT) acquires en-face image data by modulating a focused line onto the target in one direction. Hence LS-OCT not only enhances the scanning speed [47], but also reduces the scanning distortion errors [45]. However, all the LS-OCT systems developed so far depend either on an external sample movement [48] or a galvo mirror [47, 86] for transverse scanning. Therefore, these systems are bulky and impractical for endoscopic biomedical imaging.

A wide variety of OCT scanner configurations have been reported, including forward scanner, side scanner and circumferential scanner [28]. These OCT scanners could either be integrated with other existing biomedical imaging tools or can be used independently for *in vivo* imaging. The developed OCT scanners use either a pre-objective or a post-objective scanner configuration. In the pre-objective configuration as shown in Figure 3.1(a), scanning mirror is placed before the focusing lens and this type of scanner provides a flat field scanning. However, complex lens system design is required due to off-axis configuration. In the post-objective configuration as shown in Figure 3.1(b), the scanning mirror is placed after the focusing lens. A simple lens system is adequate for this configuration but the resultant scan field is not flat [77]. Another limiting factor with lens focused scanner is the chromatic aberration, where the effective focal length of the lens is wavelength dependent. This is particularly critical in OCT imaging as the light source is required to have a broad spectral range to increase the axial resolution [39]. This issue is usually solved by employing telecentric, aspheric and achromatic lenses in OCT imaging. But, these lenses are expensive, and they require complex design in order to maximize the performance. Mirror focusing is an alternative for OCT imaging as it eliminates chromatic aberration and dispersion.

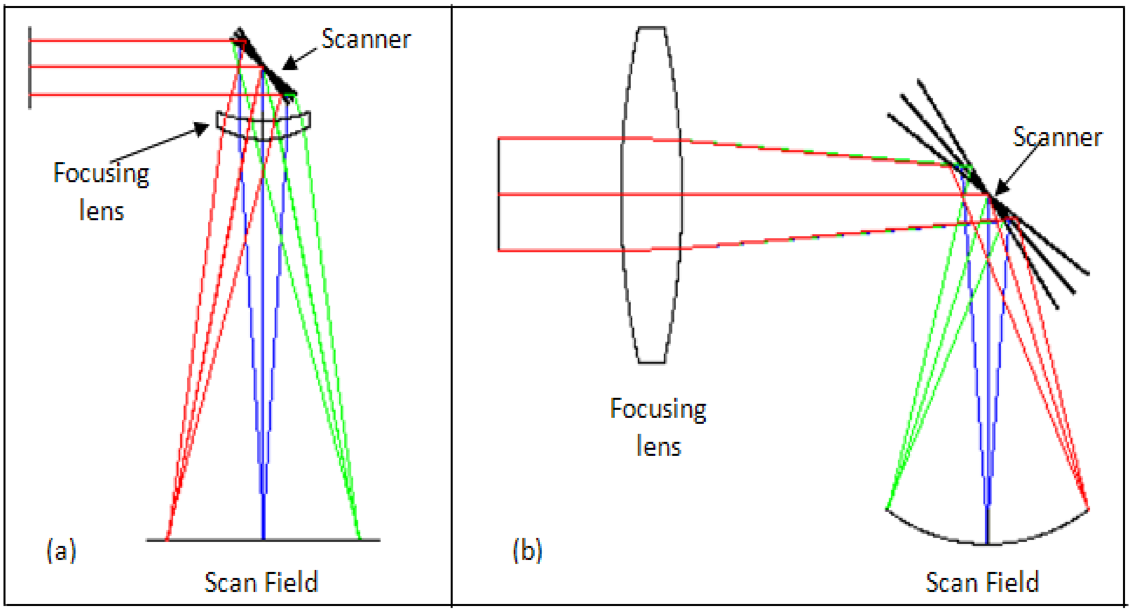

Figure 3.1: (a) Pre-objective scanning, and (b) post-objective scanning.

Mirror focusing eliminates the chromatic aberration due to its insensitivity to wavelength [77, 78], and hence the image quality is enhanced. Parabolic mirrors have been commonly used in laser printers [88], astronomical telescopes [97], X-ray collimators [89], and confocal microscopy systems [78] for focusing the laser beam as a spot. A cylindrical toroidal mirror instead of a cylindrical lens is planned in this work for focusing the broadband beam as a line. This line scanner arrangement not only improves the image quality but also achieves a flat scan field [90].

In this chapter, optical model of a pre-objective plano-convex cylindrical lens and achromatic cylindrical lens focused line-field forward-viewing scanning systems are presented. Mathematical and optical models of an off-axis toroidal cylindrical mirror focused line-field forward viewing scanning system are also presented. Optical design tools of ZEMAX are used to compare the imaging performance of the cylindrical lenses and cylindrical mirror focused scanning systems.

3.2 Plano-convex cylindrical lens focused scanner optical model

Line focused forward-viewing scanner was designed to be integrated with a Fourier domain optical coherence tomography (FD-OCT) system for high speed scanning. An 830nm center wavelength laser source with a spectral bandwidth of 200nm was utilized for the current configuration. Optical layout of the plano-convex cylindrical lens focused forward scanner is shown in Figure 3.2, where a micromirror scanner is placed on the back focal length (BFL) of the cylindrical lens. Five different scanner positions with equal intervals were defined within a scan range of 2mm. The inset in Figure 3.2 shows focused line footprint diagram of these configurations at the imaging plane. Light beam that is reflected at 45° from a fold mirror onto the scanning mirror finally focuses on the focal plane through a cylindrical lens. Distance between the fold and scanner mirror is 10mm. ZEMAX optical modeling software was utilized to evaluate performance of this configuration.

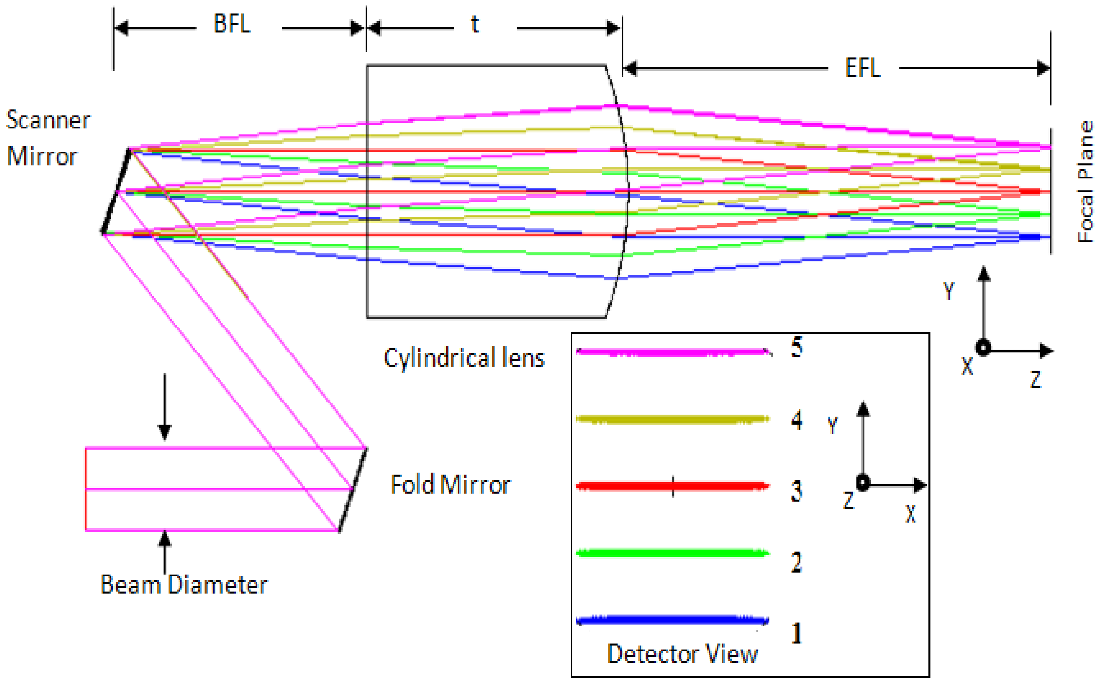

Figure 3.2: Cylindrical lens focus forward-viewing probe (BFL-back focal length, EFL-effective focal length).

Three cylindrical lenses with different effective focal lengths (EFL) of 12.7mm, 25.4mm and 50.8mm were used in the current model for performance analysis. A 2mm diameter pupil with “Gaussian” apodization type and a toroidal surface type with a conic constant of “-1” for the cylindrical lens surface was defined in the ZEMAX model. Specifications of the cylindrical lenses studied in this work are given in Table 3.1. For a particular scan range of 2mm X 2mm, the scanner scan angle or position depends on the EFL of the cylindrical lens as shown in Figure 3.3. For example, to scan a 2mm sample, scan angle is ±2.4° with an EFL of 12.7mm. This angle reduces with the increase in the EFL.

Table 3.1: Plano-convex cylindrical lenses specifications.

EFL (mm)	BFL (mm)	Lens thickness (t) mm	Material	Radius of curvature (mm)	Aperture size (mm)
12.7	7.54	7.83	N-BK7	6.588	6X6
25.4	22.35	4.65	N-BK7	13.175	6X6
50.8	46.68	6.26	N-BK7	26.315	6X6

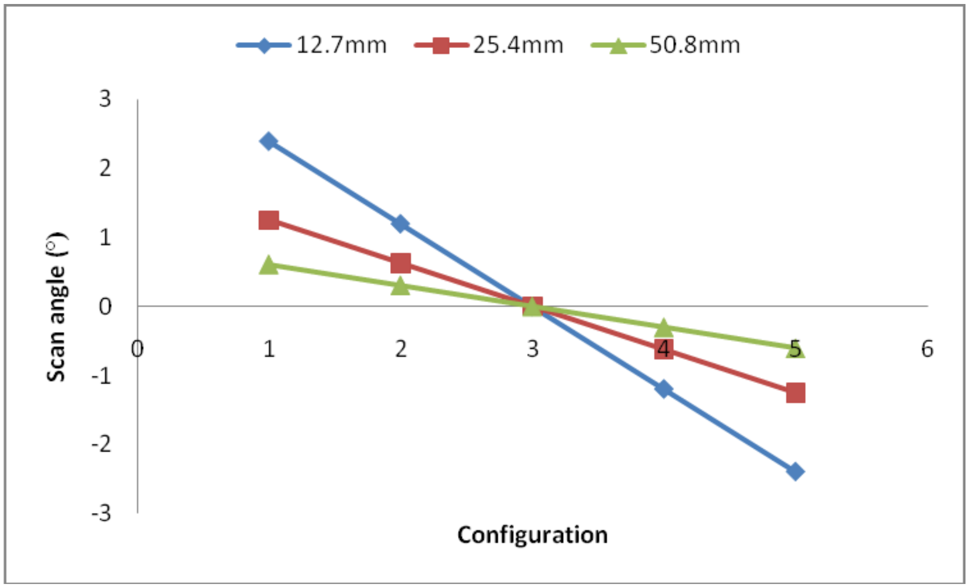

Figure 3.3: Scanner positions with different EFL for a 2mm scan range.

3.3 Performance analysis

The performance of the optical system is expressed in various ways. The spot diagram, illumination distribution, modulation transfer function (MTF), encircled energy, Strehl ratio, aberration, etc. are commonly used for performance analysis [60, 75, 76]. The aberration characteristic of the system with the cylindrical lenses was evaluated using the ZEMAX model in terms of the Strehl ratio and chromatic focal shift of ultra broadband light source, which is critical for imaging quality of an optical system.

Illumination distribution of a focused line in the X and Y directions from the ZEMAX model at scanner position 3 which corresponds to central position in the focal plane is shown in Figure 3.4. Because of the cylindrical lens focusing the line size in the X-axis is same as the pupil diameter and beam size in the Y-axis depends on NA of the focusing system. The Strehl ratio recorded for each scanner position for three EFL lenses is discussed in the following section.

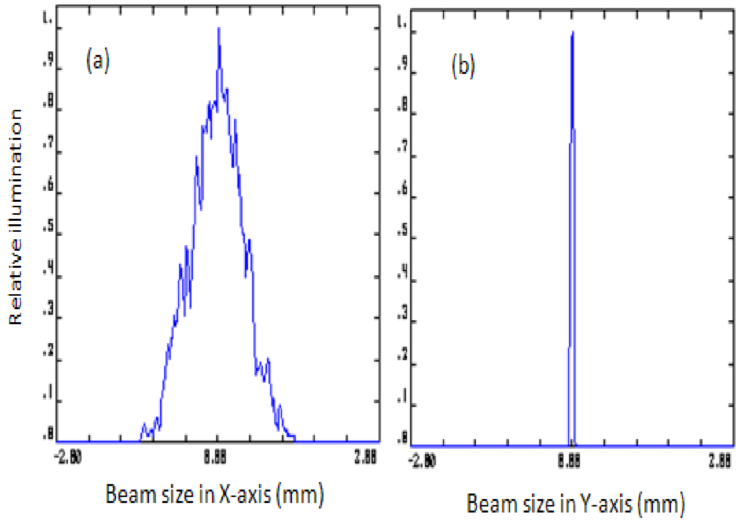

Figure 3.4: Illumination distribution at imaging plane (a) along the line and, (b) in the focusing direction.

3.3.1 Strehl ratio analysis

Strehl ratio is one of the key parameters used for assessing optical system imaging quality [83]. The Strehl ratio is a quantity that provides information about the flatness of the wavefront, and therefore, the quality of the optical system. It is the ratio between the peak intensity of the aberrated point spread function (PSF) of the system to the peak intensity an aberration free PSF [75]. In case of line illumination, line spread function (LSF) is used, and it can be determined by integrating multiple PSF [99]. The Strehl ratio is expressed by $S \approx 1-\left(\frac{2\pi}{\lambda}\right)^2 \sigma^2$ where, σ^2 is the wavefront variance and λ is the wavelength of the source [76]. A Strehl ratio of 0.8 is the Marechal criterion for a good quality optical system [85], and it corresponds to an RMS wavefront error of 0.071 waves (λ /14). Strehl ratio at different positions along the focal plane for a 2mm scan range with three different EFL cylindrical lenses used in this model is shown in Figure 3.5. Dotted boundary in Figure 3.5 indicates the acceptable range of Strehl ratio for high quality imaging based on Marechal criterion. For a 12.7mm EFL the Strehl ratio of 0.661 was achieved at the center of the focusing lens, which is already lower than the Marechal criterion. Strehl ratio decreases further as the beam moves away from the center of the cylindrical lens. However, with lower NA focusing lens, Strehl ratio improves and variation reduces within the scan range. For example, with 50.8mm EFL, the Strehl ratio is better than the Marechal criterion but the transverse resolution is low. As mentioned earlier transverse resolution of an OCT system depends on NA of the focusing system. For cylindrical lenses with EFL 12.7mm, 25.4mm and 50.8mm, the transverse resolution of the system is 6.7µm, 13.4µm and 26.8µm respectively with a center wavelength of 830±100nm and 2mm beam size. Therefore, with higher EFL the Strehl ratio improves while the transverse resolution or image quality of the scanning is reduced. As a result, aspheric, achromatic, or telecentric lenses have to be designed to maintain high imaging quality. Among these, achromatic doublets are the simplest. Hence, optical model and performance analysis of an achromatic cylindrical doublet scanner is presented in the following section to compare the performance with that of cylindrical mirror scanning, which is the objective of this work.

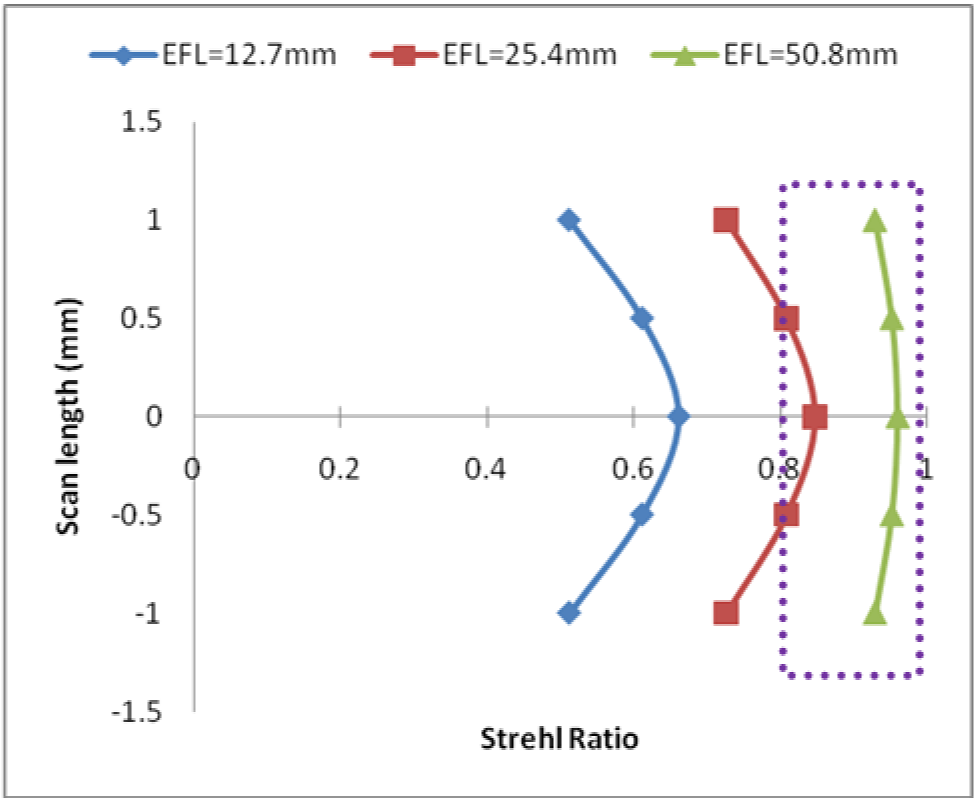

Figure 3.5: Strehl ratio of plano-convex cylindrical lens focused scanner.

3.3.2 Achromatic cylindrical lens scanner

Optical layout of an achromatic cylindrical lens scanner is shown in Figure 3.6. Surface type and beam size used in the achromatic cylindrical lens model are similar to those used in the plano-convex cylindrical lens model. Similar geometrical arrangements and five different scanner positions also used in this model except an achromatic cylindrical lens instead of the plano-convex cylindrical lens. The inset in Figure 3.6 shows focused line footprint diagram for 2mm scan range at the imaging plane. Achromatic cylindrical lens radius of curvatures and thickness are shown in Table: 3.2.

Table 3.2: Achromatic cylindrical lens specifications (in mm)

EFL	BFL	R1	R2	R3	Tc1	Tc2	Material	Aperture size
12.7	7.60	6.75	-4.04	-30.78	3.69	0.72	BK7-SF5	6X6
25.4	17.00	13.64	-8.46	-46.51	4.39	1.86	BK7-SF5	6X6
50.8	46.68	31.69	-22.40	-68.99	3.00	1.50	BK7-SF5	6X6

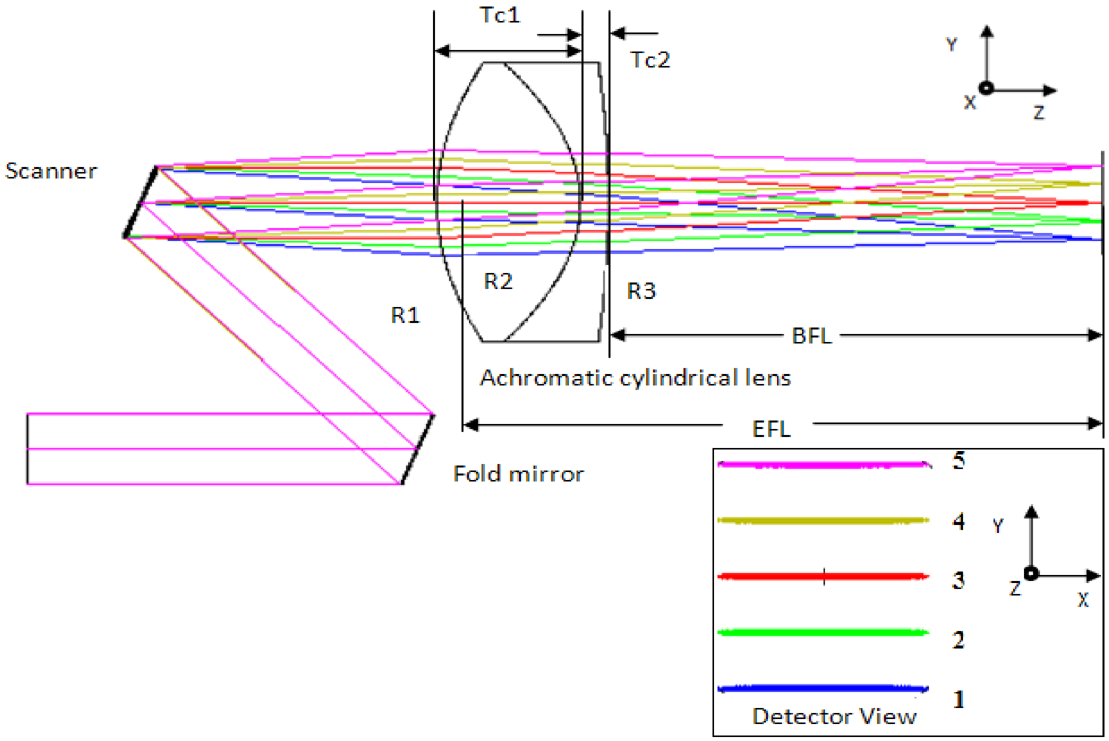

Figure 3.6: Achromatic cylindrical lens scanner.

Achromatic cylindrical lens focused scanners shows higher Strehl ratio compared to the plano-convex cylindrical lens scanners, as shown in Figure 3.7. In this case, Strehl ratio is better than the Marechal criterion for all three EFLs as highlighted by dotted line in Figure 3.7. For a 12.7mm EFL the Strehl ratio falls from 0.994 to 0.826 for a 2mm scan range. With low EFL lenses like 12.7mm, preferred for higher transverse resolution, the radius of curvature decreases significantly, as shown in Table 3.2. Hence, image quality variations are large within the scan range as small as was 1mm from the center. With higher EFL, variation of the Strehl ratio is less within the same scan range but the transverse resolution is low as discussed in the previous section. However, variation of the Strehl ratio due to misalignment is more pronounced and axial resolution degrades due to chromatic focal shift, which are discussed in the later part of this chapter. Alternatively, in this work, an off-axis toroidal cylindrical mirror focused scanner is proposed for high quality OCT imaging within the scan range.

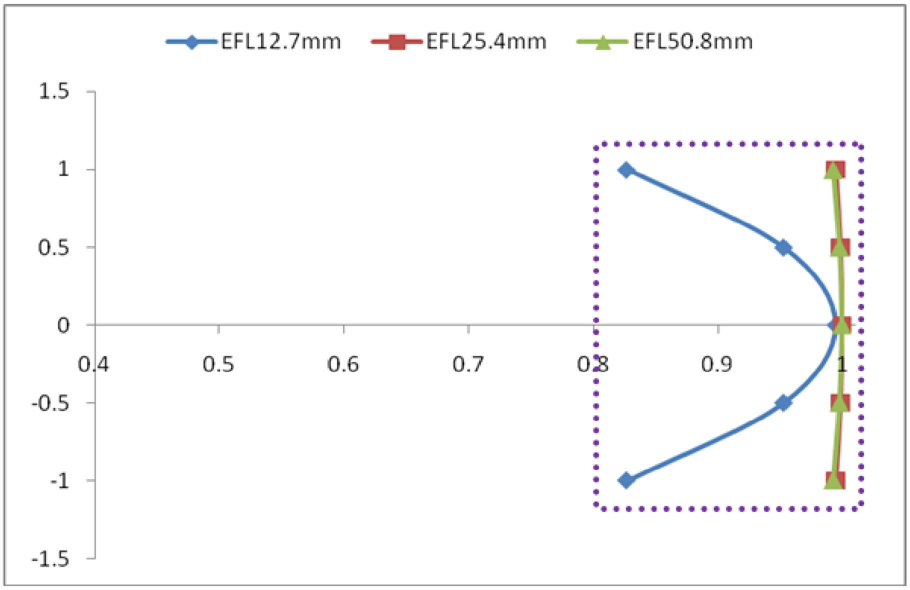

Figure 3.7: Strehl ratio of achromatic cylindrical lens focused scanner.

3.4 Mirror focused scanner model

3.4.1 Mathematical model

Consider the scanner configuration as shown in Figure 3.8, where the laser beam that is incident on a scanner mirror N is reflected onto a toroidal cylindrical mirror at a point O, which is finally focused onto the target at R. Angle between the incident and the reflected beams for both mirrors is ϕ, Distance between two mirrors is d and effective focal plane position of the focusing mirror is at a distance f. If the scanner mirror modulates the beam at an angle θ at P (z, y), it is focused onto the target sample at Q on the focal plane of the toroidal cylindrical mirror.

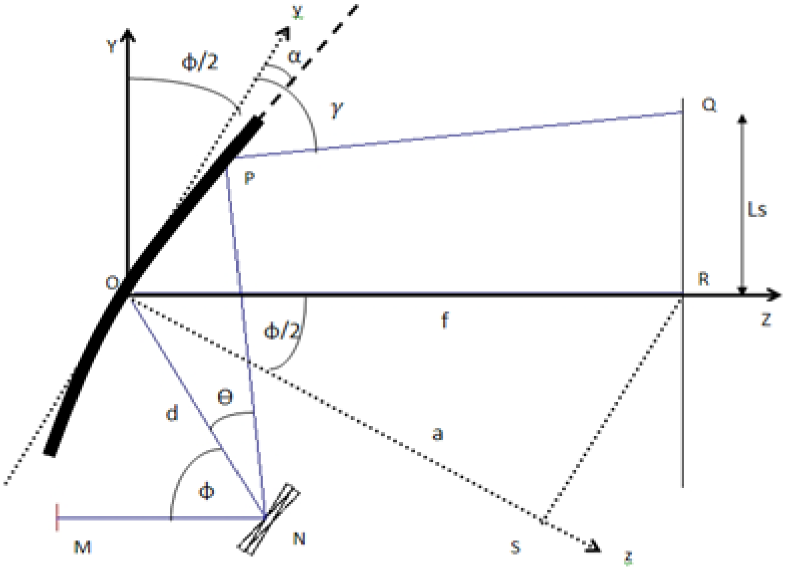

Figure 3.8: Mirror focused forward scanner configuration.

Due to the optical beam modulation at an angle of θ or the scanner mirror rotation of $\theta/2$, the focused line position shifts from R to Q. This essentially decides the scan length L_s which is expressed by the following equation:

$$L_s = Y + (f - Z)\tan(\theta - 2\alpha) \tag{3.1}$$

Detailed mathematical derivation can be found in Chapter 2 [90]. The forward scanner was designed to be used in an LS-OCT system that operates with a laser source of 830nm center wavelength and a 200nm spectral bandwidth. The scanner mirror is placed at an angle *(ϕ)* of 45° with the collimated laser beam of 2mm diameter. A focusing mirror with 12.7mm effective focal length *(f)* is placed at a distance *(d)* of 10mm from the scanner mirror. By using the above formulation, scan length of 2mm is predicted for a scan angle of ±2.4º. ZEMAX software was used to analyze the imaging quality and to validate the mathematical modeling of the cylindrical mirror focused scanner.

3.4.2 Optical model and analysis

Optical layout of the cylindrical mirror focused forward-viewing scanner is shown in Figure 3.9. As explained earlier, five different scanner positions with equal intervals were defined in this configuration within a scan range of 2mm. Surface type and beam size used in the mirror model are similar to those used in the cylindrical lens model. It is important to note that the cylindrical mirror is a negative focal length cylindrical lens coated with a reflective surface and hence the difference in radius of curvature for same EFLs. Similar to the cylindrical lenses, three cylindrical mirrors with different effective focal lengths (EFL) were used for performance analysis and compared with the lens focused scanner. Mirrors specifications are shown in Table 3.3. In this configuration, the collimated light beam first hits the scanning mirror and is reflected at 45° onto the cylindrical mirror, and finally focuses onto the focal plane. In order to scan a sample, light beam modulates onto the cylindrical mirror by the scanner mirror rotation. Scanner rotation eventually determines the final focused beam position on the sample.

Table 3.3: Cylindrical mirrors specifications

EFL (mm)	Radius of curvature(mm)	Aperture size (mm)
12.7	27.518	6X6
25.4	55.090	6X6
50.8	109.996	6X6

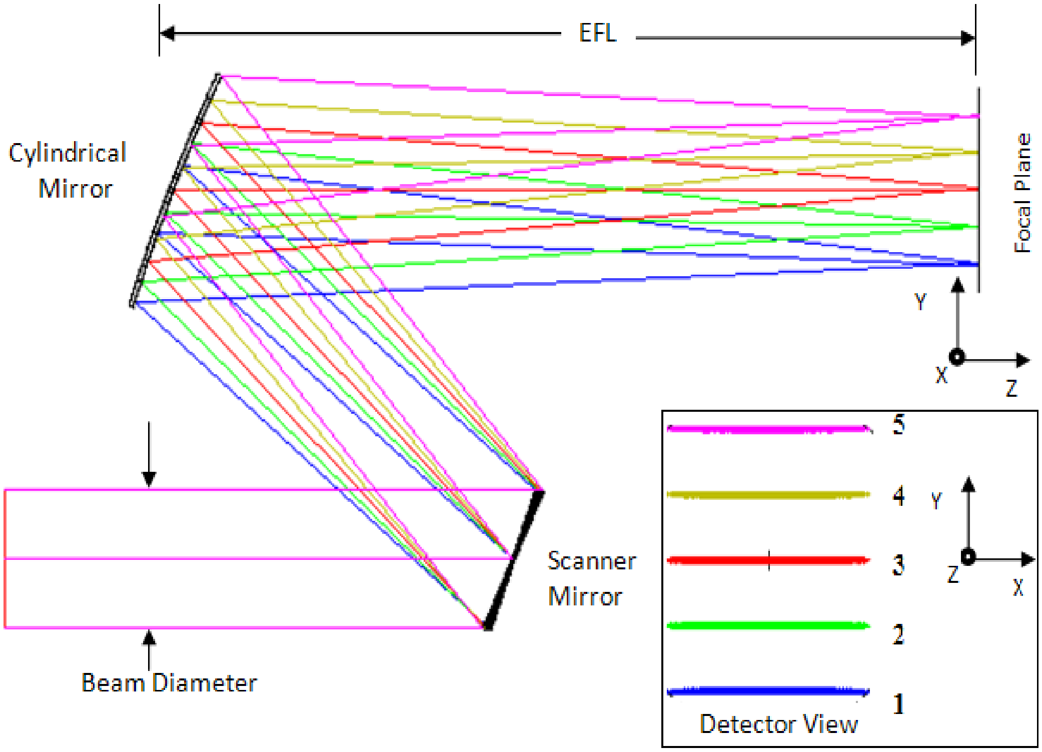

Figure 3.9: Cylindrical mirror focus forward-viewing probe layout.

Detector view of the focused lines at the imaging plane for five different scanner positions is shown as an inset in Figure 3.9. Variation of the Strehl ratio for 2mm scan length with 12.7mm, 25.4mm and 50.8mm EFL cylindrical mirrors focused scanner is shown Figure 3.10. Dotted box in Figure 3.10 indicates the Strehl ratio higher than Marechal criterion.

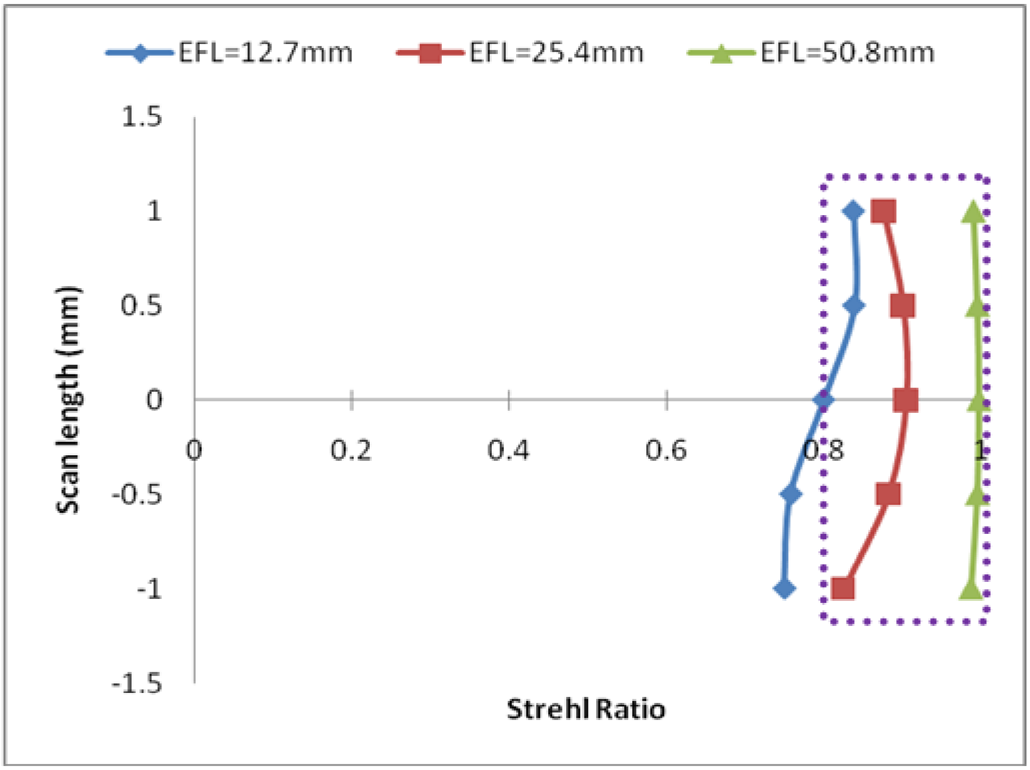

Figure 3.10: Strehl ratio of cylindrical mirror focused scanner.

Overall, achromatic cylindrical lens focusing shows higher Strehl ratio compared to the plano-convex cylindrical lens and the cylindrical mirror focusing scanners. At 50.8mm EFL, the Strehl ratio of lenses and mirror focus shows the closer value but the transverse resolution is low at higher EFL. In case of the plano-convex cylindrical lens focusing scanner, the Strehl ratio drops significantly due to aberration as the beam moves towards the edge of the lens. However, in the case of the cylindrical mirror focusing, the Strehl ratio does not vary significantly. For example, with 12.7mm EFL plano-convex cylindrical lens focused scanner, the Strehl ratio varies from 0.512 to 0.661, which is lower than the Marechal criterion. In case of the achromatic cylindrical lens this variation is from 0.826 to 0.994. While cylindrical mirror focused scanner, the Strehl ratio variation from center to one edge is 0.80 to 0.839 with the same EFL**.** Moreover, due to the off-axis arrangement in case of mirror scanning, the Strehl ratio improves while scanning on one side of the mirror, the variation is lesser as shown in Figure 3.10. For 12.7mm EFL cylindrical mirror, Strehl ratio is better than Marechal criterion in one side of the mirror. This can be further improved by the beam movement towards the mirror optical axis for a larger scan range. The variation of the Strehl ratio is more pronounced for lens focused scanner if there are any beam misalignments. Variation due to beam misalignments has been evaluated by field analysis from the ZEMAX optical model.

Spot profile or signal fall-off at the focal plane of the lens focused scanner becomes worse towards the edge of the focusing lens due to aberration. Therefore, beam alignment at the center of the lens is a critical issue. To compare the signal fall-off characteristics between the cylindrical lenses and mirror focused scanner four different fields at (0°,0°), (0°,1°), (0°,2°), and (0°,3°) were configured. Since cylindrical lens is used variation is in only one axis is consider on the other axis is immune to optical variation. Field's data used for 12.7mm EFL plano-convex cylindrical lens, achromatic cylindrical lens and cylindrical mirror focused scanner is shown in the Figure 3.11. As the beam moves away from the center of the plano-convex cylindrical lens the Strehl ratio drops from 0.671 to 0.633 due to chromatic aberration. However, in the case of the achromatic cylindrical lens, this ratio falls 0.979 to 0.308. While in the case of the cylindrical mirror focusing, the Strehl ratio varies from 0.867 to 0.840. Moreover, in case of the cylindrical mirror, due to the off-axis arrangement, as the field angle increases the beam moves away from the optical axis of the mirror. It accordingly reduces the Strehl ratio and image quality reduction is insignificant, compared to the same situation in lenses focusing.

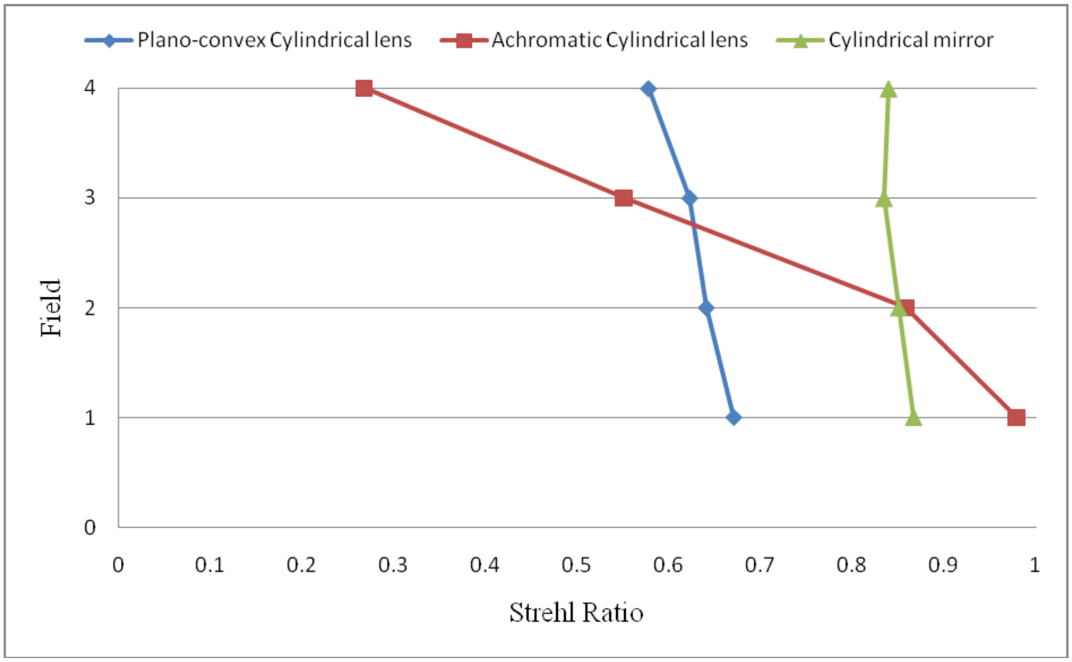

Figure 3.11: Strehl ratio falls off at different fields.

3.5 Chromatic focal shift

OCT utilizes ultra broadband light source for ultrahigh resolution imaging. Unlike traditional microscopy the transverse and axial resolutions of OCT system are decoupled. Transverse resolution depends on NA of focusing optics while the axial resolution depends on the spectral bandwidth of the light source. In the present model, a 2mm diameter beam with 830nm center wavelength and 200nm spectral bandwidth was used for performance analysis. With this laser source theoretical axial resolution is 1.52µm. Effective focal length lens focused scanner varies as a function of wavelength. Therefore, it focuses broadband spectrum at different focal plane which provides lower axial resolution. Because of this focal shift, some of the beam focuses out of scan depth or depth of focus. Figure 3.12 shows the chromatic focal position shift for plano-convex cylindrical lens, achromatic cylindrical lens and cylindrical mirror focusing scanner for the EFL of 12.7mm.For example, depth of focus of the 12.7mm EFL cylindrical lens is 85µm while the chromatic focal shift is 95µm. In case of the achromatic cylindrical lens chromatic focal shift is 20µm with the same EFL. Chromatic focal shift is more pronounced with the higher EFLs. On the other hand, reflective optics focusing is insensitive to the wavelength. Therefore, it focuses broadband spectrum at the same focal plane.

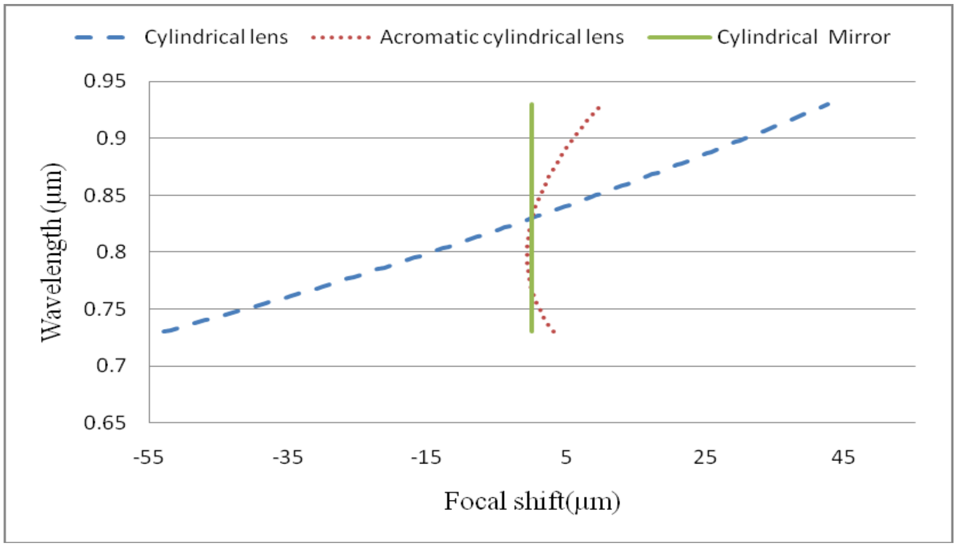

Figure 3.12: Chromatic focal shift for 12.7mm EFL.

3.6 Conclusions

Mathematical model and optical design of an off-axis cylindrical mirror focused forward-viewing OCT scanner for FD-OCT imaging is presented. Optical design of a cylindrical lens focused forward-viewing OCT scanner was also presented, and imaging performance of lens and mirror focusing was compared. Model results show that mirror focused scanner shows better Strehl ratio in comparison to the lens focused scanner. For example, the Strehl ratio improves 21% at the center position with 12.7mm EFL cylindrical mirror while comparing similar EFL cylindrical lens. However, due to the off-axis arrangement, 46.5% improvements in one extreme and 63.7% in the other extremes were achieved with the same EFL. Due to its insensitivity to the broad spectral band of the laser, cylindrical mirror focused scanner maintains higher Strehl ratio throughout the scan range. Results also showed that for a wide field or large scan range, Strehl ratio drops rapidly in the case of the plano-convex cylindrical lens focusing while the cylindrical mirror focusing system maintains high Strehl ratio. While, achromatic cylindrical lens provide higher Strehl ratio, it falls rapidly towards the lens edges especially in the case of lower EFL lenses and the system is highly sensitive to optical alignment. Moreover, achromatic cylindrical lens performance degrades due to chromatic focal shift. Due to its insensitivity to the broadband spectrum, mirror focused scanners provide zero chromatic focal shifts. Moreover, in the case of the beam misalignments, mirror focused scanner provides better performance. Therefore, from the modeling results it can be concluded that for high quality imaging in OCT an off-axis cylindrical mirror scanner is an effective alternative to complex lens scanning systems.

The optical modeling of the proposed line scanner for OCT imaging has been performed in this chapter and its advantage over the refractive optics based scanners has been demonstrated. In the following chapter, the design of the reflective optics spectrometer and the data processing for SD-OCT imaging system are presented.

Chapter 4: Spectrometer design and signal processing

This chapter covers the objective ‘2’ of the Objective and scope of the thesis in Section 1.11 and covers the work published in 2 conference proceedings in addition to some unpublished material. In order to avoid repetition, a modified introduction from two conference papers is presented in Section 4.1. The Section 4.2 covers the objective 2a of this thesis and is based on the material presented in Photonics North 2010 [91]. Section 4.3 covers the objective 2b of this thesis and is based on material presented in Photonics North 2011 [92]. Section 4.4 presents the signal processing of line-scan SD-OCT which covers the objective 2c of this thesis.

4.1 Introduction

The spectrometer is the key component in the development of the spectral domain optical coherence tomography (SD-OCT) system. In SD-OCT, the interference data is acquired through the spectrometer and is then processed by using the Fast Fourier Transform (FFT) method. Spectrometers used for SD-OCT consist of a diffractive grating, a collimating and focusing optic, and a detector array.

Broad spectral band is one of the primary requirements to achieve ultrahigh axial resolution from the OCT imaging. Traditionally, refractive optics is used in OCT imaging to focus the beam in the scanner arm as well as in the spectrometer. Effective focal length of the refractive optics varies with wavelength; therefore, the axial resolution degrades due to chromatic aberration [39, 100-102]. In addition, the major limitation of spectral domain OCT is the depth dependent signal fall-off. The quality of the spectrometer and the image reconstruction method are the two main causes for the signal fall-off in the spectral OCT. Custom designed achromatic lenses [100, 102] are commonly used to minimize the chromatic aberration, which is expensive and require complex design. Reflective optics focusing is an alternative, which is commonly used in laser printers [88], astronomical telescopes [97], X-ray collimators [89], and confocal microscopy systems [78] for focusing the laser beam. It eliminates the chromatic aberration due to its insensitivity to wavelength [77, 78], and hence the image quality is enhanced. Recently, astigmatism-corrected reflective optics-based Czerny-Turner spectrometer configurations with off-the-shelf cylindrical lens have been reported [40, 42]. However, this spectrometer was designed for a flying spot scanning imaging system. Proper optical design and alignment of the spectrometer with appropriate reconstruction method is required to minimize signal fall-off [36, 37].

In the present chapter, optical design of the refractive optics and reflective optics spectrometer for a spectral band of 200nm with a centre wavelength of 830nm is presented. Compare the imaging quality of the designed spectrometers using ZEMAX optical design software. Analytical model of line-scan SD-OCT signal processing also presented in the present chapter.

4.2 Design of reflective optics spectrometer

The proposed all-reflective optics spectrometer consists of a fold mirror, a reflective grating, a focusing mirror and an array detector as shown in Figure 4.1. The light beam first incidents onto the fold mirror and is then reflected at an angle of 45° by the fold mirror towards the reflective grating. The beam is then dispersed into its component wavelengths from the reflective grating. Angle between the incident and the reflected beam from the grating is 30° for the center wavelength which is shown in Figure 4.1. The spectrum dispersed from the reflective grating is focused onto the detector array using a cylindrical mirror. For the purpose of modeling, the distance between the fold mirror and grating is considered to be 15mm, and the distance between the grating and cylindrical mirror is considered to be 20mm, and the effective focal length (EFL) of the cylindrical mirror is 29.8mm.

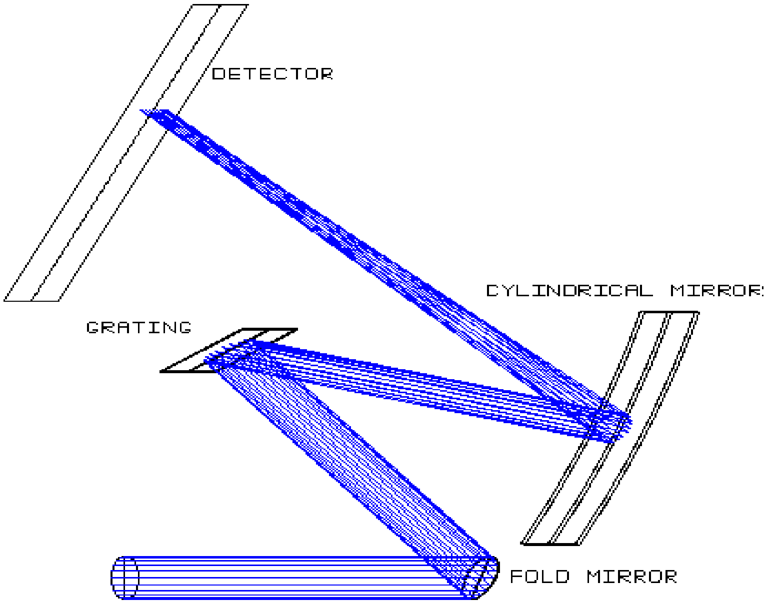

Figure 4.1: Schematic of all-reflective optics spectrometer

4.2.1 Optical design

The optical design of the spectrometer and its ZEMAX ray tracing are shown in Figure 4.2. The spectrometer is designed to be used in the line-scan FD-OCT system. The spectrometer is designed for the spectral bandwidth of 200nm with the center wavelength of 830nm. A 1200 l/mm diffraction grating and 29.8mm EFL cylindrical focusing mirror was used in the designed spectrometer. In the ZEMAX model, a toroidal surface was used for the cylindrical mirror. Conic constant of the toroidal surface was '-1'. For the performance analysis in ZEMAX, five wavelengths 730nm, 780nm, 830nm, 880nm and 930nm were defined. Incident beam of ϕ2mm from the fold mirror to the grating is dispersed according to the wavelengths as shown in Figure 4.2. The dispersed beam is then focused onto the detector, detector view is shown as an insert in Figure 4.2. The array detector of 1920 x 1080 pixels with each pixel having the size of 5µm by 5µm was considered for the spectrometer design. Theoretical resolution of the spectrometer is 0.1nm with a depth scan range of 1.7mm.

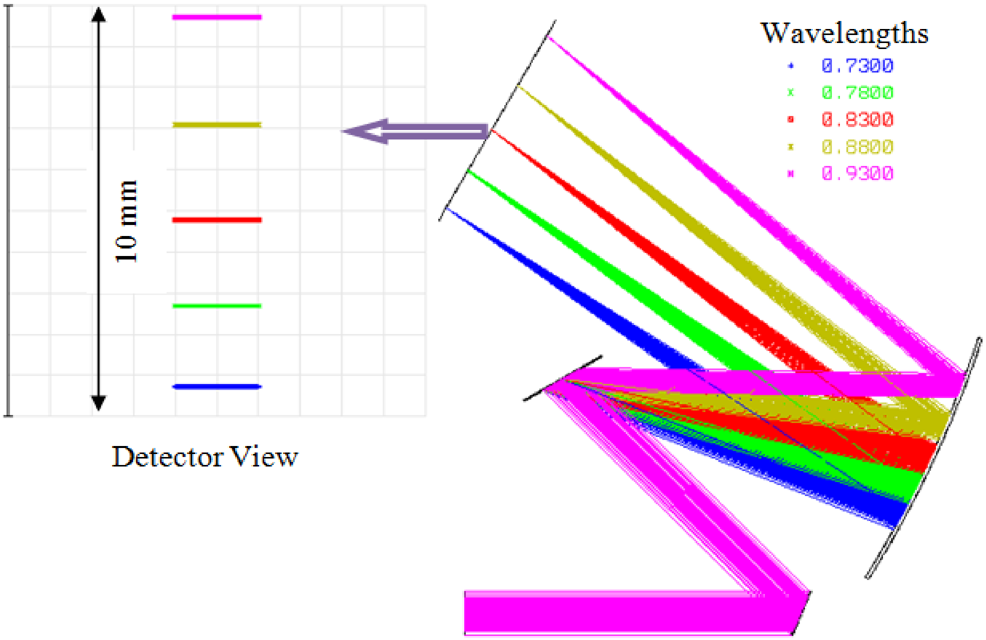

Figure 4.2: Ray diagram illustrating the working of the all-reflective optics spectrometer

4.2.2 Performance measures

In this chapter, a reflective optics spectrometer was modeled to be used with the line focused FD-OCT imaging system with a target scan range of 2mm by 2mm by 2mm. The performance of the designed all-reflective optics spectrometer was evaluated in terms of the Strehl ratio. The Strehl ratio was recorded from the ZEMAX model for the wavelengths of 730nm, 780nm, 830nm, 880nm and 930nm. Figure 4.3 shows the variation of the Strehl ratio for these wavelengths. For 730nm the Strehl ratio is 0.92, and it improves for 780nm. Due to the off-axis arrangement, the Strehl ratio decreases slightly for the higher wavelengths. Another cause of this variation is the angle of the incident and the reflected beam from the grating. However, the Strehl ratio achieved from the ZEMAX model is much better than the Marechal criterion of 0.8 [85]. With the current spectrometer configuration, the depth scan range $\left(Z_R = \frac{1}{4} \frac{\lambda_c^{\,2}}{\delta\lambda} N_x \right)$ is 1.7mm with a spectrometer resolution of 0.1nm and the axial resolution $\left(\Delta z = \frac{2 \ln 2}{\pi} \frac{\lambda^2}{\Delta\lambda} \right)$ of 1.5µm. Depth scan range can be increased by changing the detector size and or the grating l/mm. Alternatively a reduced spectral bandwidth light source can be used to increase the depth range, with a compromise in the axial resolution. Transverse resolution in the line direction $\left(\Delta x = 2 l_s \frac{M}{N} \right)$ is depends on the spectrometer configuration. The comparison of the imaging quality at high transverse resolution in the line direction of the proposed spectrometer to that of the refractive optics spectrometer is presented in the following section.

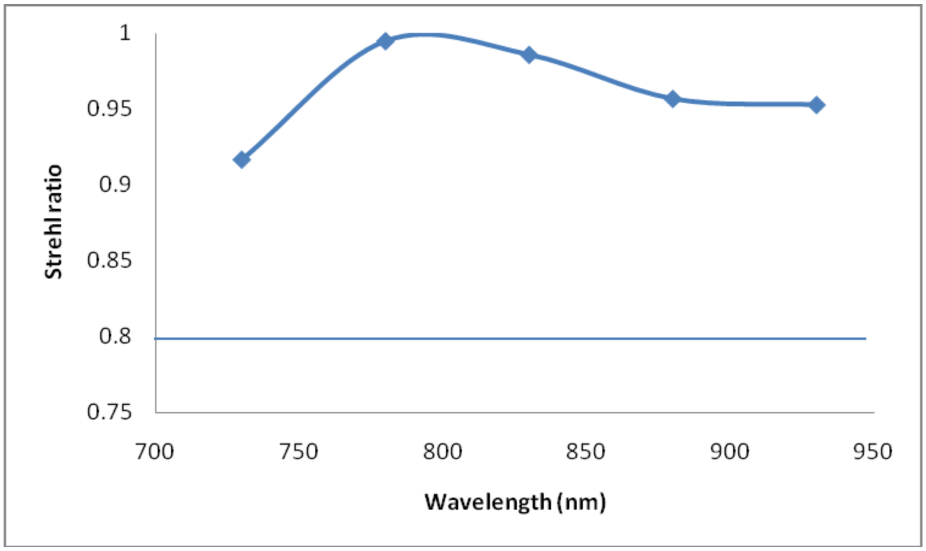

Figure 4.3: Variation of the Strehl ratio with wavelengths.

4.3 Spectrometer imaging performance comparison

Refractive optics and reflective optics spectrometers were designed using cylindrical optics, which can be utilized for line-field OCT imaging. In the refractive optics spectrometer, a plano-convex cylindrical lens and an achromatic lens were used while a cylindrical mirror was used in the reflective optics spectrometer configuration. The beam path of the designed spectrometer in the x-z plane and in the y-z plane is shown in Figure 4.4. The dispersed spectrum on the CCD is shown in Figure 4.4 (c). The incident beam from the fold mirror to the grating is dispersed corresponding to the wavelengths. The dispersed beam is then focused onto the detector by using cylindrical focusing optics. The array detector of 1920 pixels in the spectral dispersed direction with each pixel having the size of 5μm was predicted for the spectrometer design. The number of pixels in the line direction depends on the size of the incident beam used in the spectrometer design. In the present work, 2, 3 and 4mm size beams were used to evaluate the imaging performance. 400, 600 and 800 pixels are required to cover 2, 3 and 4mm beams respectively with a pixel size of 5µm. Therefore, to cover the 200nm spectral band with 2, 3 and 4mm beams 1920 by 400, 1920 by 600 and 1920 by 800 pixels resolution detectors are required.

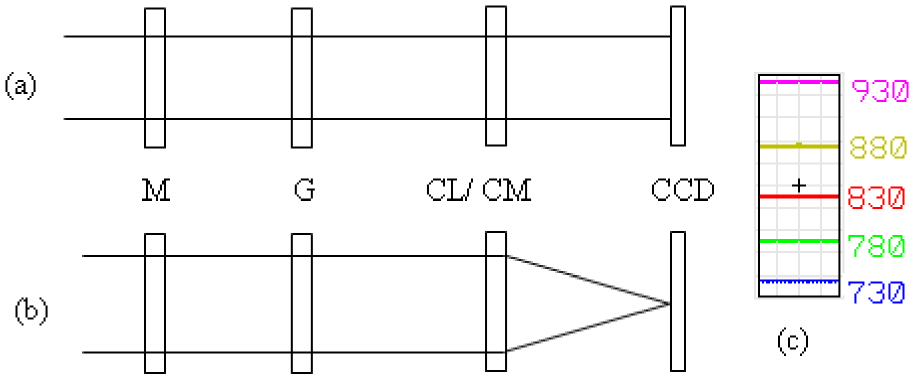

Figure 4.4: Beam paths of the spectrometer on (a) the x-z plane, (b) the y-z plane and (c) CCD plane. (M-mirror, G-grating, CL-cylindrical lens, CM-cylindrical mirror, and CCD-detector).

4.3.1 Plano-convex cylindrical lens spectrometer

In the refractive optics spectrometer, the light beam first incidents onto the fold mirror and is then reflected at an angle of 30° by the fold mirror towards the reflective grating. The broadband spectrum is then dispersed into its component wavelengths from the reflective grating. Angle between the incident and the reflected beam from the grating is 50° with respect to the center wavelength. The spectrum dispersed from the reflective grating is focused onto the detector array using a plano-convex cylindrical lens, as shown in Figure 4.5. A 25mm effective focal length cylindrical lens with BK7 glass was used in this design. Aperture size of the plano-convex cylindrical lens was 20mm by 20mm (PCKX045, Cylindrical optics company Ltd.).

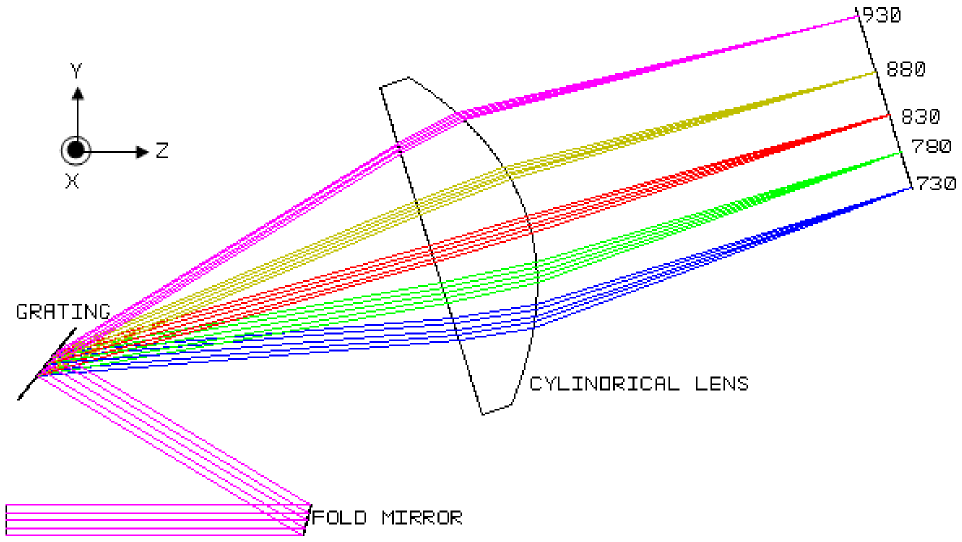

Figure 4.5: Optical layout of the spectrometer with a plano-convex cylindrical lens.

4.3.2 Achromatic cylindrical lens spectrometer

Refractive optics spectrometer using an achromatic cylindrical lens was also designed for performance comparison. Optical design of the spectrometer with the achromatic cylindrical lens is shown in Figure 4.6. Focal length of the achromatic lens is 25mm. Radius of curvatures of the achromatic lens is 18mm, 10mm and 48mm for the first, second and third surface respectively. BK7 and SF5 glasses were used in the achromatic lens combination. Aperture size of the achromatic lens is 20mm by 20mm. During the spectrometer design, achromatic cylindrical lens was available from two vendors. The aperture size for 25mm focal length was found to be 12.5mm diameter (Edmund optics - NT68-160) and 12.7mm by 12.7mm (Cylindrical optics company Ltd, ACL011). Therefore, custom-made lens design and fabrication are required for this spectrometer configuration to cover the 200nm spectral bandwidth.

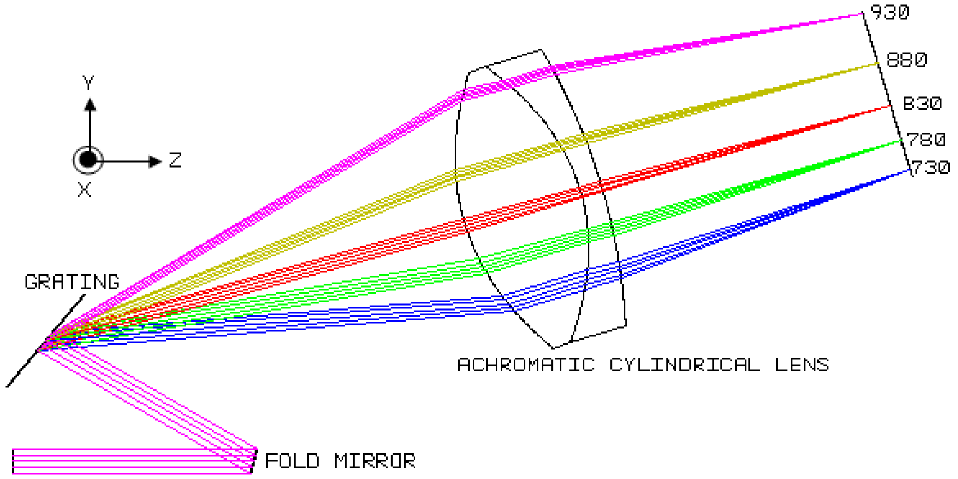

Figure 4.6: Optical layout of the spectrometer with an achromatic cylindrical lens.

4.3.3 Reflective optics spectrometer

Reflective optics focused spectrometer was designed to compare the performance of the refractive and reflective spectrometer. Similar optical arrangement has been employed in the reflective optics spectrometer except a cylindrical mirror was used instead of the cylindrical lens to focus the beam onto the detector array, as shown in Figure 4.7. A modified optical model presented here for performance comparison. Radius of curvature of the cylindrical mirror is 51.7mm. This cylindrical mirror can be fabricated by applying reflection coating on a plano-concave cylindrical lens, for example, LK1743L1, Throlabs. The cost of the cylindrical mirror would be cheaper compared to the custom-made achromatic cylindrical lens.

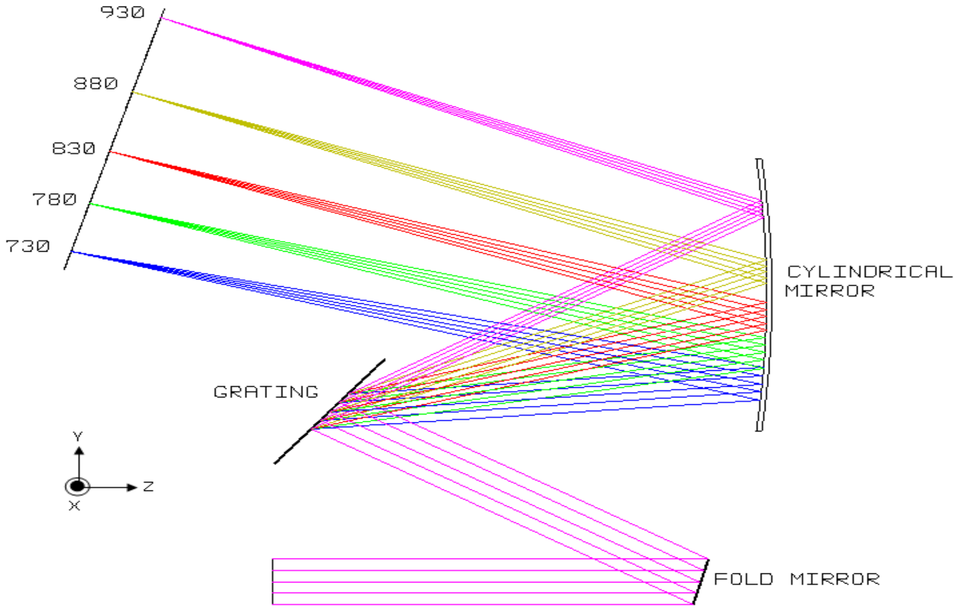

Figure 4.7: Optical layout of the reflective optics spectrometer.

4.3.4 Results and discussion

In line-field OCT, the lateral resolution is defined in the focusing as well as in the line direction. Later resolution in the focusing direction is same as the flying spot scanning, which is determined by NA of the objective lens. On the hand, lateral resolution in the line direction is determined by the Nyquist sampling theorem. According to the Nyquist sampling theorem larger beam in the spectrometer arm is required to achieve higher lateral resolution in line scan SD-OCT imaging [48]. In Chapter 2 and Chapter 3 [79, 90], a line-field scanning system was designed for 2mm scan range by using a cylindrical mirror for a high quality imaging. This spectrometer was designed to be integrated with our earlier designed line-focused scanning for high speed SD-OCT imaging. Incident beam sizes of 2, 3 and 4mm were used in the designed spectrometers to evaluate the effect of beam size on the imaging performance. Therefore, the transverse resolution in the line direction is 10µm, 4.44µm and 2.25µm respectively for 2mm, 3mm and 4mm beam. Imaging quality comparison of the designed spectrometers is presented in the following sections.

4.3.4.1 Chromatic focal shift

A higher spectral band light source is used for an ultrahigh axial resolution OCT imaging system. Refractive optics is sensitive to the spectral width of the light source. Due to the chromatic focal shift, effective focal length (EFL) of the refractive optics varies with the wavelengths. Chromatic focal shift for 4mm beam of the three spectrometer configurations with 25mm EFL is shown in Figure 4.8. Chromatic focal shift for the plano-convex and achromatic cylindrical spectrometer are 186µm and 130µm respectively. Due to its insensitivity to the spectral bandwidth, cylindrical mirror configuration maintains zero chromatic focal shifts. Consequently the reflective optics spectrometer maintains higher imaging quality discussed in the following sub-section.

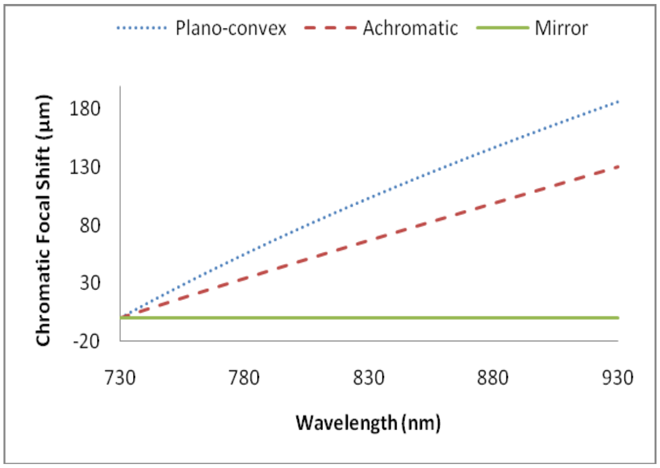

Figure 4.8: Chromatic focal shift for 4mm.

4.3.4.2 Strehl ratio comparison

The Strehl ratio (SR) is one of the parameters is used to evaluate the performance of the optical system. The SR is the ratio between the aberrated spread function to the aberration free spread function. SR from the ZEMAX model was recorded to compare the performance of the refractive optics and the reflective optics spectrometers. SR was recorded for the three beam sizes within 200nm spectral range with a centre wavelength of 830nm. Comparison of the SR for the beam size of 2mm, 3mm and 4mm are shown in Figures 4.9(a), (b), and (c), respectively.

For 2mm beam size, similar performance was achieved from the both spectrometer configurations except small drops towards the edges. However, with the larger beam size the SR significantly drops towards the edges for the refractive optics configurations, as shown in Figure 4.9(b) and Figure 4.9(c). For example, in the case of plano-convex cylindrical lens with a 4mm beam the SR drops from 0.88 to 0.45 for the wavelength range of 830nm to 730nm. For the wavelength range 830nm to 930nm the SR drops from 0.88 to 0.19. Due to the chromatic aberration, the broadband spectrum focuses in a different focal plane. In the refractive optics spectrometer configuration, the dispersed wavelengths either focused before reaching the CCD detector plane or reached the CCD plane before focusing, as shown in Figure 4.10. As a result the imaging quality significantly reduces at the lower end of the spectral band.

To enhance imaging performance, special designed achromatic lenses are used in SD-OCT. Model results shows that in case of the achromatic cylindrical lens the SR drop from 0.99 to 0.58 and from 0.99 to 0.482 respectively for the wavelength range of 830nm to 730nm and 830nm to 930nm. Reason of this variation is the residual chromatic aberration as shown in Figure 4.8, and the geometric configuration of the spectrometer such as the angle between the incident and the reflected beams, distance between the grating and the cylindrical mirror, and the ROC of the cylindrical mirror.

On the other hand, reflective optics focusing is not sensitive to the spectral bandwidth of the light source. Therefore, reflective optics focused the whole wavelengths' band in the same focal plane. Imaging quality of the refractive optics spectrometer depends on the geometric configuration of the spectrometer. With an optimized geometrical configuration, a broad spectral band can be focused on the CCD detector plane which will improve the imaging performance, as can be seen in Figure 4.7. Hence, chromatic aberration can be eliminated by using reflective optics instead of the refractive optics focusing. The designed cylindrical mirror focused spectrometer configuration maintains an SR of more than 0.92 throughout the 200nm spectral range for a 4mm beam size. Therefore, reflective optics spectrometer design maintains the SR above the Marechal criterion [85], which is required for a good quality optical system.

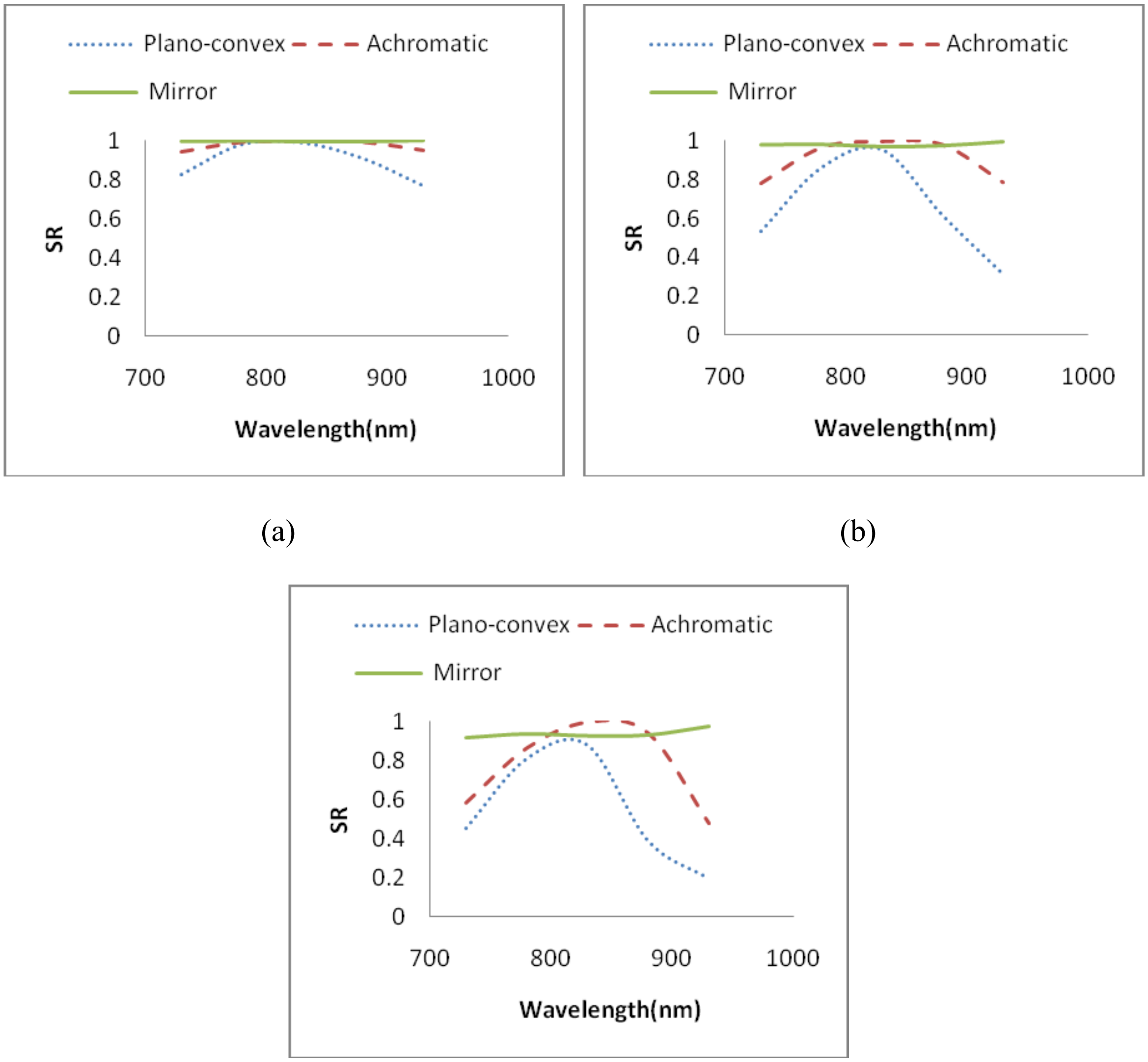

(a) (b)

(c)

Figure 4.9: Comparison of the SR with a (a) 2mm beam, (b) 3mm beam and (c) 4mm beam.

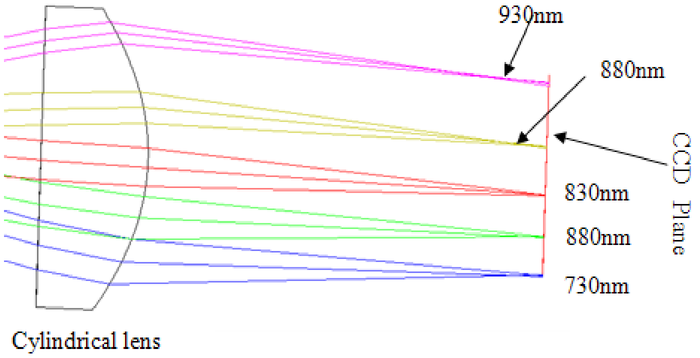

Figure 4.10: Wavelengths spread on CCD plane.

4.4 Analytical model of line-scan SD-OCT signal acquisition

In this section, a brief analytical model of the signal acquisition in SD-OCT for line scan is carried out. Hu. Z. et al. [36] reported analytical model of flying spot SD-OCT signal acquisition and studied spectrometer design parameters. In SD-OCT, the interference signal from the reference mirror and from all reflective surfaces within the sample depth range is recorded in a single shot. In the flying spot SD-OCT, a line scan camera is used in the spectrometer to record the interference signal. Every individual wavelength focused to a point spread function (PSF) is centered at specific coordinate of the CCD array. Hu. Z. et al. [36], used normalized 2D Gaussian distribution Equation (4.1) to derive a general expression for flying spot SD-OCT signal recorded by j^{th} pixel of the CCD as shown in Equation (4.2).

$$h(x, y, x_i) = \frac{4\ln 2}{\pi a^2} e^{-\left(\frac{4\ln 2}{a^2}\right)\left((x-x_i)^2+y^2\right)} \tag{4.1}$$

$$I(x_j) = \frac{1}{4} Erf\left(\frac{\Delta N_y \sqrt{\ln 2}}{a}\right) \int_0^{\infty} \left(\left(\begin{array}{l} Erf\left(\frac{(\Delta N_x - 2k_i + 2x_j)\sqrt{\ln 2}}{a}\right) + \\ Erf\left(\frac{(\Delta N_x + 2k_i - 2x_j)\sqrt{\ln 2}}{a}\right) \end{array} \right) \times \\ \left(R_r(k) + R_s(k) + 2\sqrt{R_r(k) R_s(K)} \cos(k\Delta l) \right) \right) dk \qquad (4.2)$$

The signal acquisition model presented here was modified from Hu. Z. et al. [36] model for line-scan SD-OCT. In line-scan SD-OCT, such as the one developed in this work, an area scan camera is required to record the spectrally encoded interference data. The analytical model of the proposed line scan SD-OCT system presented herein is established based on the following assumptions:

1). each single wavelength is focused as a line at particular coordinate of the CCD array,

2). the line intensity distribution is a two-dimensional Gaussian distribution of the line spread function (LSF),

3). intensity of each pixel contains contributions from all the wavelengths of the broadband spectrum, and

4). intensity of each pixel is depends on the spectrometer line profile, and the size and shape of the pixel. The CCD array resolution is N_x by N_y with a pixel size of ΔN_x by ΔN_y.

5). SD-OCT signal consists of DC term, cross-correlation term, and the auto-correlation, as discussed in Section 1.6.5. Cross-correlation term contains the axial profile of the OCT image. For simplicity only the cross-correlation term was used to build this analytical model.

The schematic of the intensity distributions are shown in Figure 4.11. The spectrometer disperses the wavelength spectrum which covers the x-axis of the CCD array while the focused line covers the y-axis of the CCD array.

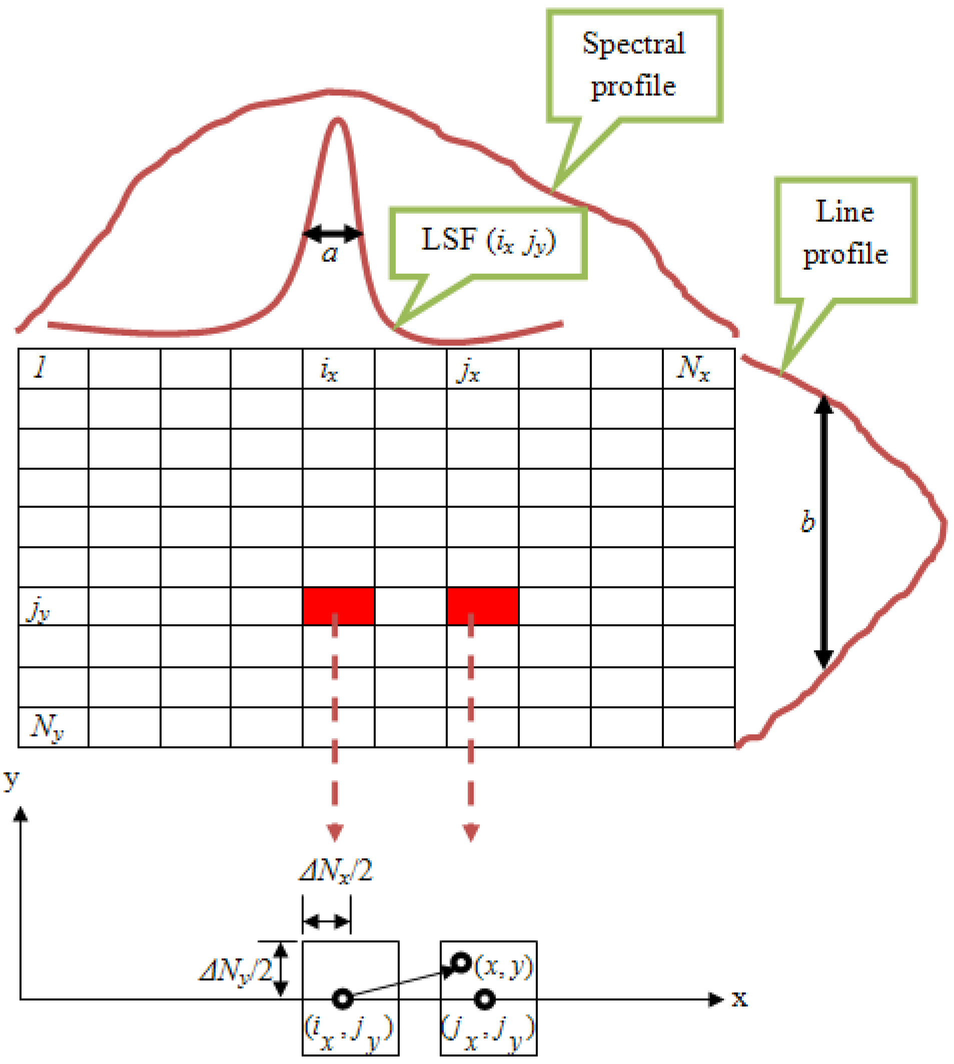

Figure 4.11: Spectral intensity and line intensity distribution on the CCD detector array.

Considering the above assumptions, three-dimensional (3D) model of the signal intensity $I(x_{j_x} y_{j_y})$ for the *(jx, jy)th* pixel of the array positioned at coordinate $(x_{j_x} y_{j_y})$ can be expressed by [36]:

$$I(x_{j_x}, y_{j_y}) = \int_0^{\alpha} \int_0^{A} G(x, y, k_{(i_x, j_y)})(2\sqrt{R_r R_s} \cos(k_{(i_x, j_y)} \Delta l)) dA dk_{(i_x, j_y)} \tag{4.3}$$

Here, R_r and R_s are the power spectral density from the reference arm and from the sample arm respectively, k is the wave number, and Δl is the path length difference between the sample arm and reference arm. The wave number k is defined by $k=2\pi/\lambda$. $G(x, y, k_{(i_x, j_y)})$ is a normalized 2D Gaussian of LSF. A is the area of pixel (j_x, j_y) and the differential variable is described by $dA=dxdy$. 2D Gaussian distribution of a LSF can be expressed by [36, 103]:

$$G(x, y) = \frac{2\sqrt{\ln 2}}{\sqrt{\pi} a} e^{-\left(\frac{4\ln 2}{a^2}\right)x^2} \times \frac{2\sqrt{\ln 2}}{\sqrt{\pi} b} e^{-\left(\frac{4\ln 2}{b^2}\right)y^2} \tag{4.4}$$

Here, the spread size *'a'* is the full-width-at-half-maximum (FWHM) in the focusing direction and *'b'* is the FWHM in the line direction of the LSF. The contribution of wave number $k_{(i_x, j_y)}$ at (x, y) in pixel (j_x j_y) can be expressed by a normalized 2D Gaussian distribution of Equation (4.4) :

$$G(x, y, k_{(i_x, j_y)}) = \frac{2\sqrt{\ln 2}}{\sqrt{\pi} a} e^{-\left(\frac{4\ln 2}{a^2}\right)\left(x - k_{(i_x, j_y)}\right)^2} \times \frac{2\sqrt{\ln 2}}{\sqrt{\pi} b} e^{-\left(\frac{4\ln 2}{b^2}\right)y^2} \tag{4.5}$$

The total intensity of pixel *(j$_x$, j$_y$)* by $k_{(i_x,j_y)}$ is the integral of the distribution function $G(x,y)$ over the area of pixel *(j$_x$,j$_y$)*, which can be expressed by:

$$\int_0^A G\left(x,y,k_{(i_x,j_y)}\right)dA = \int_{\left(x_{j_x}-\Delta N_x/2\right)}^{\left(x_{j_x}+\Delta N_x/2\right)} \int_{\left(y_{j_x}-\Delta N_y/2\right)}^{\left(y_{j_x}+\Delta N_y/2\right)} \left(\frac{2\sqrt{\ln 2}}{\sqrt{\pi a}} e^{-\left(\frac{4\ln 2}{a^2}\right)\left(x-k_{(i_x,j_y)}\right)^2} \times \frac{2\sqrt{\ln 2}}{\sqrt{\pi b}} e^{-\left(\frac{4\ln 2}{b^2}\right)y^2} \right) dydx$$

$$\int_0^A G\left(x,y,k_{(i_x,j_y)}\right)dA = \left(\begin{array}{c} \left(\displaystyle\int_{\left(x_{j_x}-\Delta N_x/2\right)}^{\left(x_{j_x}+\Delta N_x/2\right)} \left(\frac{4\ln 2}{\pi ab} e^{-\left(\frac{4\ln 2}{a^2}\right)\left(\left(x-k_{(i_x,j_y)}\right)^2\right)} \right) dx \right) \times \\ \left(\displaystyle\int_{\left(y_{j_x}-\Delta N_y/2\right)}^{\left(y_{j_x}+\Delta N_y/2\right)} \left(e^{-\left(\frac{4\ln 2}{b^2}\right)y^2} \right) dy \right) \end{array} \right) \quad (4.6)$$

For simplicity Equation (4.4) was solved by using integral by parts method.

<u>Solution for first part of the Equation (4.4):</u>

Following equations were used to solve the first part of the Equation (4.6).

$$\int \frac{1}{\sigma\sqrt{2\pi}} e^{-\frac{(x-\mu)^2}{2\sigma^2}} dx = -\frac{1}{2}\left(Erf \frac{-x+\mu}{\sigma\sqrt{2}} \right) \quad (4.7)$$

In the first part of the Equation (4.6), $\frac{1}{2\sigma^2} = \left(\frac{4\ln 2}{a^2}\right)$, $\frac{1}{\sigma\sqrt{2\pi}} = \frac{2\sqrt{\ln 2}}{b\sqrt{\pi}} . \frac{2\sqrt{2\ln 2}}{a\sqrt{2\pi}} = \frac{4\ln 2}{\pi ab}$

$$Erf(-x) = -Erf(x) \quad (4.8)$$

$$\int_{\left(x_{j_x}-\Delta N_x/2\right)}^{\left(x_{j_x}+\Delta N_x/2\right)} \left(\frac{4\ln 2}{\pi ab} e^{-\left(\frac{4\ln 2}{a^2}\right)\left(x-k_{(i_x,j_y)}\right)^2} \right) dx = \left(\frac{2\sqrt{\ln 2}}{b\sqrt{\pi}} \right) \int_{\left(x_{j_x}-\Delta N_x/2\right)}^{\left(x_{j_x}+\Delta N_x/2\right)} \left(\frac{2\sqrt{2\ln 2}}{a\sqrt{2\pi}} e^{-\left(\frac{4\ln 2}{a^2}\right)\left(x-k_{(i_x,j_y)}\right)^2} \right) dx$$

$$= \left(\frac{2\sqrt{\ln 2}}{b\sqrt{\pi}} \right) \left[-\frac{1}{2} Erf \frac{k_{(i_x,j_y)}-x}{\frac{a\sqrt{2}}{2\sqrt{2\ln 2}}} \right]_{\left(x_{j_x}-\Delta N_x/2\right)}^{\left(x_{j_x}+\Delta N_x/2\right)}$$

$$= \left(\frac{2\sqrt{\ln 2}}{b\sqrt{\pi}} \right) \left(-\frac{1}{2} \left(Erf\left(\left(k_{(i_x,j_y)} - x_{j_x} - \Delta N_x/2\right) \frac{2\sqrt{\ln 2}}{a} \right) - Erf\left(\left(k_{(i_x,j_y)} - x_{j_x} + \Delta N_x/2\right) \frac{2\sqrt{\ln 2}}{a} \right) \right) \right)$$

$$= \left(\frac{\sqrt{\ln 2}}{b\sqrt{\pi}} \right) \left(Erf\left(\left(\Delta N_x - 2k_{(i_x,j_y)} + 2x_{j_x}\right) \frac{\sqrt{\ln 2}}{a} \right) + Erf\left(\left(\Delta N_x + 2k_{(i_x,j_y)} - 2x_{j_x}\right) \frac{\sqrt{\ln 2}}{a} \right) \right) \quad (4.9)$$

Here, $Erf(-x) = \frac{2}{\sqrt{\pi}} \int_0^x e^{-t^2} dt$ is the error function.

Solution for second part of the Equation (4.6):

Following equation was used to solve the second part of the Equation (4.6).

$$\int e^{-\xi x^2} dx = \frac{\sqrt{\pi}}{2\sqrt{\xi}} Erf(x\sqrt{\xi}) \quad (4.10)$$

In the second part of the Equation (4.6), $\xi = \left(\frac{4\ln 2}{b^2} \right)$

$$\int_{\left(y_{j_x}-\Delta N_y/2\right)}^{\left(y_{j_x}+\Delta N_y/2\right)}\left(e^{-\left(\frac{4\ln 2}{b^2}\right)y^2}\right)dy=\frac{\sqrt{\pi}}{2\sqrt{\frac{4\ln 2}{b^2}}}\left[Erf\left(y\frac{2\sqrt{\ln 2}}{b}\right)\right]_{\left(y_{j_x}-\Delta N_y/2\right)}^{\left(y_{j_x}+\Delta N_y/2\right)}$$

$$=\frac{b\sqrt{\pi}}{4\sqrt{\ln 2}}\left(Erf\left(\left(y_{j_x}+\Delta N_y/2\right)\frac{2\sqrt{\ln 2}}{b}\right)-Erf\left(\left(y_{j_x}-\Delta N_y/2\right)\frac{2\sqrt{\ln 2}}{b}\right)\right)$$

$$=\frac{b\sqrt{\pi}}{4\sqrt{\ln 2}}\left(Erf\left(\left(\Delta N_y+2y_{j_x}\right)\frac{\sqrt{\ln 2}}{b}\right)+Erf\left(\left(\Delta N_y-2y_{j_x}\right)\frac{\sqrt{\ln 2}}{b}\right)\right) \tag{4.11}$$

Now, the intensity distribution can be rewritten from Equation (4.6) as:

$$\int_0^A G\left(x,y,k_{(i_x,j_y)}\right)dA$$
$$=\left(\frac{\sqrt{\ln 2}}{b\sqrt{\pi}}\right)\left(Erf\left(\left(\Delta N_x-2k_{(i_x,j_y)}+2x_{j_x}\right)\frac{\sqrt{\ln 2}}{a}\right)+Erf\left(\left(\Delta N_x+2k_{(i_x,j_y)}-2x_{j_x}\right)\frac{\sqrt{\ln 2}}{a}\right)\right)\times$$
$$\left(\frac{b\sqrt{\pi}}{4\sqrt{\ln 2}}\right)\left(Erf\left(\left(\Delta N_y+2y_{j_x}\right)\frac{\sqrt{\ln 2}}{b}\right)+Erf\left(\left(\Delta N_y-2y_{j_x}\right)\frac{\sqrt{\ln 2}}{b}\right)\right)$$

$$\int_0^A G\left(x,y,k_{(i_x,j_y)}\right)dA=\frac{1}{4}\left(\begin{array}{l}\left(\begin{array}{l}Erf\left(\left(\Delta N_x-2k_{(i_x,j_y)}+2x_{j_x}\right)\frac{\sqrt{\ln 2}}{a}\right)+\\ Erf\left(\left(\Delta N_x+2k_{(i_x,j_y)}-2x_{j_x}\right)\frac{\sqrt{\ln 2}}{a}\right)\end{array}\right)\times\\ \left(Erf\left(\left(\Delta N_y+2y_{j_x}\right)\frac{\sqrt{\ln 2}}{b}\right)+Erf\left(\left(\Delta N_y-2y_{j_x}\right)\frac{\sqrt{\ln 2}}{b}\right)\right)\end{array}\right) \tag{4.12}$$

By substituting $\int_0^A G\left(x, y, k_{(i_x,j_y)}\right)dA$ in Equation (4.3) the interference signal can be rewritten as:

$$
\begin{aligned}
I(x_{j_x}, y_{j_y}) = \frac{1}{4}\left(Erf\left(\left(\Delta N_y + 2y_{j_x}\right)\frac{\sqrt{\ln 2}}{b}\right) + Erf\left(\left(\Delta N_y - 2y_{j_x}\right)\frac{\sqrt{\ln 2}}{b}\right)\right) \times \\
\int_0^\infty \left(\left(\begin{array}{l} Erf\left(\left(\Delta N_x - 2k_{(i_x,j_y)} + 2x_{j_x}\right)\frac{\sqrt{\ln 2}}{a}\right) + \\ Erf\left(\left(\Delta N_x + 2k_{(i_x,j_y)} - 2x_{j_x}\right)\frac{\sqrt{\ln 2}}{a}\right) \end{array} \right) \times \left(2\sqrt{R_r R_s}\cos(k_{(i_x,j_y)}\Delta l)\right) \right) dk_{(i_x,j_y)}
\end{aligned}
\tag{4.13}
$$

This equation is verified by applying *a* = *b* which makes the line to a spot and $y_{j_x} = 0$ so that the area scan camera becomes a line scan camera. If these two changes are carried out, the Equation (4.13) will be same of the Equation (4.2) derived by Hu. Z. et al. [36] for flying spot scanning. The Equation (4.13) represents the optical resolution of the spectrometer based on the contribution of the finite pixel size as well as the LSF. Here, the pixel height ΔN_y and spread *'b'* affect only the total intensity, while the pixel width ΔN_x and the line spread '*a'* affect the interference signal.

A-scan profile can be obtained by performing Fourier Transformation (FT) of the Equation (4.13). Since the intensity distribution in the line direction has no influence on the interference signal, the depth dependent signal fall-off of the line-scan SD-OCT will be similar to that of the flying spot SD-OCT. Examples of A-scan profile generation and depth dependent sensitivity fall-off is presented in Appendix A. The depth dependent signal fall-off can be expressed from the FT of the Equation (4.13) [36]:

$$S_{fall-off}(z) = (\Delta N_x R)\exp\left(-\frac{a^2R^2z^2}{4\ln 2}\right)\left(\frac{\sin(\Delta N_x Rz)}{\Delta N_x Rz}\right) \tag{4.14}$$

Here, z is the depth position and $R = \frac{\Delta k}{\Delta N_x}$ is the reciprocal linear dispersion, where Δk is the segment of the wave number covered by the CCD pixel width ΔN_x. The reciprocal linear dispersion can be expressed by $R = \frac{\Delta k}{\Delta N_x} = \frac{d.\cos\beta}{mf}$ [104]. Where, *d* is the groove spacing of the grating, *β* is the diffracted angle, *m* is the order of diffraction, and *f* is the effective focal length of the spectrometer focusing optics.

Therefore, depth dependent signal fall-off depends on the imaging quality of the spectrometer and determined by the line spread function *'a'* for a designed spectrometer. The line spread function *'a'* is driven by the spectrometer system parameters. These system parameters include the CCD pixel size (ΔN_x), grating grove spacing (*d)*, the diffracted angle (*β)*, the order of diffraction (*m)*, and the effective focal length of the spectrometer focusing optics *(f)*.

Optical design of refractive optics and reflective optics spectrometers are presented in Section 4.3. It can be seen from Figure 4.9(c) that for a 4mm beam the SR varies significantly with respect to the wavelength in the case of refractive optics based spectrometers, while the SR remains same for reflective optics spectrometer. Since SR is defined by the size and shape of the spread function, the loss of SR with respect to wavelength signifies a change in the spread function with wavelength thereby affecting the sensitivity fall-off.

As a consequence, the LSF ‘*a’* changes its size and shape towards the end of the spectral range. Hence, the LSF of a single wavelength may not fit into a pixel area and its intensity distribution could potentially reach in the surrounding pixels. Figure 4.12 shows the LSFs of the plano-convex cylindrical lens focused spectrometer and Figure 4.13 shows the LSFs of the achromatic lens focused spectrometer at different wavelengths. On the other hand, the reflective optics-based spectrometer maintains a consistent SR and therefore consistent size and shape of LSF throughout the 200nm spectral bands, as shown in Figure 4.14. It can be seen from the figures that the LSF ‘a’ is consistent within the spectral range in the case of reflective optics spectrometer, thereby providing better sensitivity in comparison to refractive optics spectrometers.

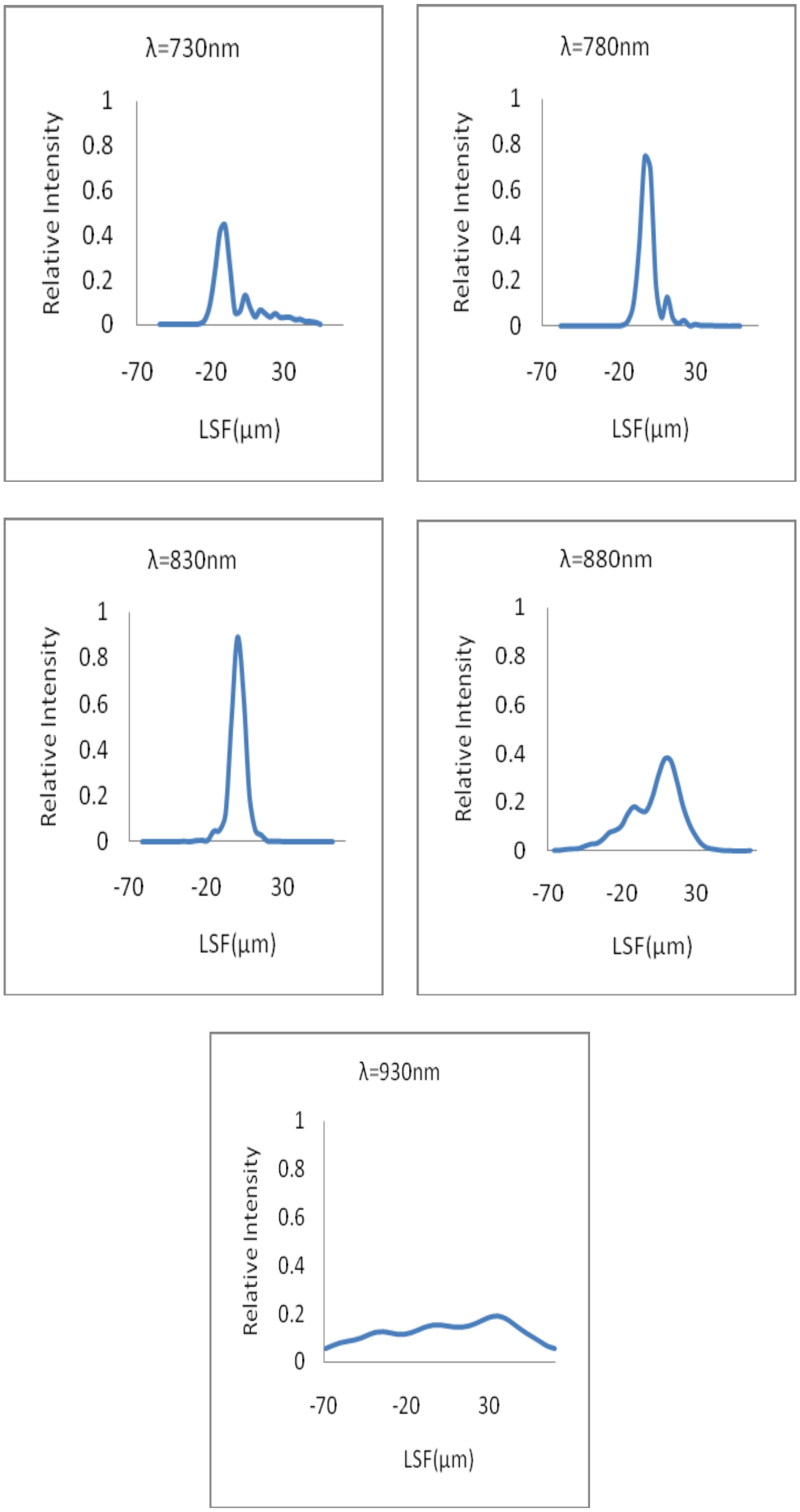

Figure 4.12: LSFs of the plano-convex cylindrical lens based spectrometer

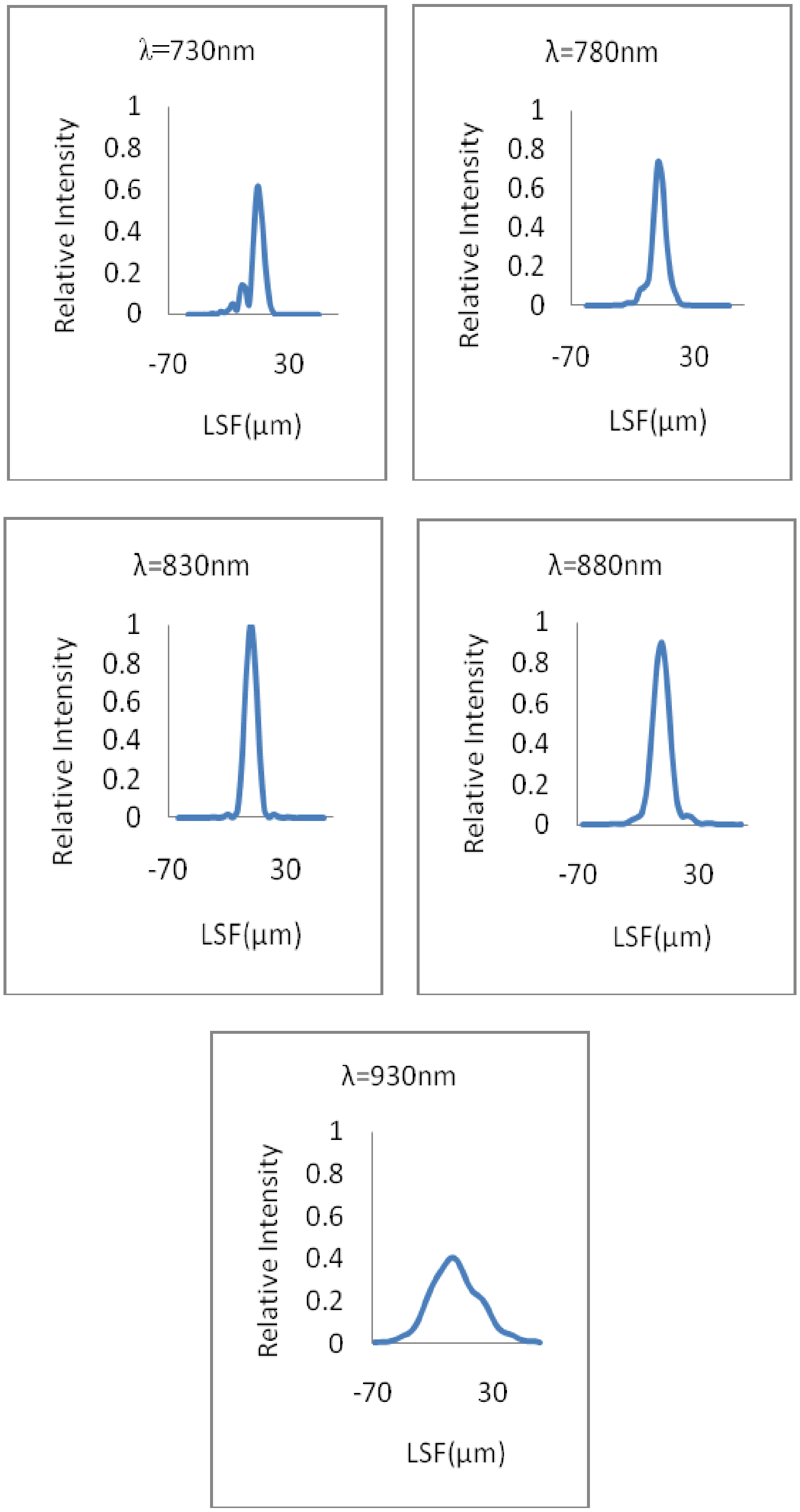

Figure 4.13: LSFs of the achromatic cylindrical lens based spectrometer

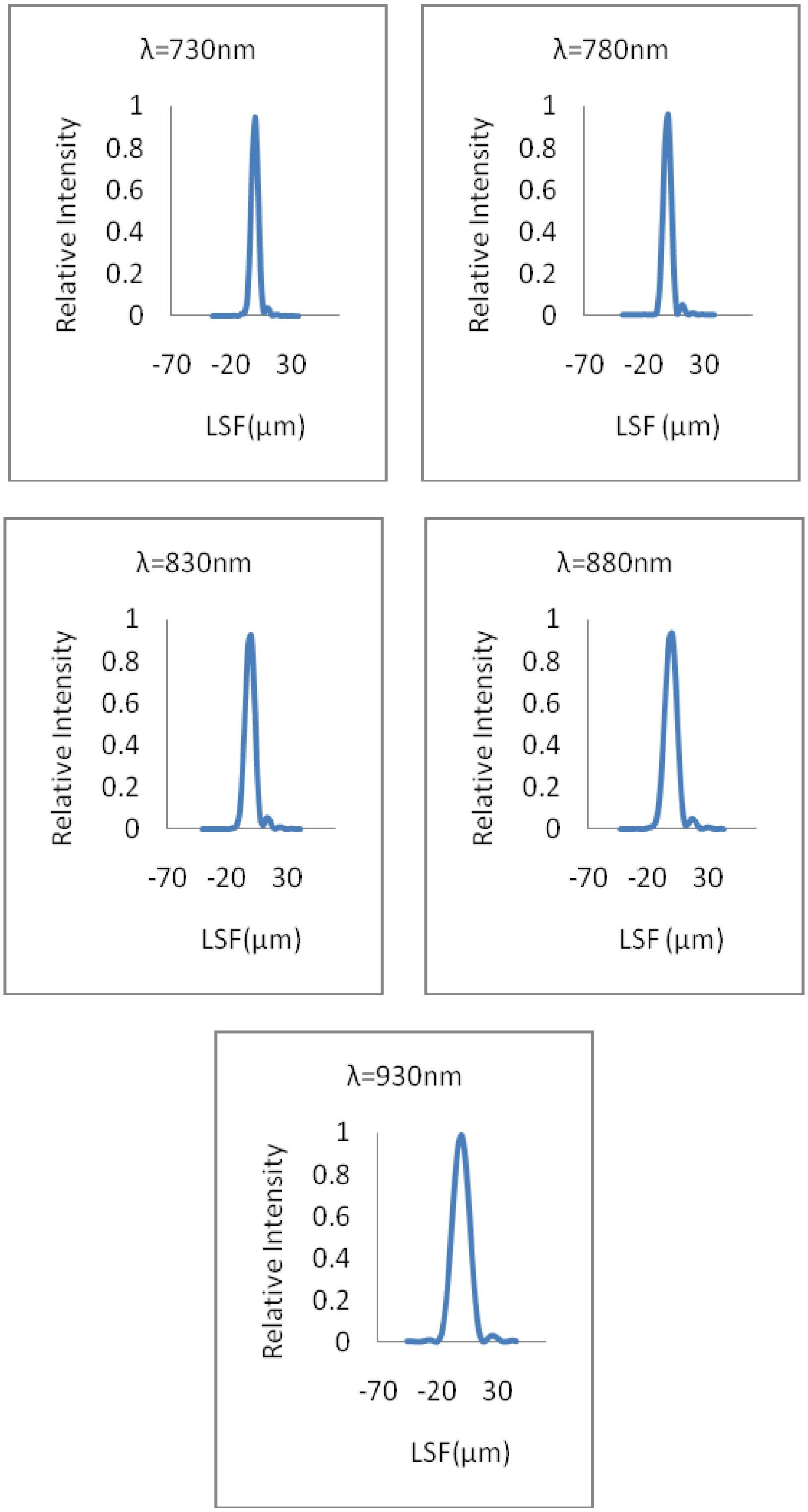

Figure 4.14: LSFs of the cylindrical mirror based spectrometer

4.5 Conclusions

Optical modeling of a reflective optics spectrometer for light source with a spectral bandwidth of 200nm for a high quality line-field SD-OCT imaging is presented in this chapter. The imaging performance was compared with the refractive optics spectrometers. A plano-convex cylindrical lens, an achromatic cylindrical lens and a cylindrical mirror was used as a focusing element in the designed spectrometers. The spectrometers cover the spectral range of 730nm to 930nm. Performances of the designed spectrometers were assessed by recording the SR and chromatic focal shifts from the ZEMAX optical model. Chromatic focal shift for the plano-convex and the achromatic cylindrical spectrometer is 186µm and 130µm respectively while the cylindrical mirror maintains zero chromatic focal shifts due to its insensitivity to the broad spectral band. Model results show that for a larger beam size the performance drops significantly in the case of plano-convex cylindrical lens focused spectrometer. For example, in case of the 4mm size beam, the SR drops by 48% from 830nm to 730nm and by 78% from 830nm to 930nm wavelength range. In case of the achromatic cylindrical lens spectrometer, the SR drops by 41% from 830nm to 730nm and by 51% from 830nm to 930nm wavelength range. Whereas reflective optics focused spectrometer maintains an SR more than 0.9 for the wavelength range of 730nm to 930nm regardless of the beam sizes considered. Therefore, reflective optics spectrometer provides better imaging performance with a higher resolution. In addition, an analytical model has been developed for data processing with the proposed line-scan SD-OCT and shows that the reflective optics based spectrometer based SD-OCT systems provide better sensitivity throughout the 200nm spectral band width.

Chapter 5: Experimental validation of reflective optics line scanning system

Optical design of the vital sub-modules of OCT imaging is presented in Chapter 2 to Chapter 4. From the performance analysis it is proved that the reflective optics based scanning system provides better imaging quality compared to the refractive optics based scanning system. Reflective spectrometer also provides better performance compared to the refractive optics spectrometer. A 200nm spectral band width light source was used in the scanning system and in the spectrometer design for a high axial resolution.

Modified optical model and experimental validation are presented in this chapter covering objective '1d' of the Objective and scope of the thesis in Section 1.11. This chapter is based on the manuscript submitted to the Journal of Optics (Manuscript ID - JOPT/400149/PAP/148632) [93]. A 53nm Spectral bandwidth light source with a centre wavelength of 843nm was used for experimental validation of the scanning system. The spectral range of this light source is from 800nm to 880nm with a center wavelength of 843nm. Though the axial resolution is reduced due to the reduction of the spectral bandwidth, this will not have any influence on the imaging quality as mirror focusing is insensitive to the spectral bandwidth.

5.1 Introduction

Optical coherence tomography (OCT) is a non-invasive optical imaging technology that can generate two-dimensional (2D) and three-dimensional (3D) images with micrometer scale resolution. In OCT, axial resolution is determined by the spectral bandwidth of the light source whereas the lateral resolution is determined by using the system optics [30, 31, 105]. In addition to high resolution, a higher imaging speed is also essential for clinical applications of the OCT imaging. After implementation of the Fourier domain acquisition in OCT, the imaging speed and sensitivity improve significantly [73, 106]. However, most of the OCT systems utilize point based scanning in which 2D mechanical scanning is required to acquire a 2D tomogram, thereby reducing the imaging speeds. Alternatively, parallel detection, such as line-scan (LS) OCT [47, 48, 52, 53, 86] and full-field has been developed for high speed imaging. Full-field OCT (FF-OCT) is not suitable for endoscopic OCT imaging [87]. A line-scan OCT provides parallel spatial detection, thereby increasing the speed and constancy while reducing the complexity compared to a flying-spot scanning system.

In OCT imaging, the axial and transverse resolutions are decoupled. In line-field OCT, the light beam focuses in one direction by using cylindrical optics, and in the other direction the beam size remains the same as the incident beam. Hence, transverse resolution in a line-field OCT is determined independently in the focusing and in the line directions [47, 48]. Transverse resolution in the focusing direction of a line-field OCT is same as the transverse resolution of the flying spot OCT, which is determined by the scanner arms numerical aperture and is expressed by $\Delta y = 1.22\frac{\lambda_c f}{l_s}$, where, l_s is the line length, λ_c, is the center wavelength of the light source, and *f* is the effective focal length of the scanner arm focusing optics. Thus, a higher transverse resolution can be achieved either by using a larger size beam (l_s) or a shorter focal length (*f*). On the other hand, in the case of endoscopic OCT imaging, the probe size prevents the use of a larger beam. Hence, the only way to increase the transverse resolution is by using a shorter focal length. The transverse resolution in the line direction is determined according to the Nyquist theorem and the ratio $\left(M = \dfrac{l_s}{l_{CCD}}\right)$ of the sizes of the line-focused beams in the sample and the detector [48]. The line size in the detector $\left(l_{CCD} = \Delta N_x . N_x\right)$ can be rewritten in terms of number of pixels N_x of the detector occupied by the line length and ΔN_x is the pixel size. Hence, the transverse resolution in the line direction is expressed by $\Delta x = \dfrac{2}{\Delta N_x}\left(\dfrac{l_s}{N_x}\right)^2$. Therefore, the transverse resolution in the line direction depends on the line size on the sample and the detector resolution.

For high axial resolution OCT imaging, an ultrahigh broadband light source is required. For example, a 200nm spectral bandwidth [108] was used for the OCT imaging, which gives an axial resolution of 1.3μm in tissue. A conventional lens used in an OCT system focuses these wavelengths in different focal planes. Therefore, the axial resolution of the OCT imaging degrades due to chromatic aberration [39, 109]. Mirror focusing [77, 78] is an alternative that can be used to eliminate the chromatic aberration. Since the focal length of the mirror is insensitive to the spectral band of the light source, the axial resolution is not affected in OCT imaging with reflective optics.

A cylindrical mirror focused-line scanning system has been designed for high speed scanning with higher imaging quality. This scanning system can be utilized for OCT imaging applications with sub-micron axial resolution in general. With the ability to miniaturize the proposed scanning system, this can have an impact in endoscopic imaging applications in particular. In chapter 2 [79], and Chapter 3 [90], a mathematical model and an optical design of a line scanning system was reported for 200nm spectral bandwidth. The imaging performance was compared between a plano-convex cylindrical lens, an achromatic cylindrical lens, and a cylindrical mirror-based focused-line scanning system with 50.8mm, 25.4mm, and 12.7mm effective focal lengths [79]. The model results showed that the cylindrical mirror-focused scanning system provides better performance compared to both plano-convex system and better achromatic cylindrical lens scanning system. The model results also showed that cylindrical mirror scanning provides better performance when the beam is off-set from the center of the focusing optics.

In this chapter, a modified optical model and experimental validation of the line-scanning system is presented. The scanning system imaging quality was evaluated using ZEMAX optical design software. The results were verified experimentally. In the system that was developed, a light source with a center wavelength of 843nm and a spectral bandwidth at full-width-half-maximum (FWHM) of 53nm was used. Strehl ratio was used to evaluate the imaging quality of the scanning system over a 2mm scan range by using cylindrical mirrors with radius of curvatures (ROC) 51.7mm and 103.4mm.

5.2 Optical design of the scanning system

With the experimental constraints taken into consideration, the earlier optical design [79] was modified. In chapter 3 [79], the performance of the designed scanning system was evaluated for 25.4mm, 51.7mm and 103.4mm ROC mirrors with a 200nm spectral bandwidth. The distance between the mirrors and the angle between the incident beam and the reflected beam were optimized for higher imaging quality. The beam reflected from the scanning mirror is blocked by the CCD camera housing before reaching on the cylindrical mirror as shown in Figure 5.1. The beam is blocked by the camera housing because of a low ROC mirror with a smaller angle between the incident and reflected beams ‘ϕ’ and with a shorter distance ‘d’. The blocked beam is indicated by the dotted lines in Figure 5.1. For the experiments, the housing was removed from the camera, enabling the use of both 51.7mm and 103.7mm ROC mirrors with a distance ‘d’ of 35mm. The reduction of the distance ‘d’ below 35mm or lowering the ROC from 25.4mm is not possible with the CCD camera. The scanning system imaging performance was evaluated using free space optics. However, for a real endoscopic OCT system where the sample would be scanned instead of the CCD, beam blocking would have no influence. The designed scanning system can be used for real OCT imaging with a higher transverse resolution. The details of optical design of the scanning system can be found in chapter 2 [79], and Chapter 3 [90].

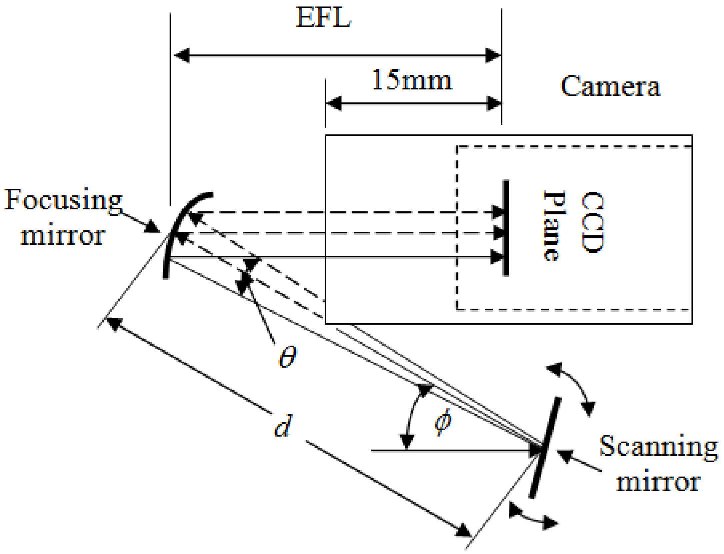

Figure 5.1: Beam blocking with CCD housing.

Cylindrical mirrors with ROCs of 51.7mm and 103.4mm were used in the optical design. The focal length (FL) of these mirrors is 25.85mm and 51.7mm respectively. In this design, an 843nm light source with a FWHM of 53nm was used. To avoid the beam clipping, the distance d was maintained at 35mm and the angle ϕ was maintained at 45° for both configurations. The incident light beam was collimated with a 10mm focal length achromatic collimating (AC) lens (Thorlabs, AC060-010-B) from a 0.14 NA object space beam. Subsequently, the beam was reflected by a scanning mirror (SM) and finally focused as a line onto the CCD plane by the cylindrical mirror (CM). The collimated output beam size was 2mm (at $1/e^2$). The optical layout of the scanning system is shown in Figure 5.2. Figure 5.3 shows the beam paths of the scanning system in the x-z plane and y-z plane. The collimated beam was focused as a line by using a cylindrical mirror in the Y-direction whereas in the X-direction it remained the same as the incident beam as shown in Figure 5.3(c). Scanning was carried out in the Y-direction by rotating the scanner mirror. Details of the scanning method and scanner position configuration can be found in our earlier works [79, 90].

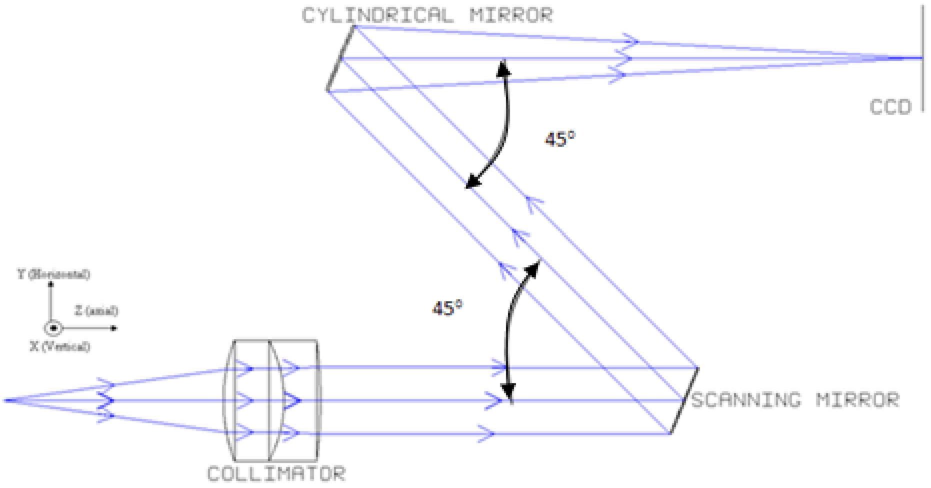

Figure 5.2: Scanning system layout.

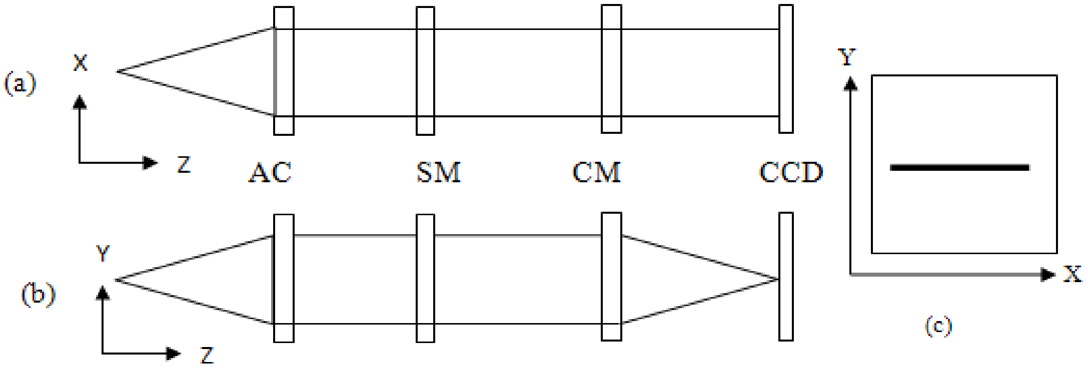

Figure 5.3: Beam paths of the scanning system: (a) in the x-z plane, (b) in the y-z plane, and (c) the CCD view.

Though the focal plane of the mirror is half of its ROC, due to off-axis configuration, the focal plane position (FPP) will be a function of the scanning system configuration. For performance evaluation, the FPP was optimized by using ZEMAX optical design software within a 2mm scan range. First, the model was optimized for the FPP position with the beam at the center (C) of the cylindrical mirror. In the case of the 51.7mm FL mirror, the optimized FPP was 47.77mm. Then the FPP position was optimized for the two beam off-set positions from the centre of the cylindrical mirrors. The optimized FPP for both cylindrical mirrors with the beam positions at the center (C) of the mirror, 1mm off-set (C+1), and 2mm off-set (C+2) from the center is tabulated in Table 5.1.

Table 5.1: Optimized FPPs from the ZEMAX optical model.

Incident Beam position on the cylindrical mirror	For 51.7mm FL mirror	For 25.85mm FL mirror
Center (C)	47.77	23.90
Centre + 1 (C+1)	47.19	23.38
Centre +2 (C+2)	46.61	22.74

5.3 Experimental setup

The experimental setup consists of a superluminescent diode (SLD) laser, a scanning mirror, a cylindrical focusing mirror, and a CCD detector. The spectral bandwidth of the SLD light source (Superlum HP-371) at full-width-half-maximum (FWHM) is 53nm with a center wavelength of 843nm. The theoretical axial resolution with this source configuration is ~6µm. The beam was collimated by using a custom-made pigtail achromatic collimator (OZoptics). This collimator was specially designed for a wavelength range of 800nm to 880nm with a focal length of 10mm and 0.14 NA single mode fibre (Corning HI-780) to provide a 2mm (1/e^2) collimated beam. The cylindrical mirrors were fabricated by applying a reflective coating on plano-concave cylindrical lenses (Thorlabs, LK1743L1 and LK1069L1). The ROCs of the cylindrical mirrors used for this study was 103.4mm and 51.7mm with an aperture size of 8mm by 8mm. The cylindrical mirror was mounted on an XY stage (Melles Griot, 07 TMC 502). A flat mirror was used as a scanning mirror mounted on a tilt and rotation stage (Newport, M-PO46N-50) for spatial scanning. Manual scanning was performed by using stage rotations in order to change the beam position on the detector, which can be replaced by a MEMS scanning mirror in the case of endoscopic probes. An area scan CCD camera (JAI CV-A11) was used to capture the beam profile. The resolution of the CCD was 644 by 492 pixels with a pixel size of 7.4μm^2. The CCD housing was removed to avoid beam blocking, as discussed in Section 6.1. The CCD was mounted on an XYZ stage, which was built with two Melles Griot (07 TMC 502) micro stages for the X and Y movement and a Newport (M-460A series) micro stage for the Z-axis movement.

5.4 Scanning procedure

First, the collimated beam was aligned straight, and the beam was incident on the flat mirror. The flat mirror was placed at an angle of 22.5° with respect to the collimated beam, providing the angle 'ϕ' between the incident and reflecting beams as 45°, as shown in Figure 5.2. The cylindrical mirror was positioned at a distance of 35mm from the flat mirror. The beam was aligned parallel to the initial collimated output beam and positioned at the center (C) of the cylindrical mirror using XY micro stage. Then the CCD camera was positioned at the optimized focal plane of the cylindrical mirror by translating the micro stage in Z-axis. Then the focussed beam was positioned at the center of the CCD by using the XY micro stage, which is denoted as the centre position (0mm scan position) of the scan field. After the beam was aligned at the 0mm scan position, the SLD power was adjusted to avoid saturation on the CCD (shown in Figure 5.4). Neutral density filters were used to reduce the background noise. Scanning was carried out by using the tilt and rotation stage. Five line profiles that were captured for performance evaluation within the 2mm scan range at -1mm, -0.5mm, 0mm, 0.5mm and 1mm, are shown in Figure 5.5.

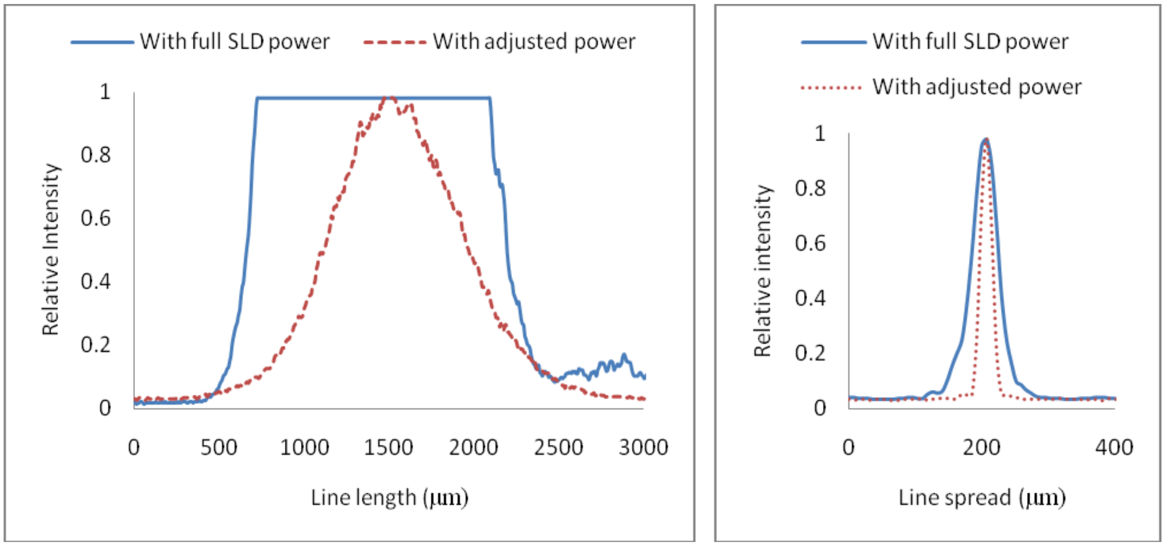

(a) (b)

Figure 5.4: Saturated and unsaturated line profile (a) in the line direction and (b) in the focusing direction.

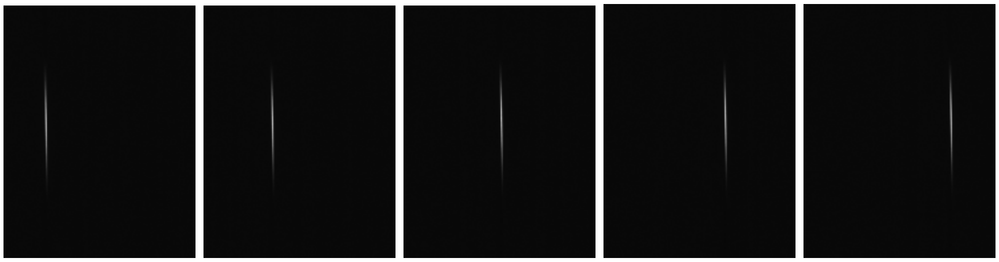

-1mm -0.5mm 0mm 0.5mm 1mm

Figure 5.5: Line profiles at different scan positions.

The beam position on the focusing mirror is a critical issue for the scanning system in order to maintain the imaging quality throughout the scan range. Results from our earlier model [79] prove that in the case of beam off-set from the center of the focusing optics, the cylindrical mirror provides better performance than either that of the plano-convex cylindrical lens or that of the achromatic cylindrical lens focusing. In order to evaluate the performance of the designed scanning system under these conditions, an intentional beam offset of 1mm and 2mm away from the center of the mirror was provided by moving the cylindrical mirror in the Y-axis. Then five beam profiles were then captured by using the CCD in the above-mentioned scan positions within the 2mm scan range for each offset. In both cases, the CCD camera position was adjusted at the center with respect to the 0mm scanning position by moving the XY micro stage. In the case of 51.7mm FL mirror, experiments were done at fixed focal plane positions and at optimized focal plane positions, and, in the case of the 25.85mm mirror, the experiments were carried out only with optimized focal plane positions. The SLD power was adjusted in such a way that there was no saturation at any of the five positions within the 2mm scan range. This power was maintained for the subsequent experiments.

5.5 Results and discussion

The scan map was reconstructed from the five beam profiles captured using a program written with LabVIEW software. The beam profiles were captured as image files and then converted into intensity text-array data. The portion of the beam profile that contained the line image data was then extracted from the arrays and stitched together to build the scan map. The scan range in the X-direction was determined by the incident beam size, which was 2mm in the developed system. In the Y-direction, the 2mm scan range was covered by the rotation of the scanning mirror. Figure 5.6 shows 2D scan map and 3D beam profiles of the five focused lines within the scan range of 2mm by 2mm from which en-face OCT imaging data can be acquired and the depth information can be obtained in combination with the spectral domain (SD) acquisition.

The Strehl ratio (SR) is one of the quality assessment parameters for the optical system [84, 110]. The Strehl ratio is the ratio between the aberrated spread function and the aberration-free spread function. In order to evaluate the imaging quality of the developed scanning system, the Strehl ratio was recorded from the model and it was verified experimentally.

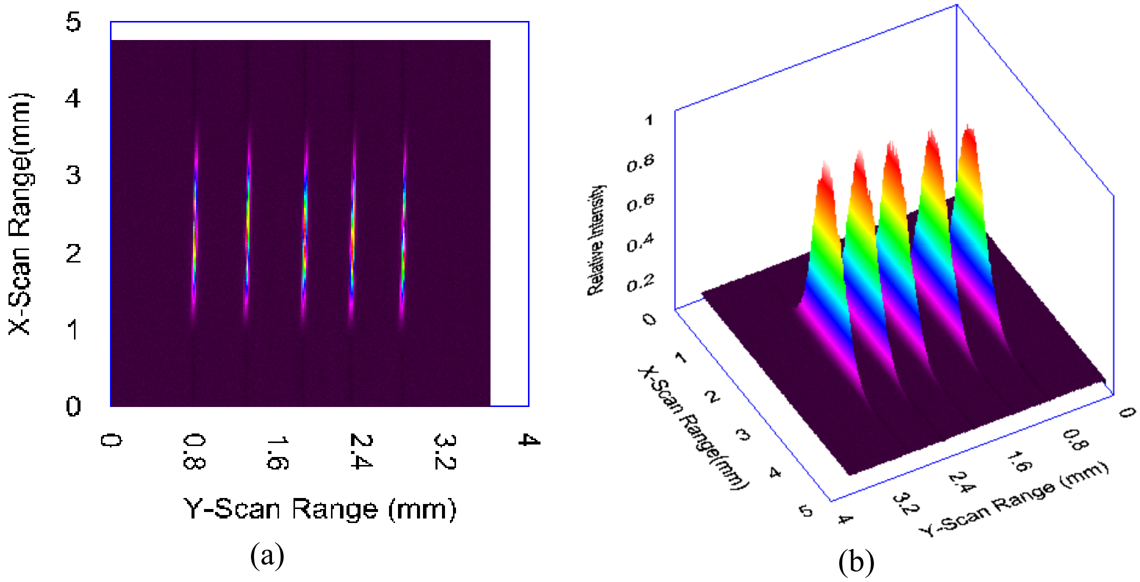

(a)

(b)

Figure 5.6: (a) 2D scan map and (b) 3D beam profiles of 2mm by 2mm scan range.

5.5.1 Performance analysis for 51.7mm FL mirror

From the ZEMAX model, SR data was obtained from the cross section of the line at the centre of the beam profile. The SR measurements for the beam positions at center (C) of the mirror, 1mm off-set from the centre (C+1), and 2mm off-set from the centre (C+2) measured at the fixed focal plane of 47.77mm are shown in Figure 5.7 (a), (b), and (c), respectively. In the case of the beam position at C for which the focal plane was optimized, the SR values are very high and in the case of C+1 and C+2, the model and experimental results show higher variations in the SR within the scan range. However, the SR is better than the Marechal criterion throughout the 2mm scan range for the beam position at C and C+1. In the case of the 2mm beam off-set, the SR is slightly lower than the Marechal criterion at one end. However, the trends of the SR measurements for all three cases are the same and show good agreement between the optical model and the experimental results with a maximum deviation of ~6%.

As the beam moves from the centre of the mirror, the effective FPP changes due to the ROC of the mirror and the off-axis scanning system configuration, affecting the imaging quality. This can be improved by optimizing the FPPs for the specific beam off-set position as shown in Table 5.1. If the FPPs are optimized, the ZEMAX model shows an SR of 0.99 throughout the 2mm scan range regardless of the beam offset. Hence, only the experimental results with optimized FPPs are shown in Figure 5.8, which shows good agreement with the model results. The SR is better than the Marechal criterion throughout the 2mm scan range, regardless of the beam offset.

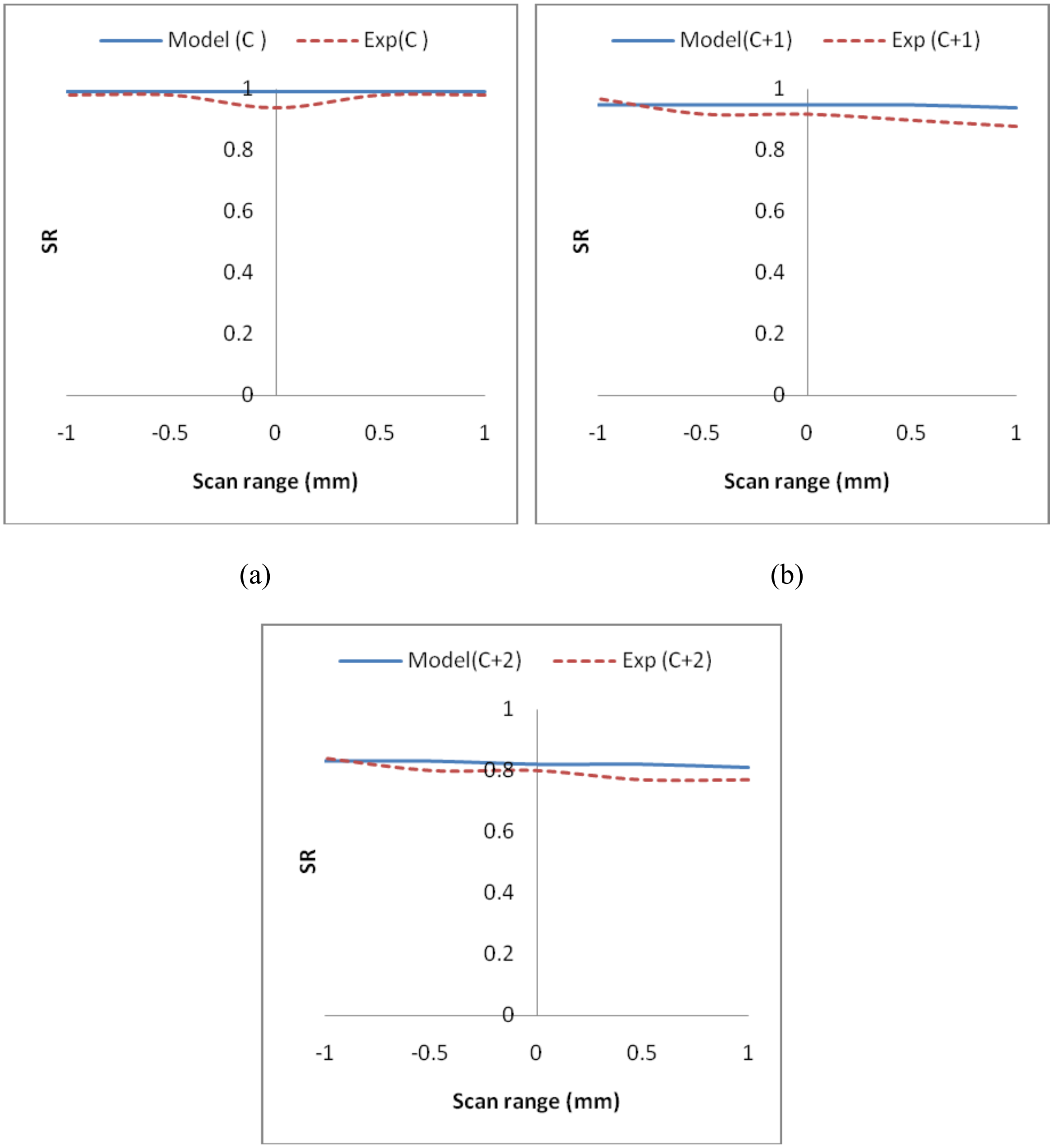

(a) (b)

(c)

Figure 5.7: Model and experimental results with the beam position at (a) C, (b) C+1 and (c) C+2.

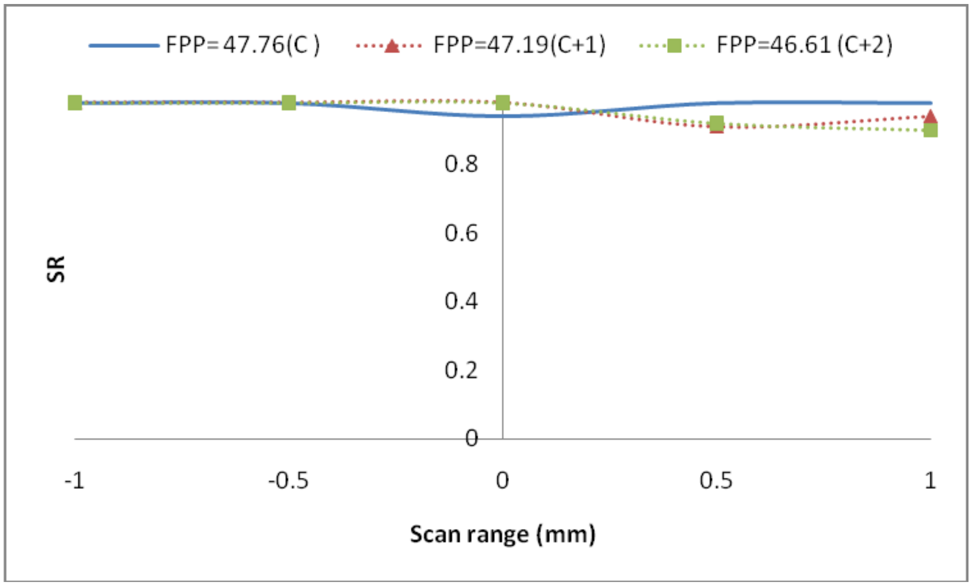

Figure 5.8: Experimental results with optimized FPPs for 51.7mm FL mirror.

5.5.2 Performance analysis for 25.85mm focal length

In the case of endoscopic imaging applications, transverse resolution can be improved only by using a lower FL focusing optics due to the size restriction of the scanner probe. In our experiments, the performance was evaluated with a 25.85mm FL cylindrical mirror for higher transverse resolution scanning. The imaging performance produced by the ZEMAX model with the first optimized focal plane position set at 23.91mm is shown in Figure 5.9. If the beam position is at C, the SR is in the acceptable range within 1mm of the 2mm scan range whereas in case of beam off-sets, the SR varies significantly from 0.91 to 0.32 and 0.43 to 0.2 within the scan range.

This variation in SR is due to the fact that the optical angle required for scanning the 2mm range is much higher due to the smaller ROC [79]. The variation is even more pronounced if the beam is moved from the centre of the mirror with lower ROC.

However, the imaging quality can to some extent be improved by optimizing the FPPs for each beam off-set. Hence, in this case, the experiments were carried out only with the optimized FPPs.

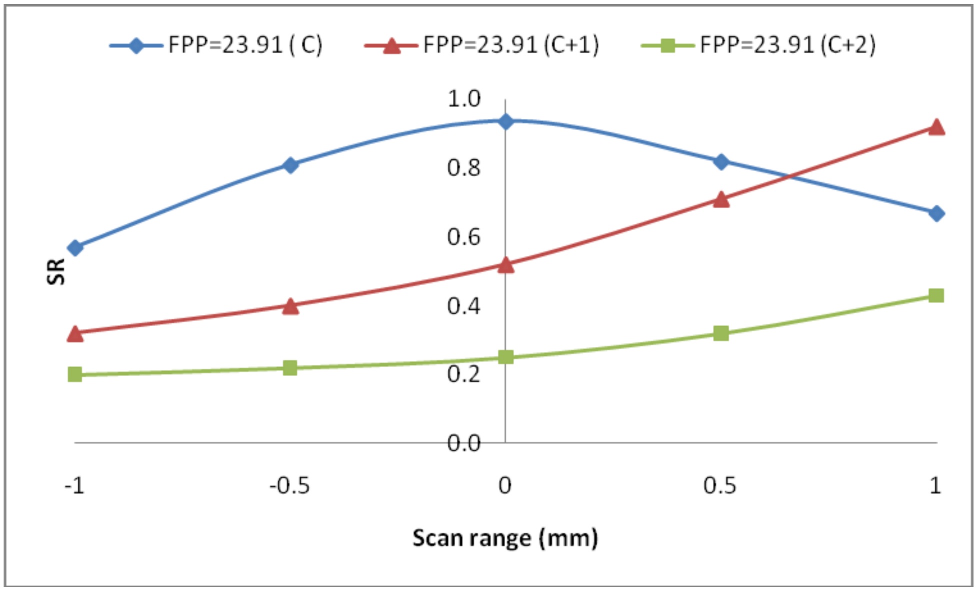

Figure 5.9: Model results with a 23.91mm FPP for the three beam positions on the mirror.

Figure 5.10 (a), (b), and (c) show the comparison between the model and experimental results for a 25.85mm FL mirror for the beam positions at C, (C+1), and (C+2). For this three beam positions, the experimental results were in good agreement with the model results on one side of the 2mm scan range and the deviation is higher on the other side. This trend is similar to the one seen in experiments with 51.7mm FL cylindrical mirror and this is due to the fact that, in the off-axis mirror arrangement, the scanning angle moves the beam away from the optical axis on one side, thus deteriorating the image quality.

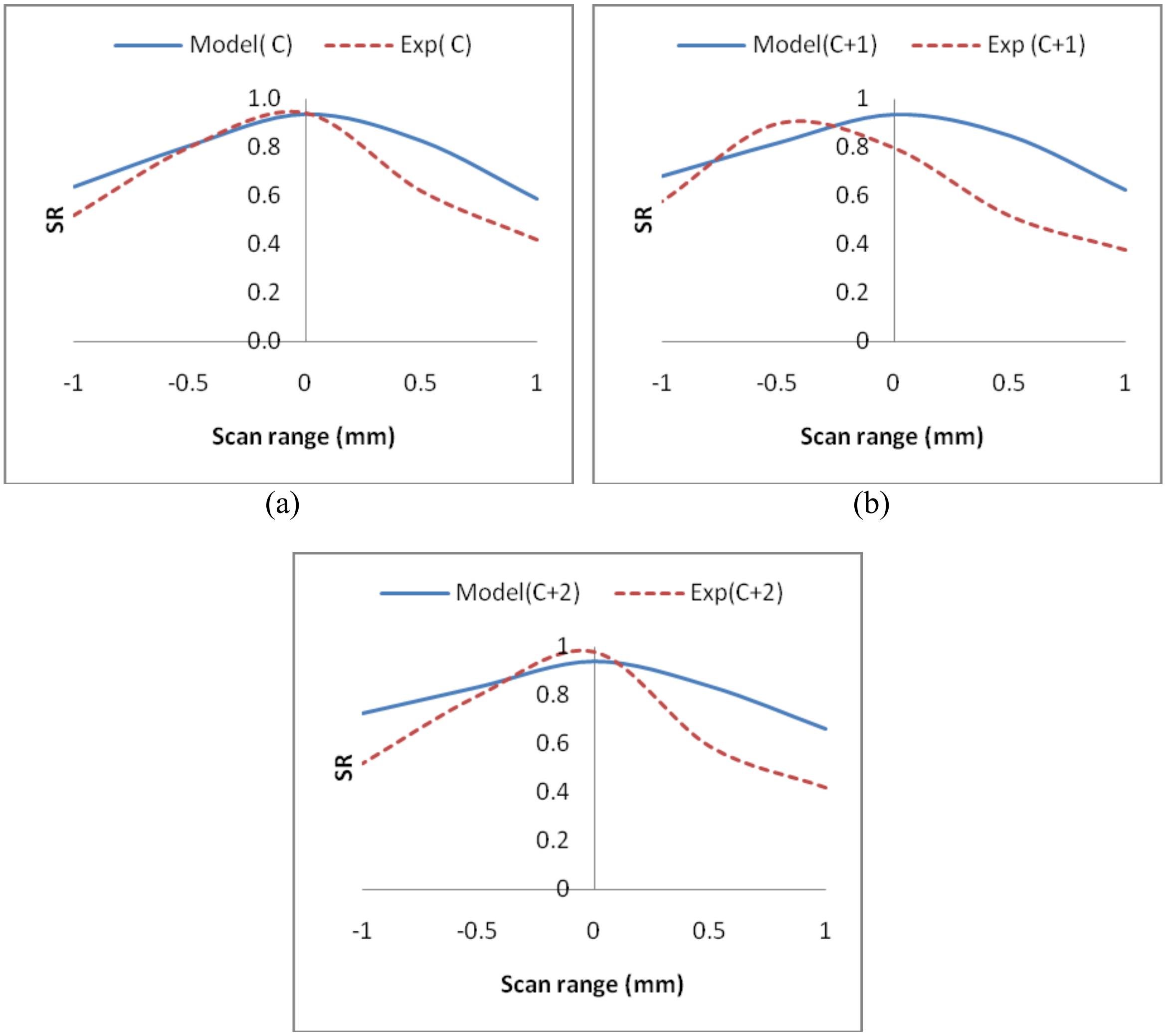

(a) (b)

(c)

Figure 5.10: Model and experimental results with the beam position at (a) C, (b) C+1, and (c) C+2 for a mirror the 25.85mm FL.

As shown earlier, the imaging quality of the scanning system reduces within the scan range while scanning with a lower FL mirror. Due to the off-axis arrangement, the imaging quality is determined by the geometrical configuration of the scanning system. In the model and experiments the same configuration was used to evaluate the imaging quality of the developed scanning system. However, the optical scan angle is 2.4° for the 51.7mm FL mirror whereas the scan angle is 4.8° in the case of the 25.85mm FL mirror

[79], thereby increasing the angular variation between the incident and reflected beams. Once the angular variation is higher between the incident beam and the reflected beam, the imaging quality significantly drops.

5.5.3 Imaging quality improvement

The advantage of using cylindrical reflective optics is that en-face scanning is needed in only one direction. If the scan direction is changed in such a way that the incremental angle is in the orthogonal plane to that of the optical axis, the affect of the incident angle is negligible. Optical design software does not allow us to change the focussing as well as the scanning direction to the X-axis instead of the Y-axis. So the imaging quality was assessed experimentally by changing the focusing and the scanning direction from Y to X by rotating the cylindrical mirror by 90° in the X-Y plane. Figure 5.11 shows the experimental results of X and Y scanning for a 25.85mm mirror at a beam position at C.

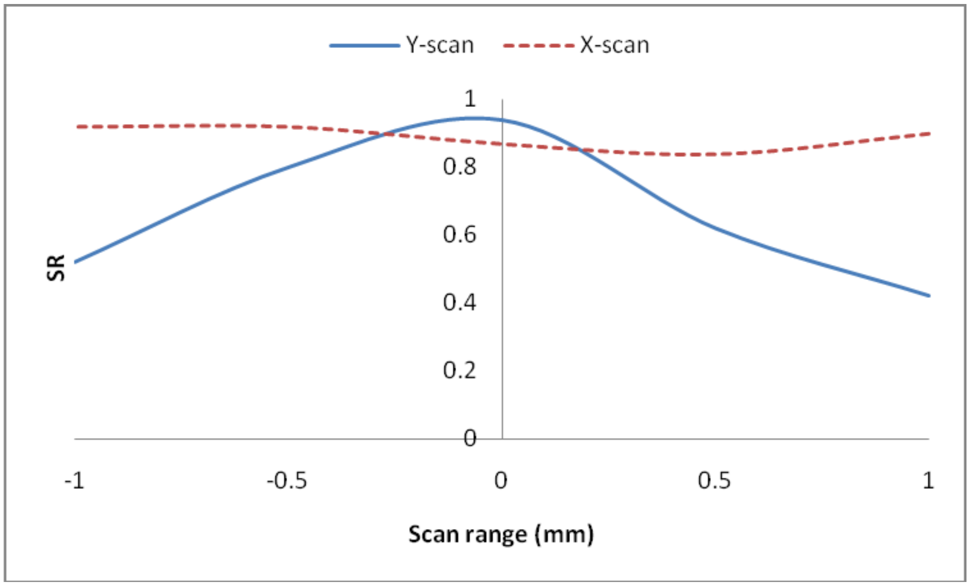

Figure 5.11: Comparison of the experimental results for the Y and X direction.

Figure 5.12 shows the 3D beam profiles of a 2mm by 2mm scan range. Results show that the system maintains SR higher than the acceptable limit throughout the scan position. From the results, it is evident that the SR improved by changing the focusing and scanning direction. Further study is required to verify the effects of the angle between the incident and reflected beam at various offset positions by using the X and Y scanning system configurations

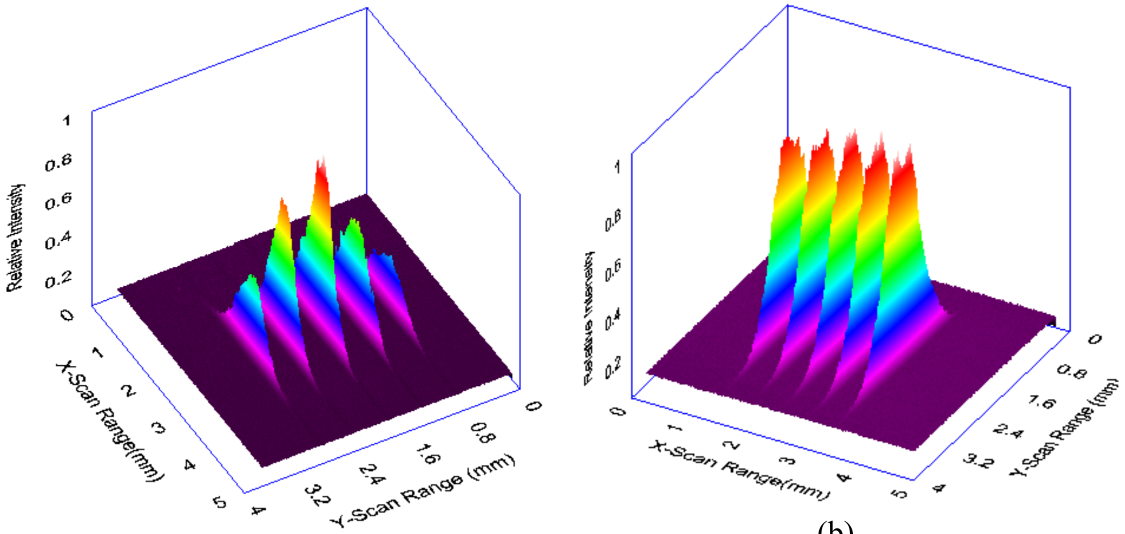

(a) (b)

Figure 5.12: 3D scan map showing (a) Y-direction scanning and (b) X-direction scanning.

5.6 Conclusions

An off-axis cylindrical mirror focused line scanning system was developed to provide high imaging quality. Mirrors with focal lengths of 25.85mm and 51.7mm were used to evaluate the imaging quality of the scanning system. The cylindrical mirror focuses a 2mm collimated beam as a line onto a CCD. Manual scanning was performed to scan 2mm range in the focusing direction and the line size was 2mm. The developed scanning system covers a 2mm by 2mm *en-face* scanning area by using a single-axis scanner. A 53nm spectral bandwidth light source with a center wavelength of 830nm was used in the developed system. Strehl Ratio (SR) was used to evaluate the imaging quality of the developed scanning system. Three incident beam positions were used to evaluate the beam positioning sensitivity of the scanning system. For a 51.7mm FL cylindrical mirror, the experimental results showed good agreement with optical model predictions and maintained SR better than the Marechal criteria throughout the 2mm scan range. When the 25.85mm FL cylindrical mirror was used, the variation of the SR between the experimental measurements and the model prediction was higher. However, the trend of the SR was consistent throughout the 2mm scan range for three incident beam positions. When the 25.85mm FL mirror was used, a higher optical scan angle was required to scan a 2mm scan range compared to the 51.7mm mirror. Therefore, the variation of the angle between the incident and the reflected beam was higher. As a result the SR drops once the beam moves away from the optical axis. An optimized orthogonal scanning scheme was tested, and the result showed performance improvement. Further study is presented in Chapter 6 to confirm the effect of the incident angle, distance between the mirrors, and scanning directions on the imaging quality of the scanning system.

Chapter 6: Optimized line-scanning system parameters

Modified optical model and the experimental validation of the reflective optics based scanning system were presented in Chapter 5 and it has been concluded that the imaging quality can be further improved by optimizing the scanning system parameters and by changing the scan direction from tangential to sagittal plane. In the current chapter, the effect of scanning system parameters and scan direction on the imaging quality is presented. This chapter is a reproduction of the manuscript that was submitted to the Journal of Biomedical Optics (Manuscript ID-JBO 11373) [94]. This chapter covers the objective '1e' of the Objective and scope of the thesis as detailed in Section 1.11.

6.1 Introduction

Optical coherence tomography (OCT) is a high resolution, non-invasive cross-sectional imaging technology [4]. In OCT, a single-axis or a two-axis scanner is required to obtain two-dimensional (2D) or three dimensional (3D) imaging [61, 67]. A pre-objective or a post-objective lens scanning configuration is commonly utilized in OCT imaging. To perform the scanning using a pre-objective configuration, the beam is required to move away from the optical axis of the lens. . Consequently, a complex lens system design is required to maximize the imaging quality throughout the scan range [81]. On the other hand, a simple lens system is sufficient in the case of post-objective lens configuration, but the resultant scan field is not flat [77, 81, 82]. To achieve a flat scan field in the post-objective configuration, Polygon scanner mirrors are commonly used [111]. However, they are not suited for endoscopic scanning owing to their large size. Moreover, a broader spectral-band light source is required in OCT imaging for a higher axial resolution and the effective focal length (EFL) of the lenses varies as a function of the wavelengths [112]. Consequently, the imaging quality of the lens-focused scanning system is reduced due to the chromatic aberration [39]. In addition, the imaging quality of flying spot scanning is also reduced because of the distortion errors [45] and motion artifacts such as eye or body motion [46].

A line-scanning (LS) system that uses cylindrical lens-focusing has been reported for high-speed OCT imaging [47, 48, 52, 53]. In LS-OCT, a collimated beam is focused as a line on the sample by using cylindrical optics. The line size in the focusing direction is determined by the numerical aperture (NA) of the objective lens whereas in the other direction it remains the same as that of the collimated beam. 2D cross-sectional imaging data can be obtained by using line focused scanning with spectral-domain (SD) acquisition without requiring a mechanical scanner. On the other hand, the 3D image data can be obtained by using line scanning with SD acquisition by integrating only a single axis scanner. As a result, line-field scanning increases the scanning speed while maintaining the sensitivity advantage of flying spot scanning with SD acquisition [47]. However, the line-scanning systems developed so far, use lenses to focus the beam, thereby affecting the image quality, which is degraded by the chromatic aberration and scanning distortion errors. Mirror focusing is an alternative that can eliminate the chromatic aberration as the mirror is insensitive to the spectral bandwidth of the light source. In Chapter 2 and Chapter 3 [79, 90], a mathematical model and optical design of a cylindrical mirror-based scanning system have been reported. It was proved that, for OCT applications, the mirror focusing performs better than the lenses.

The transverse resolution depends on the numerical aperture of the scanning system and can be increased by using either a larger beam or a cylindrical mirror with a shorter EFL. In the case of endoscopic OCT imaging, the probe size prevents the use of a larger beam. Consequently, the only way to increase the transverse resolution is by using a mirror with a shorter EFL. The imaging quality of the mirror-focused scanning system does not depend on the spectral bandwidth of the light source [79]. However, due to off-axis arrangement of the scanning system layout, the imaging quality is dependent on the geometrical arrangement of the scanning system. The scanning system parameters include the following: the incident beam size, the distance between the mirrors, the angle between the incident and reflected beams, the optical scan angle, and the effective focal length (EFL) of the cylindrical mirror. The optimization of these parameters is required to maximize the imaging quality throughout a target scan range.

In this chapter, the results of a modified optical model and the experimental validation of that model are presented. The effects of the angle between of the incident and reflected beams 'ϕ', the distance between the mirrors 'd', and the EFL of the cylindrical mirror, on the flatness of the scan field were studied. In addition, scanning was performed both in the tangential (Y-scan) and in the sagittal (X-scan) planes to evaluate the effect of scanning direction on the flatness of the scan field. Two beam off-set positions from the centre of the cylindrical mirror were studied to evaluate the robustness of the cylindrical mirror scanning to beam-position variations. The scan field flatness was evaluated using the Strehl Ratio (SR).

6.2 Scanning system configuration

Consider that, in the scanning system configuration shown in Figure 6.1, the laser beam which is incident on a scanner mirror at N, is then reflected onto a cylindrical mirror at a point C. The beam is finally focused onto the target at R. The radius of curvature of the cylindrical mirror is r. The angle between the incident and the reflected beams is 'ϕ', the distance between the two mirrors is $CN=d$, and the focal plane position of the cylindrical mirror is $CR=f$. An optical scan angle of θ is required to scan a target scan range of 'L_s'. The details of this model and the scanning procedure can be found in Chapter 2 and Chapter 3 [79, 90].

A collimated beam is required to sweep on the cylindrical mirror in order to scan the target range L_s. Because of this beam sweeping, the optical scan angle varies from $-\theta/2$ to $+\theta/2$ with respect to the angle 'ϕ'. For this optical scan angle, the angle between the incident and reflected beams varies from $(\phi - \theta/2)$ to $(\phi + \theta/2)$. This angular variation also depends on the distance between the mirrors and the radius of curvature of the focusing mirror. The focal length of the cylindrical mirror is half of the radius of curvature while the beam is in the optical axis of the mirror. Using an off-axis scanning system configuration, the effective focal length (EFL) is determined by the d, θ, r, and ϕ of the configured system [90]. The EFL positions also vary according to the beam position on the cylindrical mirror.

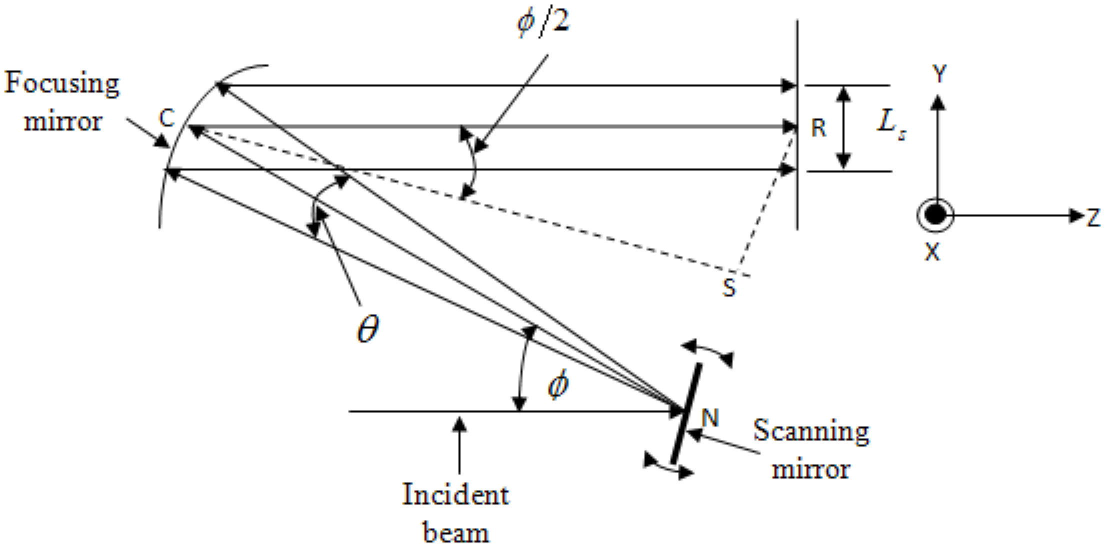

Figure 6.1: Scanning system configuration with a Y-axis scanning.

The advantage of using the cylindrical mirror is that en-face scanning requires only one directional scans. Therefore, a cylindrical mirror can be used to perform en-face scanning either in the tangential plane (Y-scan) or in the sagittal plane (X-scan) by focusing the beam in the respective direction. A map of en-face scanning performed by using a Y-scan and by using an X-scan is shown in Figure 6.2 (a) and (b) respectively. If the scan direction changes from the Y-scan to the X-scan, the influence of the angle 'ϕ' is diminished because the scanning is performed in the orthogonal direction with respect to the incident beam. As a result, the position of EFLs within the scan range varies as a function of d and θ. Hence, for a fixed d and r, the EFL positions within the scan range vary as a $f(\phi, \theta)$ in the case of tangential scanning whereas it varies as a $f(\theta)$ in the case of sagittal scanning.

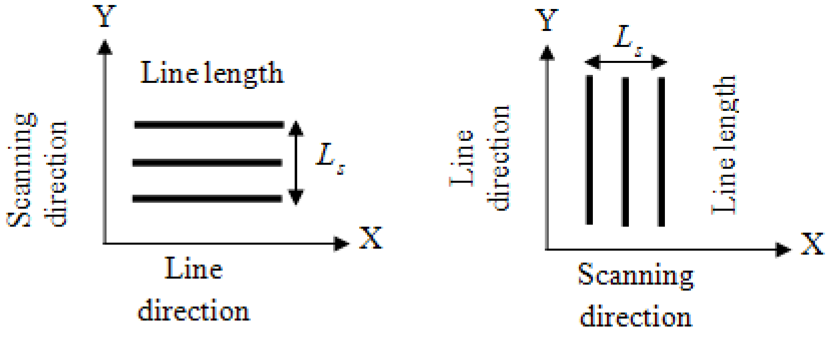

(a) (b)

Figure 6.2: 2D scan map of the (a) tangential(Y-scan) and (b) sagittal(X-scan) scanning.

6.3 Optical simulation using the Y-scan system configuration

To evaluate the flatness of the scan field, a 2mm beam and cylindrical mirrors with radius of curvatures (ROC) of 51.7mm and 103.4mm were used. Therefore, the EFL of these mirrors is 25.85mm and 51.7mm respectively. Strehl Ratio [79] was used for performance evaluation. An 843nm centre wavelength light source with a spectral range of 800nm to 880nm was used in the ZEMAX model. Since mirror-focusing is insensitive to wavelength bands and it maintains zero chromatic focal shifts [79], this system can be used for any broader spectral bandwidth light source that is required for OCT imaging. The influence of the scanning system parameters was simulated for a 2mm by 2mm scan field by using the ZEMAX optical design software.

6.3.1 Effect of the distance (*d*)

The effect of the distance between the scan mirror and the cylindrical mirror '*d*' was studied with the ZEMAX software for 25.85mm and 51.7mm FL mirrors with an angle 'ϕ' of 45° for five different distances of '*d*'. The Strehl Ratio was recorded at five different positions within the 2mm scan range. In the ZEMAX model, five beam positions with an interval of 0.5mm were defined within the 2mm scan range. These scans at positions, indicated by -1mm, -0.5mm, 0mm, 0.5mm and 1mm, scan are shown in Figure 6.3. The results are shown in Figure 6.4 for a 51.7mm FL mirror and Figure 6.5 for a 25.85mm FL mirror. The simulation results show that, in the case of the 51.7mm FL, almost the same SR was maintained throughout the 2mm scan range when the distance between the mirrors '*d'* was 50mm or lower (lines are overlaps in Figure 6.4), and if the distance was more than 50mm, the SR drops slightly towards both ends.

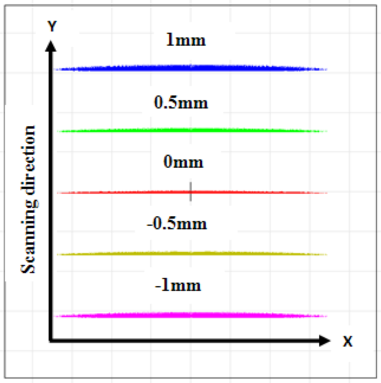

Figure 6.3: Five beam positions in the 2mm by 2mm scan field.

In the case of the 25.85mm FL mirror, a good SR is maintained when the mirror is located at *'d'* less than or equal to 25mm. For a larger distance, the imaging performance drops significantly towards the ends of the scan range. Therefore, to achieve a high imaging quality, the distance between the mirrors should be equal to or less than the FL of the mirror. However, due to the experimental constraints, the distance between the mirrors *'d'* of 35mm was used for experiments.

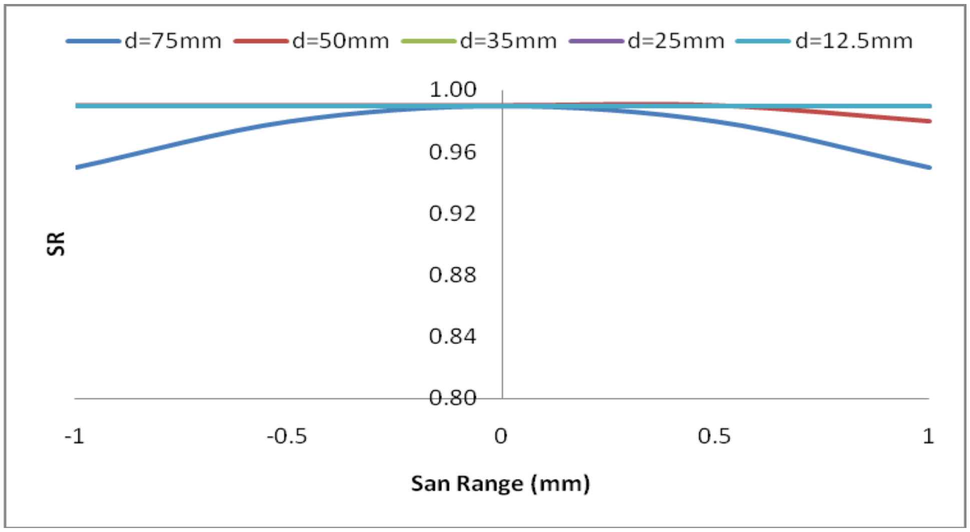

Figure 6.4: Variation of SR for different ‘d’s for 51.7mm FL mirror.

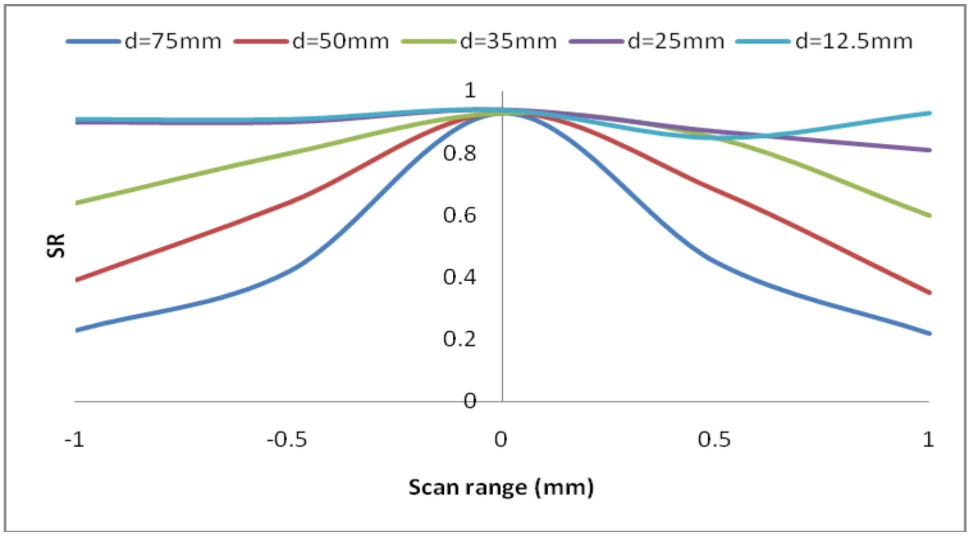

Figure 6.5: Variation of SR for different ‘d’s for 51.7mm FL mirror.

6.3.2 Effect of the incident angle (ϕ)

Table 6.1 shows the value of the parameters that were used in the ZEMAX model to evaluate the effect of the incident angle. The optical scan angle from the ZEMAX and the angular variations ($\phi \pm \theta/2$) for 51.7mm and 25.85mm FL mirrors with different ϕ are given in Table 6.2. Here, the optical scan or the angular variation corresponds to the 2mm scan range for a defined ϕ.

Table 6.1: ZEMAX model parameters

r (mm)	d (mm)	ϕ
103.4	35	30°,45°,60°
51.7	35	30°,45°,60°

Table 6.2: Angular variations simulated using the ZEMAX for a 2mm scan range

	Optical scan angle (θ)		Angular variation ($\phi \pm \theta/2$)	
ϕ	25.85mm FL	51.7mmFL	25.85mm FL	51.7mmFL
30°	4.4°	2.2°	27.8° – 32.2°	28.9° – 31.1°
45°	4.8°	2.4°	42.6° – 47.4°	43.8° – 46.2°
60°	5.2°	2.6°	57.4° – 62.6°	58.7° – 61.3°

The focal plane position (FPP) was optimized with a different angle of ϕ for the best SR within the 2mm scan range. The optimized FPP positions of the 51.7mm FL mirror and the 25.85mm FL mirror are given in Table 6.3. Figure 6.6(a) shows the SR comparisons with these incident angles for a 51.7mm FL mirror, and Figure 6.6(b) shows the SR comparisons for a 25.85mm FL mirror at optimized FPP for the specific 'ϕ'. In the case of the 51.7mm FL mirror, the SR remained better than the Marechal criteria throughout the 2mm scan range regardless of the angle 'ϕ'. In the case of the 25.85mm FL mirror, the SR was higher than the Marechal criteria throughout the 2mm scan range when the incident angle was 30°. However, in the case of the 45° and 60° angles, the SR drops towards both ends of the 2mm scan range. The SR drops because a higher optical angle is required when using a lower FL mirror to scan the same 2mm range.

Table 6.3: Optimized FPPs with different ϕ

ϕ	FPP(51.7mm FL)	FPP(25.85mm FL)
30°	49.939	24.992
45°	47.767	23.913
60°	44.778	22.43

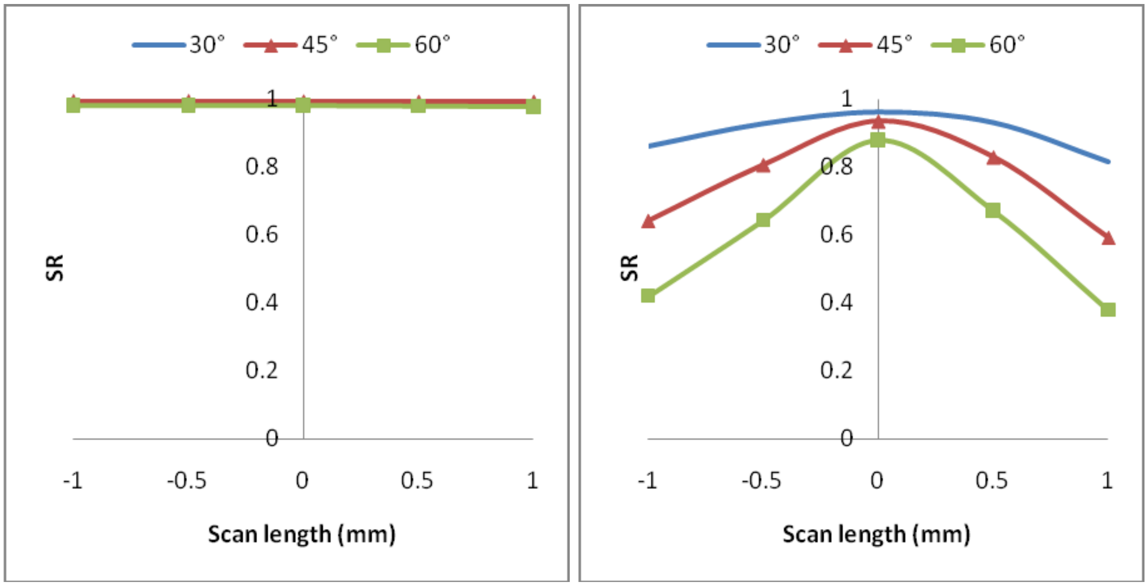

(a) (b)

Figure 6.6: SR comparisons at different incident angles using (a) a 51.7mm FL mirror and (b) a 25.85mm FL mirror.

The model was optimized for a best SR for each beam position within the 2mm scan range. The effective focal length (EFL) position was optimized individually for five different beam positions. The EFL position variations with different incident angles for

51.7mm FL mirror and 25.85mm FL mirror are shown in Figures 6.7(a) and (b), respectively. The results show that the variation of the EFL position (ΔEFL) is higher when reducing the FL of the mirror and/or increasing the angle between the incident and reflected beams. For example in the case of the 51.7mm FL mirror, ΔEFL is 250µm from the center to one end of the scan field with *ϕ=60°* compared to a ΔEFL of 50µm with *ϕ=30°*. Similarly at *ϕ=60°*, the ΔEFL varies from 250µm to 874µm if the FL of the mirror is changed from 51.7mm to 25.4mm. Because of this higher ΔEFL, the imaging quality drops significantly towards the ends of the scan field. In order to obtain high imaging quality, the angle between the incident and reflected beams '*ϕ*' should be 0º making it an on-axis scanning system. Since this is not possible, flat scan field can be achieved by using an angle of *ϕ*, which is as low as the design would permit.

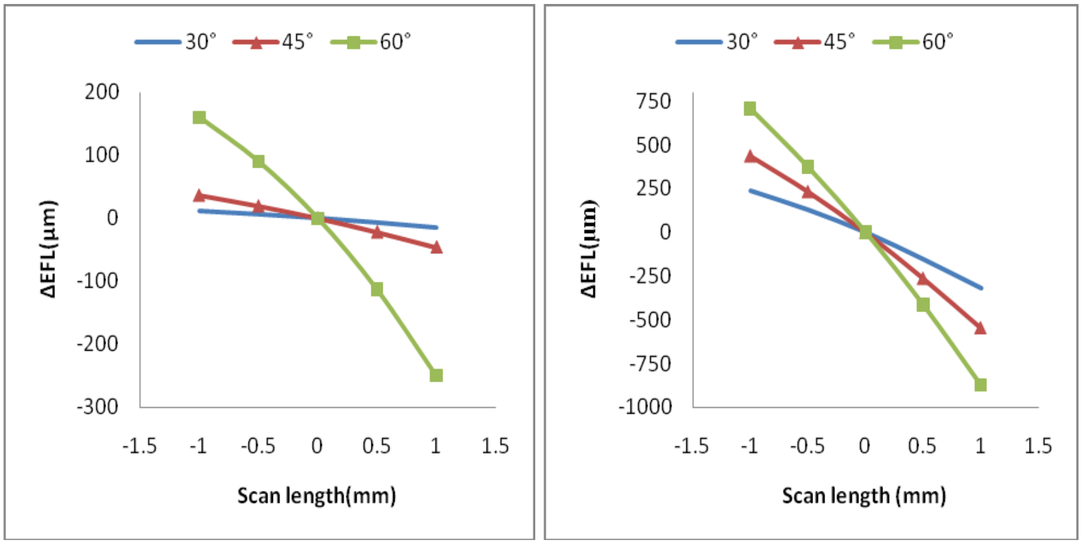

(a) (b)

Figure 6.7: EFL position variations at different incident angles with (a) a 51.7mm FL mirror and (b) a 25.85mm FL mirror.

6.4 Experimental setup

The experimental setup consists of a superluminescent diode (SLD) laser, a scanning mirror, a cylindrical focusing mirror, and a CCD detector, as shown in Figure 6.8. The spectral bandwidth of the SLD (Superlum HP-371) at full-width-half-maximum (FWHM) is 53nm with a center wavelength of 843nm. The beam was collimated by using a custom-made pigtail achromatic collimator (OZoptics) to 2mm. The ROCs of the cylindrical mirrors used for this study was 103.4mm and 51.7mm with an aperture size of 8mm by 8mm. A flat mirror mounted on a tilt and rotation stage (Newport, M-PO46N-50) was used as a scanning mirror. A 644 by 492 CCD camera (JAI CV-A11) with a pixel size of 7.4μm^2 was used to capture the beam profile.

The beam reflected from the scanning mirror is blocked by the CCD camera housing before reaching on the cylindrical mirror. Hence, for the experiments, the housing was removed from the camera, enabling the use of both 51.7mm and 103.7mm ROC mirrors with a distance *'d'* of 35mm. The reduction of the distance *'d'* below 35mm or using mirrors with ROC less than 51.7mm is still not possible with the CCD camera. Five line profiles that were captured for performance evaluation within the 2mm scan range are at -1mm, -0.5mm, 0mm, 0.5mm and 1mm. The captured beam profiles were analyzed using a program written using LabVIEW software.

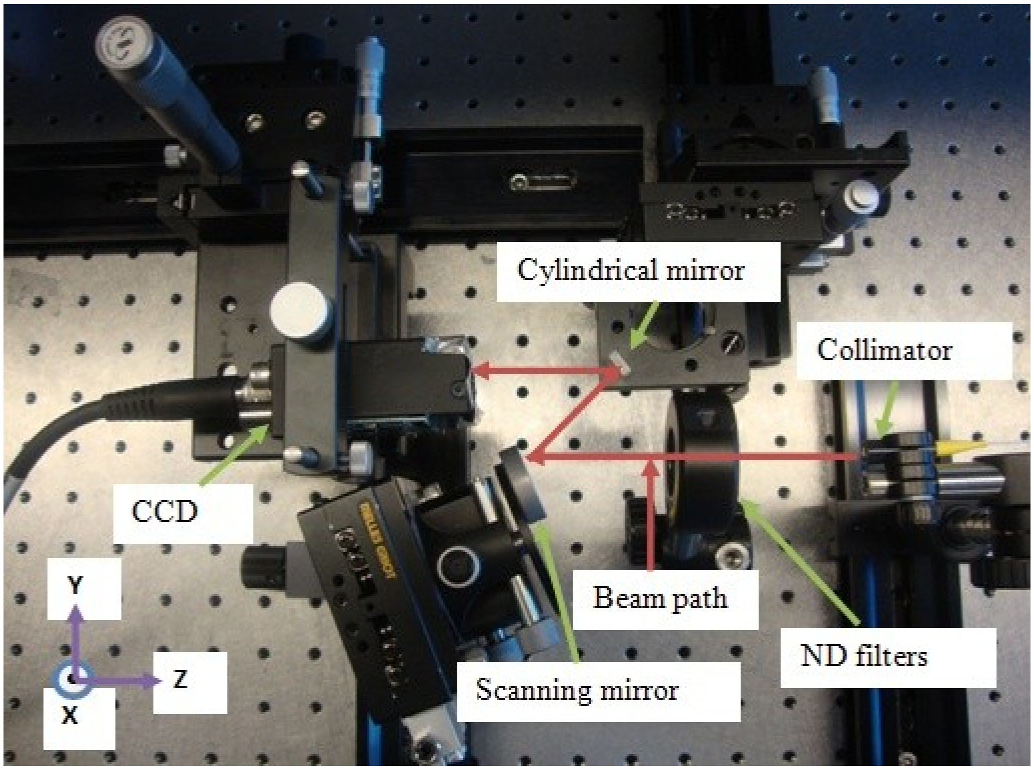

Figure 6.8: Experimental setup of the scanning system.

6.5 Result and discussion

Consistency of the imaging quality throughout the target scan range is required to maintain the flatness of the scan field. Y-scans and X-scans were performed by rotating the scanning mirror in the respective direction for a target scan range of 2mm. The Strehl Ratio (SR) was used to evaluate the flatness of the scanning system with 51.7mm FL and 25.85mm FL mirrors. Spread function was used to obtain the SR from the ZEMAX model as well as from the experimental measurements.

6.5.1 Flatness evaluation with Y-scan system configuration

In the Y-scan configuration, the collimated beam was focused in the Y-axis while the X-axis remained the same as the collimated beam size. The system parameters that were discussed in Section 6.3 were used for the experiments. The scanning was performed by rotating the scanning mirror in the Y-axis. Five beam profiles were captured with an interval of 0.5mm within the 2mm scan range. The experiments were repeated for the incident angles of 30°, 45°, and 60° with a distance of *d=35mm*. Comparisons of SR between ZEMAX modeling and the experiments for a 51.7mm FL mirror, with the beam positons set at incident angles of 30°, 45°, and 60°are shown in Figure 6.9(a), (b), and (c), respectively. In the case of 30° and 45° incident angles, the SR remained above the Marechal criteria throughout the 2mm scan range. In the case of the 60° incident angle, the SR is 2.5% lower than the Marechal criteria at one end of the 2mm scan range.

Because of the off-axis configuration, the beam is blocked by the camera housing for $\phi<45°$ with a 25.85mm FL. Thus, the experiments were restricted to $\phi=45°$ and $\phi=60°$ with a 25.85mm FL. In the case of shorter FL mirrors, a larger optical scan angle was required to scan the 2mm scan range compared to that of the longer FL mirrors, resulting in increased EFL position variations. The model results and the experimental results with 45° and 60° angles are shown in Figures 6.8(a) and (b), respectively. In the case of 45° angle, the variation between model and experimental measurements is 29% whereas this variation is 39% in the case of 60° angle. However, with the different incident angle the result shows the same trend within the scan range. The modeling results in Section 6.3 show that the scanning system maintained a consistent SR within the 2mm scans range with an angle of *ϕ=30°*. Therefore, variations of the imaging quality can be reduced by using a lower angle of '*ϕ*', as discussed in Section 6.3.2.

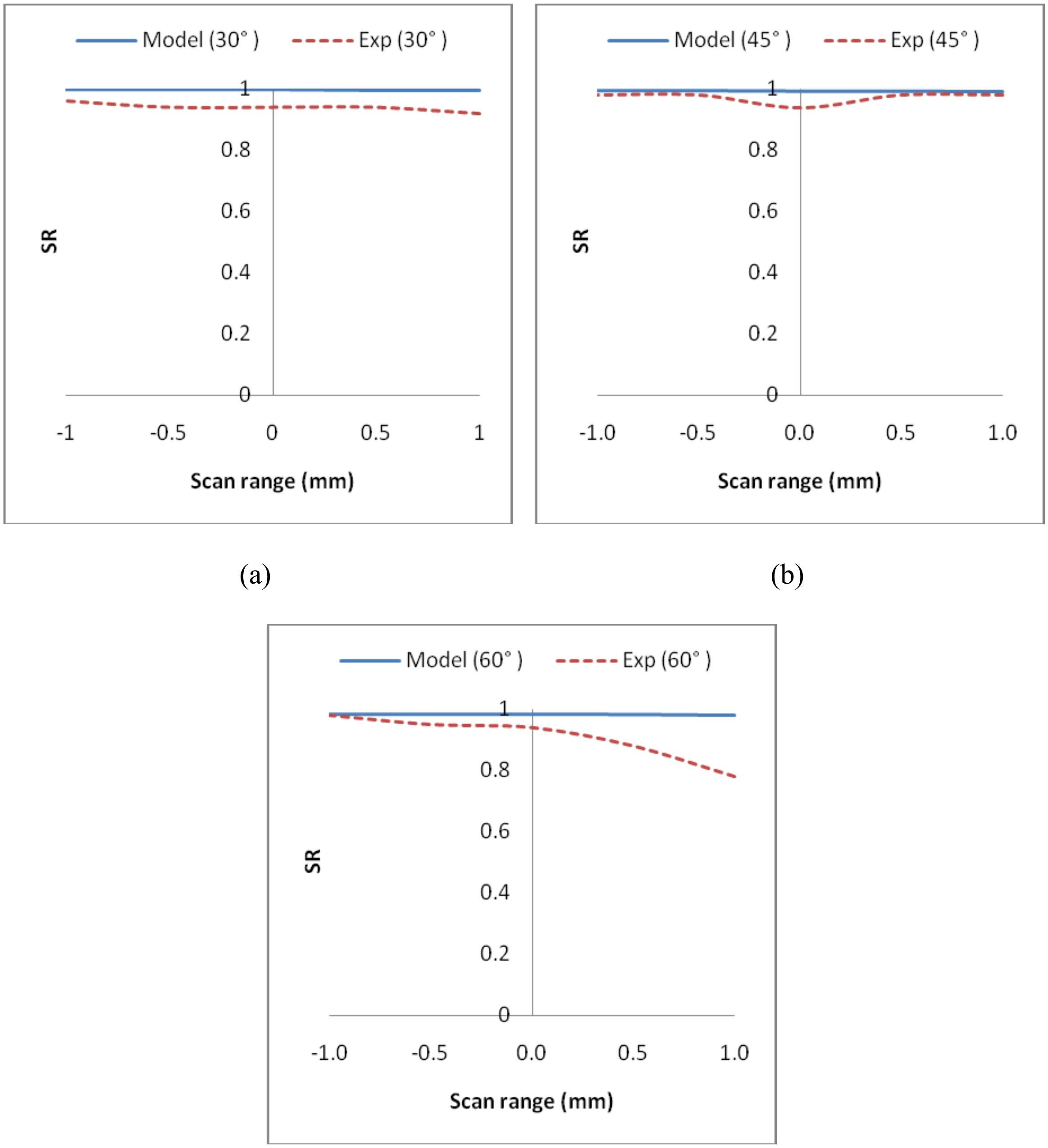

(a)

(b)

(c)

Figure 6.9: SR comparison of 51.7mm FL mirror with the angle of (a) *ϕ=30°* (b) *ϕ=45°,* and (c) *ϕ=60°*.

The experiments were performed in a free space optics system, where the system geometric parameters such as the distance *'d'*, the angle '*ϕ'* and the ROC, were restricted by the size of the optics and that of the CCD camera. However, in the real imaging system scanning would be performed on the sample instead of on the CCD camera, and the scanning mirror can be replaced by a MEMS mirror. Design of a miniature scanning system was reported in our earlier work [90]. The mirror distance of *d=10mm* and the angle of *ϕ=20°* with the 14.95mm FL mirror were used in the miniature scanning system simulation. With these parameters, the scanning system maintained an SR more than 0.97 throughout the 2mm scan range. Therefore, the developed scanning can be used in endoscopic OCT imaging as well as in external OCT imaging applications with a higher transverse resolution.

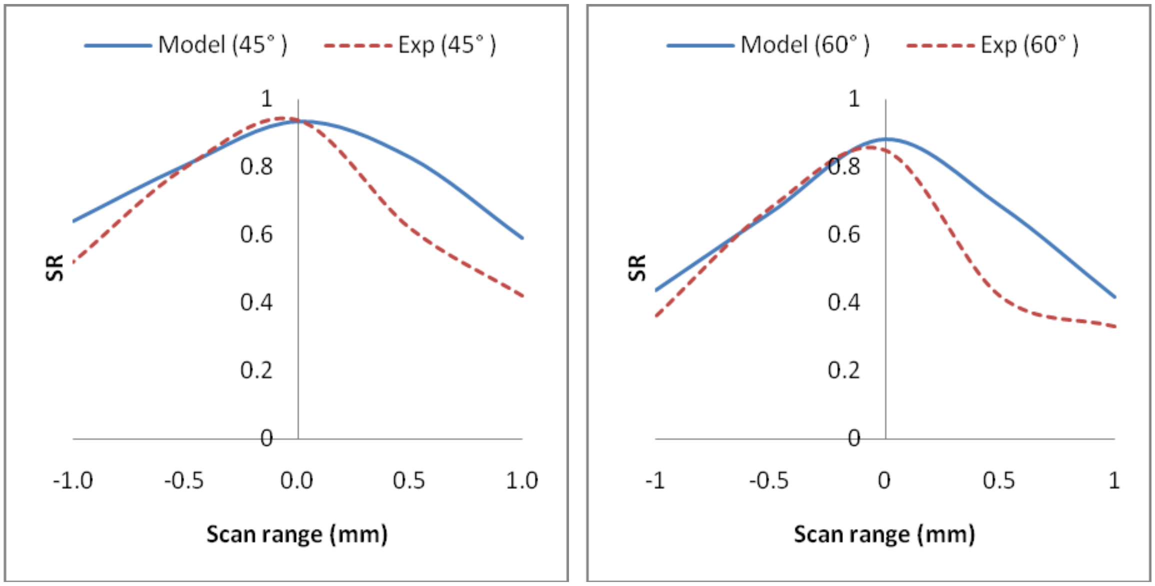

(a) (b)

Figure 6.10: SR comparison for 25.85mm FL mirror with the angle of (a) *ϕ=45°* and (b) *ϕ=60°*.

6.5.2 Flatness evaluation with X-scan system configuration

X-scanning was performed to evaluate the effect of the scanning direction on the flatness of the scan field. The ZEMAX optical design software does not permit changing the scanning as well as the focusing direction for this off-axis scanning system configuration. Thus, the flatness of the scan field was experimentally evaluated by using an X-scan. For this set of experiments, same system parameters that were used in the optical model and in the Y-scan configuration were repeated. X-scans were performed by changing the focusing and the scanning direction from the Y-axis to the X-axis. When the scanning direction was changed from Y to X, the scanning was performed in the orthogonal plane with respect to the incident beam. Because of that the incident angle ϕ does not have any influence on the angular variations during the scanning. Hence, the EFL positions vary as a function of the scan angle. The incident angles of 30°, 45° and 60°were used with the 51.7mm FL mirror. Because of the experimental constraints, in the case of the 25.85mm FL mirror, the experiments were limited to the incident angles of 45° and 60°. Experiments were performed by positioning the beam at the center (C) of the mirrors. Five beam profiles were captured within the 2mm scan range, and then the profiles were processed to extract the SR value. Comparisons of the SR for the beam position at C are shown in Figures 6.11 (a) and (b) for the 51.7mm FL mirror and for the 25.85mm FL mirror, respectively. The experimental results show that the SR maintained above the Marechal criteria of 0.8 throughout the 2mm scan range regardless of the focal length and the incident angle.

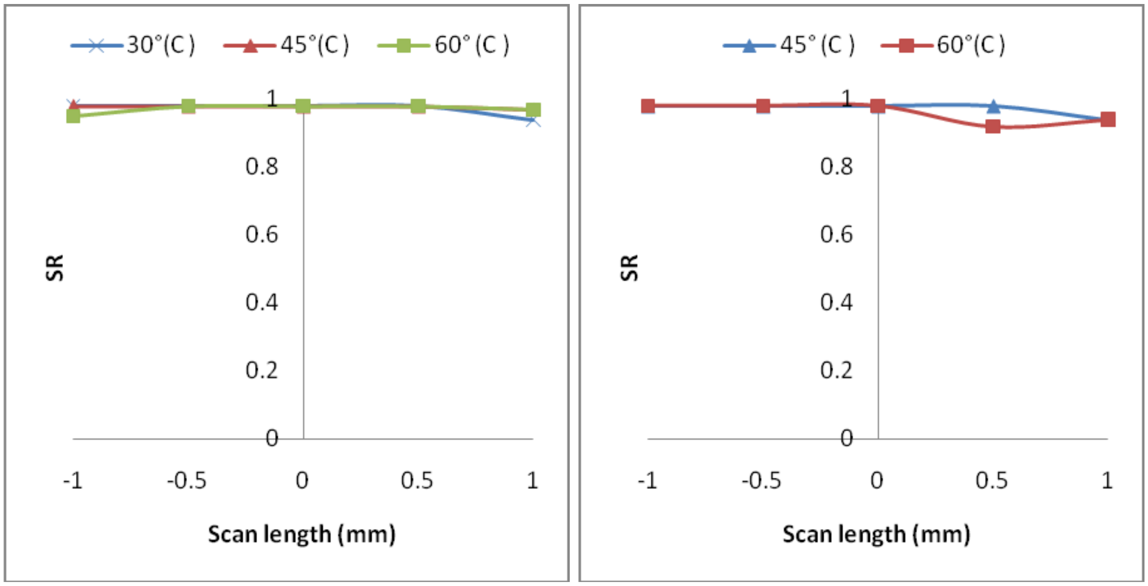

(a) (b)

Figure 6.11: X-scan SR comparison with the beam position at C for (a) 51.7mm, and (b) 25.85mm FL mirror.

Two off-set positions on the cylindrical mirrors were used to evaluate the sensitivity of the scanning system to variations in beam positioning. For both mirrors, a 1mm off-set from the center (C+1) and a 2mm off-set from the center (C+2) were studied. Five beam profiles were recorded within the 2mm scan range for each off-set position. The SR comparisons of these beam positions are shown in Figures 6.10 and 6.11 respectively. Experimental results show that the SR maintained above the Marechal criterion throughout the 2mm scan range regardless of the beam position, the incident angle, and the radius of curvatures. Therefore, the developed scanning system provides flat scan field by maintaining consistent SRs throughout the 2mm scan range.

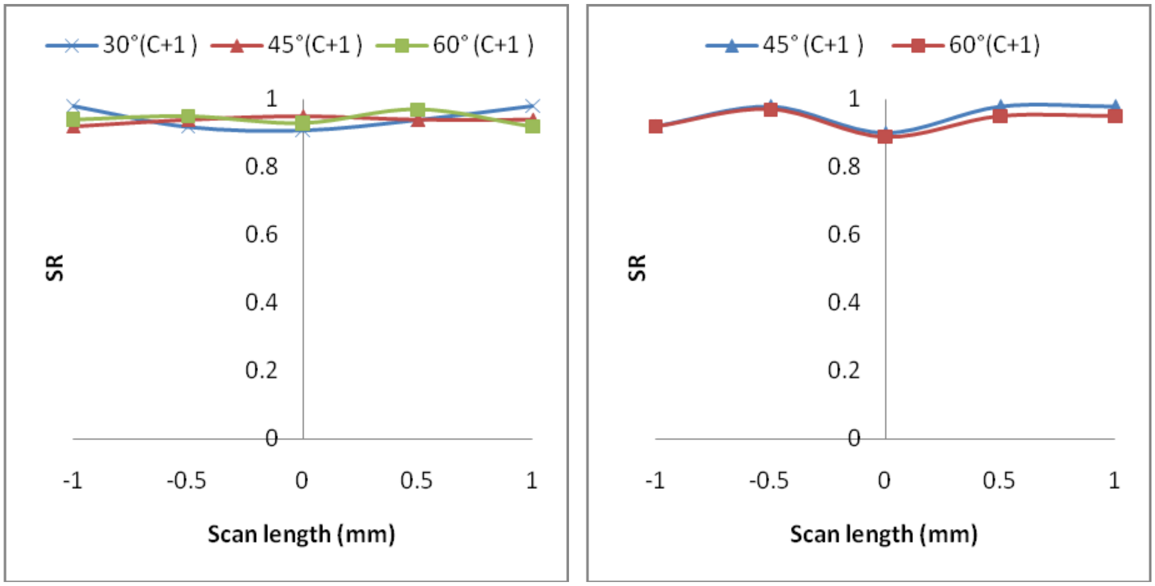

(a) (b)

Figure 6.12: X-scan SR comparison with the beam position at C+1 for (a) a 51.7mm FL mirror and (b) 25.85mm FL mirror.

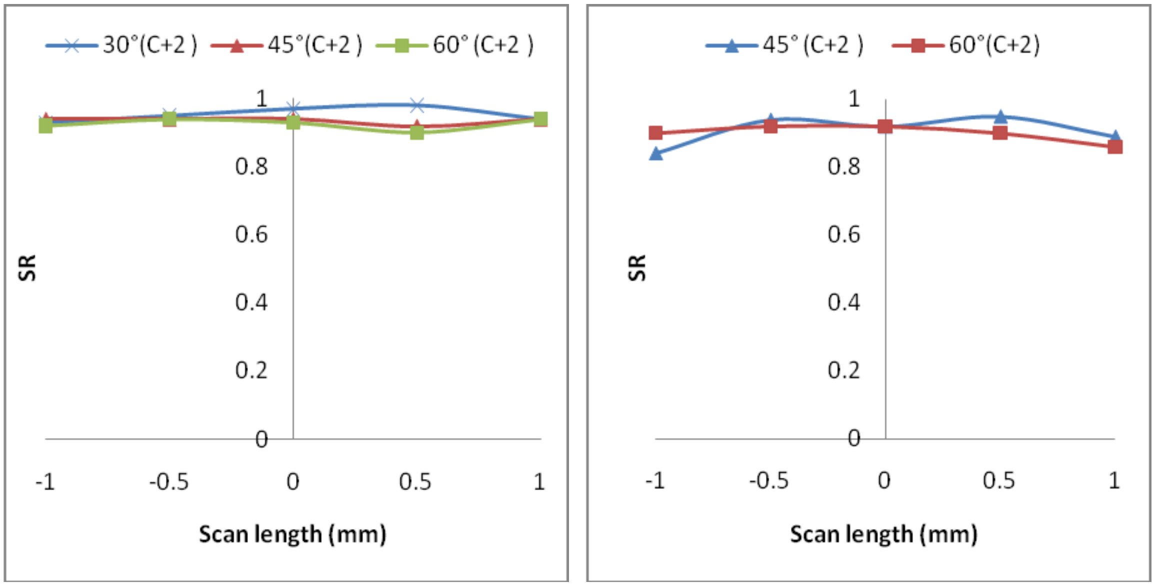

(a) (b)

Figure 6.13: X-scan SR comparison with the beam position at C+ for (a) 51.7mm FL mirror and (b) 25.85mm FL mirror.

3D beam profiles from the Y-scan and from the X-scan made by using a 51.7mm FL mirror and a 25.85mm FL mirror are shown in Figure 6.14 and Figure 6.15 respectively. In the case of the 51.7mm FL mirror, the beam profiles show consistency throughout the 2mm scan range in both scanning directions. In the case of the 25.85mm FL mirror, the beam profile lost consistency towards the ends of the 2mm scan range when using the Y-scan system configuration. The reason for this loss is attributed to the higher angular variation with respect to the angle between the incident and the reflected beam for the same scan field of 2mm. In the case of the X-scan system configuration, the beam profiles maintained consistency throughout the 2mm scan range. In this configuration, the scanning was performed in the orthogonal plane with respect to the incident beam. Therefore, the incident angle does not have any impact on the angular variation.

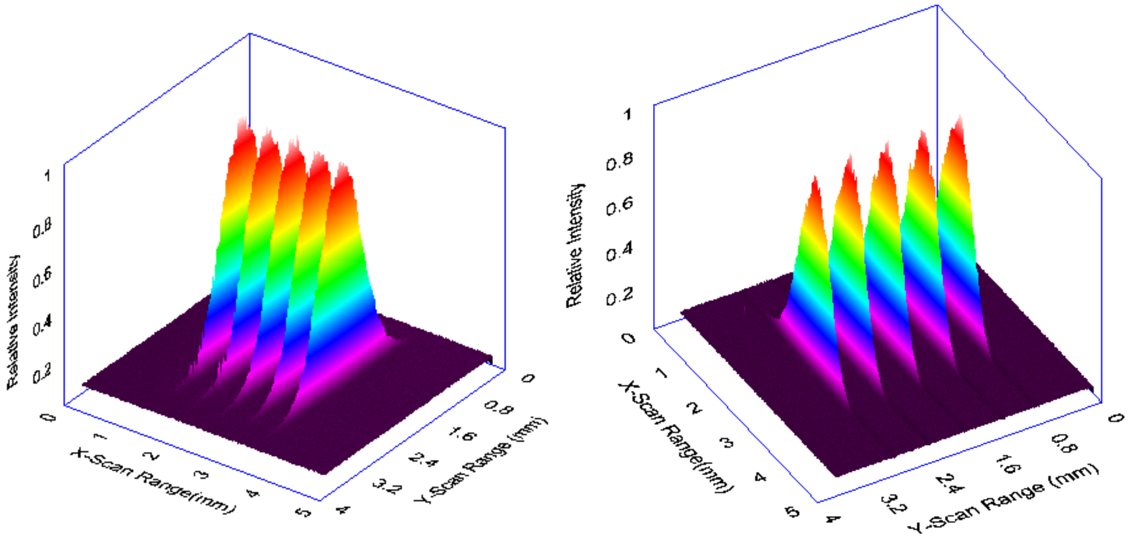

(a) (b)

Figure 6.14: 3D map of 51.7mm FL mirror with $\phi=60^\circ$ (a) Y-scan and (b) X-scan configuration.

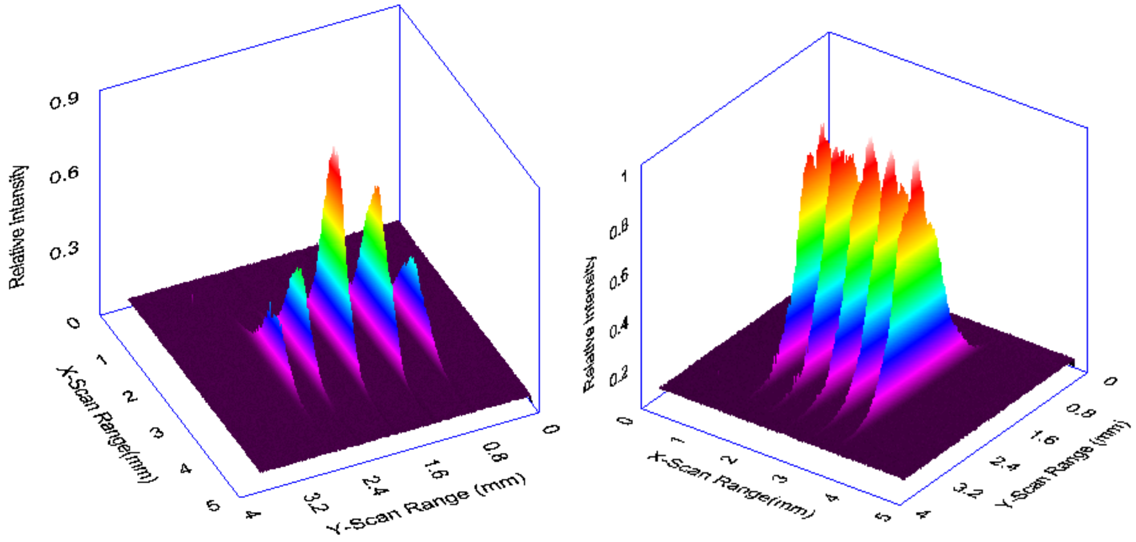

(a) (b)

Figure 6.15: 3D map of 25.85mm FL mirror with $\phi=60°$ (a) Y-scan and (b) X-scan configuration.

6.6 Transverse resolution comparison

The shape and the size of the spread function determine the transverse resolution. Imaging quality depends on the consistency of the transverse resolution throughout the scan range. Transverse resolution in the line focusing direction is quantified by using the full-width-at-half-maximum (FWHM) of the spread function. Therefore, a consistent FWHM is required to achieve a flat scan field image. To evaluate the effect of the scan direction on the FWHM, the spread function was extracted from five beam profiles. Figure 6.16 shows the spread function at five scan positions within a 2mm scan range using the 25.85mm FL mirror at the angle $\phi=45°$. In the case of the X-scan, a 15µm transverse resolution is maintained throughout the 2mm scan range. In the case of the Y-scan, a 15μm transverse resolution was achieved only at the centre of the scan field. It drops significantly towards the ends of the scan field.

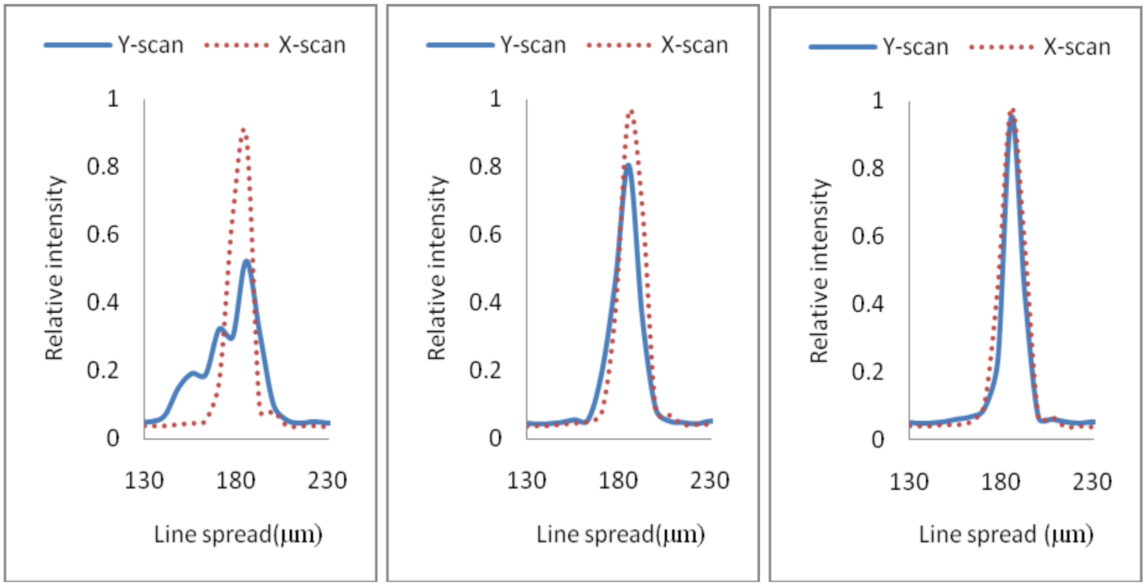

(a) -1mm (b) -0.5mm (c) 0mm

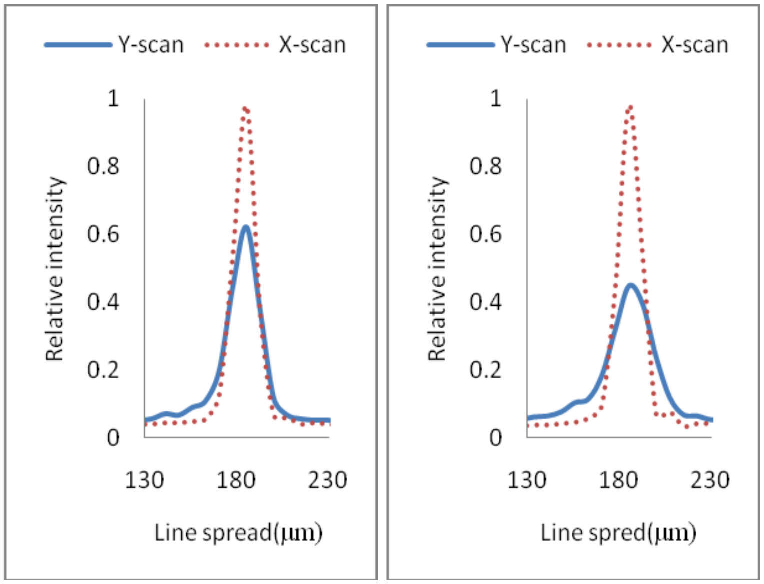

(d) 0.5mm (e) 1mm

Figure 6.16: X-scan and Y-scan transverse resolution within 2mm scan range at different scan positions.

6.7 Conclusions

A robust line-scanning system has been demonstrated by using cylindrical mirror focusing. A 53nm spectral bandwidth light source with a centre wavelength of 843nm was used in the developed scanning system. A 25.85mm focal-length cylindrical mirror and a 51.7mm focal-length cylindrical mirror were used to focus a 2mm collimated beam. The effect of the angle between the incident beam and the reflected beam and the distance between the mirrors was studied. The flatness of the scan field was demonstrated by using tangential scanning. For high-performance imaging with the developed system, the geometric parameters of the scanning system, such as the angle between the incident beam and the reflected beam should be as low as the design would permit and the distance between the mirrors should be smaller than or equal to the focal length of the cylindrical mirror. The improvement of the imaging performance by using sagittal scanning was demonstrated and proved that sagittal scanning provides robust performance regardless of the scanning system parameters and beam off-set.

Chapter 7: Conclusions and future studies

7.1 Conclusions

The main objective of this thesis work is to develop a reflective optics-based line-scan SD-OCT for high-quality imaging at high-speeds for endoscopic applications. The proposed objectives have been achieved in this research, as reflective optics based novel line scanning system has been developed. Analytical models and optical designs of scanning system and spectrometer were explored in this thesis study. This thesis study explored the utilization of reflective optics in optical coherence tomography for high imaging performance. Significant advantages of the reflective optics focusing compared to that of refractive optics focusing with respect to chromatic aberration, scan field flatness, and uniformity of imaging quality over a fixed scan range were established through optical simulation and experimental verification. An off-axis cylindrical mirror has been used for line field focusing in the scanning system and in the spectrometer. Refractive optics scanning system by using plano-convex cylindrical lens and achromatic cylindrical lens are designed to compare the performance with reflective optics focusing system. Strehl ratio (SR) of 0.8, which is the Marechal criteria for a good quality optical system, was used as a benchmark for performance comparisons and experimental validations.

- The literature review examined the overview of the medical imaging and the state-of-the-art of OCT imaging. Subsequently, different types OCT systems, scanning protocols, and system design requirements have been reviewed. Flying spot vs. line scanning and refractive vs. reflective optics system were then reviewed in relation to the imaging quality of the OCT imaging. It was concluded that the focusing lens in the scanner arm and in the spectrometer are the primary limitations to achieve high-quality imaging with SD-OCT.

- To overcome the limitations of the lens focusing system, cylindrical mirror focusing was proposed. The main benefit of the cylindrical mirror focusing is the insensitivity to the broader spectral bandwidth. Mirror focusing eliminates the chromatic aberration and provides uniform imaging quality within the design scan range.
- Mathematical model of an off-axis cylindrical mirror focused line scanning system has been developed and scan field flatness was evaluated using ZEMAX optical design software. In the optical model, a 2mm collimated beam is focused as a line by using cylindrical optics and 100nm spectral bandwidth light source was used. The effective focal plane variation of 9µm was demonstrated from the optical model within the 3.2mm scan range.
- Imaging quality was compared between the refractive optics and reflective optics focused scanning systems. A plano-convex cylindrical lens and an achromatic cylindrical lens were used in the refractive optics scanning system configuration while a cylindrical mirror was used in the reflective optics configuration. The effective focal lengths of 12.7mm, 25.4mm, and 51.8mm were used for performance comparisons. The scanning system was designed for 2mm by 2mm scan range with a light source of 200nm spectral band width. Model results

proved that, Strehl ratio drops rapidly in the case of the plano-convex cylindrical lens focusing while the cylindrical mirror focusing system maintains high Strehl ratio. On the other hand, achromatic cylindrical lens provided higher Strehl ratio when the beam is on the optical axis, while it reduces rapidly towards the lens edges especially in the case of higher transverse resolution where lower focal length lenses are employed. Due to its insensitivity to the broadband spectrum, the mirror focused scanners provide zero chromatic focal shifts. Moreover, in the case of the beam off-set from the center of the focusing optics, the mirror focused scanner provides better performance. From the modeling results, it was concluded that for high quality imaging in OCT an off-axis cylindrical mirror scanner is an effective alternative to complex lens scanning systems.

- With similar optical elements used in the scanning system, refractive optics and reflective optics based spectrometers were designed and their imaging performance was compared. 2mm, 3mm, and 4mm collimated beams were used to compare imaging quality at different transverse resolutions. Transverse resolution in the line direction with these beams is 10μm, 4.44μm and 2.25μm respectively. Model results proved that at a high transverse resolution, the performance drops significantly in the case of plano-convex cylindrical lens focused spectrometer. For example, in case of the 2.25μm transverse resolution, the SR drops by 48% from 830nm to 730nm and by 78% from 830nm to 930nm wavelength range. In case of the achromatic cylindrical lens spectrometer, the SR drops by 41% from 830nm to 730nm and by 51% from 830nm to 930nm wavelength range. Whereas reflective optics focused spectrometer maintains an SR more than 0.9 for the wavelength range of 730nm to 930nm regardless of the transverse resolution. The depth scan range with this spectrometer configuration is 1.7mm and spectral resolution is 0.1nm. Analytical model and signal processing of the line-scan SD-OCT were demonstrated. From the analytical model, the importance of the quality of the LSF to signal sensitivity fall-off has been ascertained and it was proved that the reflective optics spectrometer's performance is superior to that of the refractive optics spectrometer.

- Performance analysis from the optical models proved that the cylindrical mirror focusing is robust either compared to the plano-convex cylindrical lens or compared to the achromatic cylindrical lens. Moreover, the cost of the cylindrical mirror is lesser compared to the custom-made achromatic lens for high-quality imaging.
- To validate the optical model, an experimental setup consisting of a broadband light source, fiber optic collimator, scanner mirror and a cylindrical focusing mirror together with a CCD camera for analysis of the Strehl ratio was constructed. A LabVIEW based software program was developed to analyze the focused line spread function from the CCD image. A 53nm spectral bandwidth light source with cylindrical mirrors of 25.85mm and 51.7mm focal lengths were used in the modified model and experimental validation. To prove the effectiveness of the cylindrical mirror focusing manual scanning was performed. The model and experimental results showed good agreement.

- To evaluate the robustness of the developed scanning system, the effects of the geometric parameters of the scanning system on the imaging quality were studied. The effects of the angle between of the incident and reflected beams, the distance between the mirrors, and the focal length of the cylindrical mirror, on the flatness of the scan field were demonstrated, and the design parameters were identified.
- In addition, the effect of the scanning direction on the imaging quality of the LS OCT was also studied in order to evaluate the scan field flatness. The improvement of the imaging performance by using sagittal scanning was demonstrated and proved that sagittal scanning provides robust performance regardless of the scanning system parameters.
- The robustness of the developed scanning system to variations in beam position was studied theoretically for the lens and the mirror focused scanning systems. For this, an incident beam was off-set by 1mm and 2mm from the center of the lens/mirror focus and the imaging performance was compared. It was proved that the mirror focusing is insensitive to variations in beam position. It was also experimentally verified for the proposed scanning system.

7.2 Future studies

The main objective of this research was to develop a reflective optics-based endoscopic line-scan OCT imaging system. A novel line scanning system and a reflective optics based spectrometer was demonstrated in this thesis to improve the quality of OCT imaging at high speed. The scanning system would also be useful in the time-domain OCT (TD-OCT) as well as in the swept source OCT (SS-OCT) imaging. Reflective optics based spectrometers are used widely in spectral interferometric instruments. The designed cylindrical mirror based spectrometer could be integrated with the cylindrical mirror focused line scanning system to build reflective optics based OCT system for high imaging quality. To build a complete endoscopic LS-OCT system and utilize the state-of-the-art of the reflective-optics focusing, following improvements are required:

- Replace manual scanning mirror with a MEMS mirror for high-speed scanning.
- In order to build miniature endoscopic probe, integrate the fiber optic beam collimator, the MEMS mirror scanner, and the cylindrical mirror in a single platform.
- Integrate the developed scanning system and designed spectrometer to build the complete line-scan SD-OCT imaging system.
- Finally, a graphical user software interface is required to operate the MEMS mirror, capture and process OCT signal.

Appendix A

A.1 Line-scan SD-OCT signal processing algorithm

In flying spot SD-OCT, the spectrally encoded interference data recorded by using a line scan camera, and then resampled into the wave number space. The axial profile can be obtained by Fourier Transformation (FT) of the resampled spectrum [31, 36-38, 113, 114].

On the other hand, in line-scan SD-OCT, spectral signal obtained in an area scan CCD detector as a 2D array. Recorded signal can be processed by performing 1D FT or it can be processed by performing a 2D FT [115]. Signal processing flow chart of the line-scan SD-OCT is shown in Figure A.1. In the case of 1D FT, the 2D signal array is required to be divided into multiples of 1D array in the line direction. The resultant 1D array contains the similar spectral intensity data that is acquired by using a flying spot scanning. Therefore, these 1D arrays can be processed by using the same algorithm that has been used in the flying spot scanning [31, 36-38, 113, 114] and then combined together to create a 3D OCT image. Signal processing using LabVIEW based program for flying spot SD-OCT has been reported recently [114, 116]. In the following section, the methodology of depth profile generation from the sample is demonstrated.

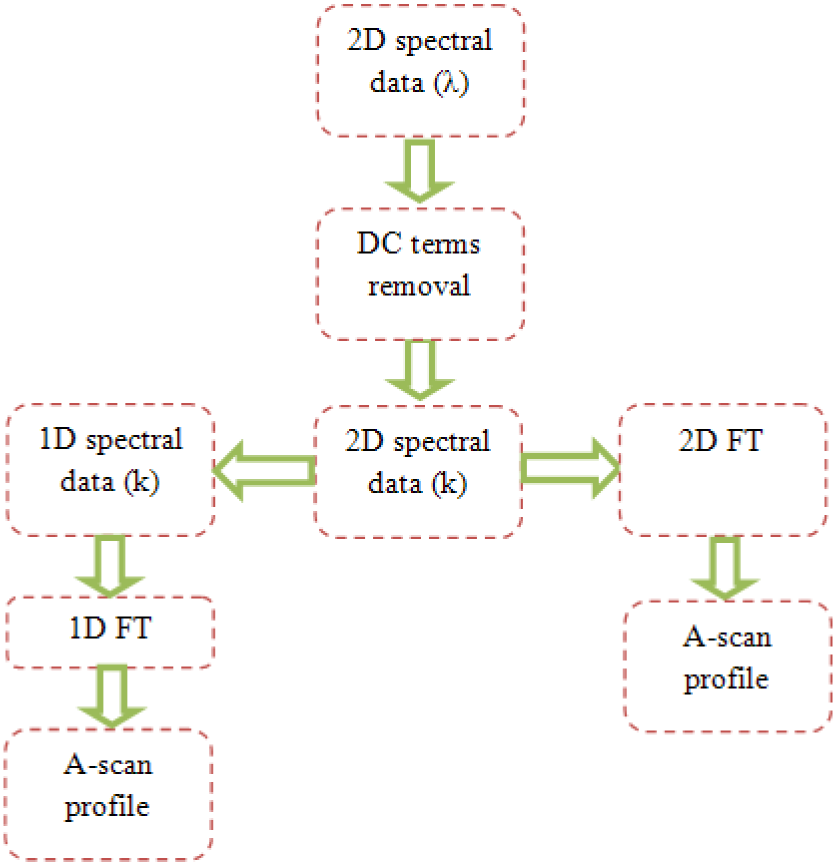

Figure A.1: Flow chart of the line-scan SD-OCT data processing.

A.2 1D FT based A-scan profile

As discussed in Section 4.4, in line-scan SD OCT, the intensity distribution in the line direction has no influence on the interference signal. Therefore, divisions of acquired 2D array in the line direction will not affect the interference signal that contains the depth information. Interference signal and the resultant A-scan profiles for different depths were simulated by using the modified LabVIEW program that was developed by Xi P. Et al., [114]. An 843nm center wavelength light source with a FWHM spectral bandwidth of 53nm that was utilized in the experimentation in Chapters 5 and 6 of this thesis is used in the following simulation. The spectral range of this source is from 800nm to 880nm. The spectral intensity distribution of the SLD source is shown in Figure A.2. This spectral range is covered by 2048 CCD pixels with a spectral resolution of 0.08nm and resultant depth scan range is ~2mm. A-scan profiles were simulated for four defined depth locations within the 2mm scan range. Assumed reflectivity at different depths is shown Table A.1

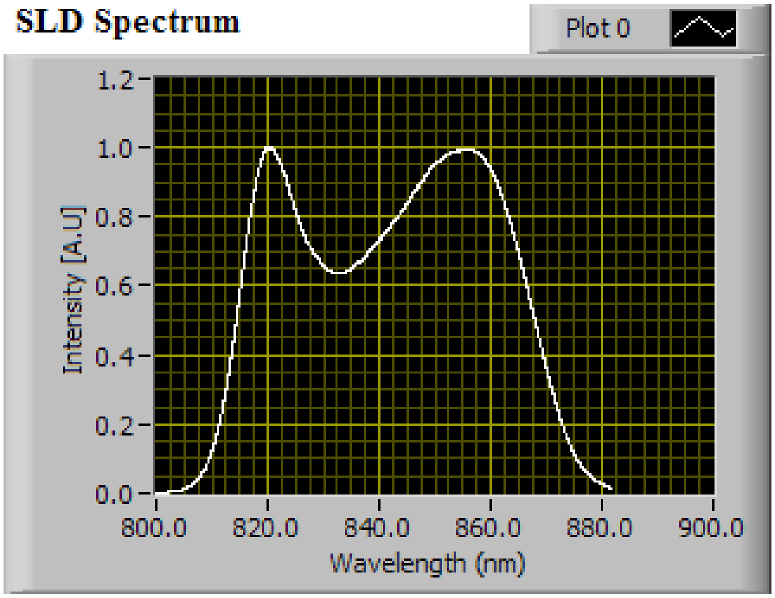

Figure A.2: SLD spectrum profile

The simulated interference signals and A-scan profiles are shown in Figure A.3 to Figure A.6. Simulation result shows that the signal is attenuated with the increasing of the depth location. This attenuation is dependent on the spectral bandwidth integrated by individual pixels as well as the spectrometer optics [114]. This depth dependent signal attenuation is known as sensitivity fall-off and its limits depth scan range of the OCT imaging.

Recently, non-uniform Fast Fourier transform (NUFFT) has been demonstrated and it shows OCT signal quality improvement by using this processing method [38]. 1D FT based signal processing is demonstrated in this section for four depth locations within a single position on the focused line. By applying the same process the rest of the positions can be processed and then combined to perform 3D imaging.

Table A.1: Input data of the A-scan profiles simulation

Depth (µm)	Reflectivity
100	0.9
500	0.7
1000	0.4
1500	0.2

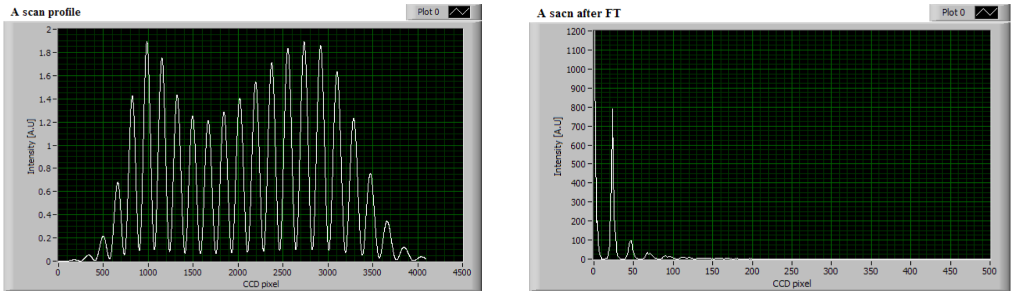

(a) (b)

Figure A.3: a) Interference signal and b) A-scan profile at 100µm depth.

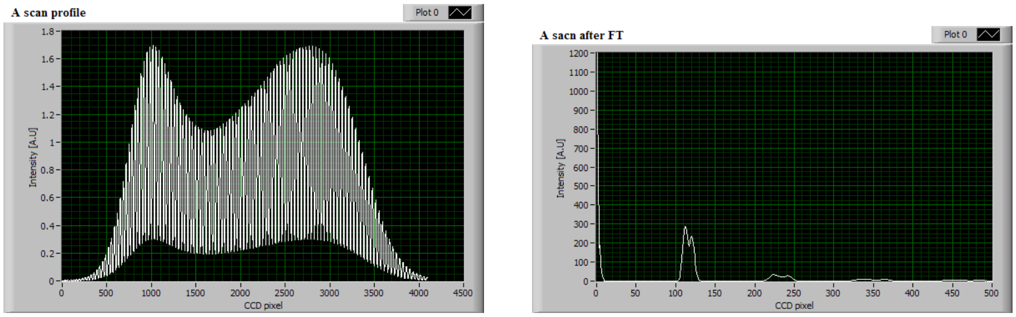

(a) (b)

Figure A.4: a) Interference signal and b) A-scan profile at 500µm depth.

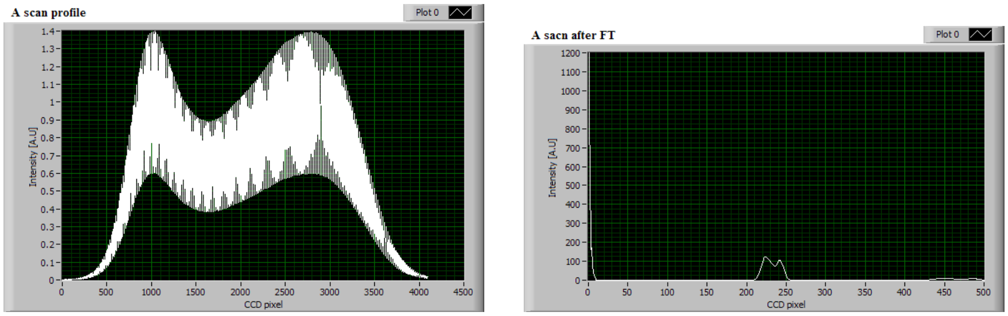

(a) (b)

Figure A.5: a) Interference signal and b) A-scan profile at 1000µm depth.

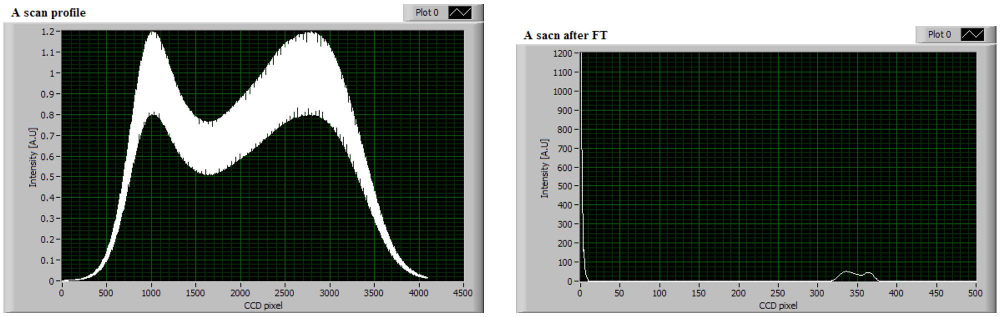

(a) (b)

Figure A.6: a) Interference signal and b) A-scan profile at 1500µm depth.

References

1. W. Drexler and J. G. Fujimoto, eds., *Optical Coherence Tomography -Technology and Applications* (Springer, 2008).
2. B. Qi, A. Phillip Himmer, L. Maggie Gordon, X. D. Victor Yang, L. David Dickensheets, and I. Alex Vitkin, "Dynamic focus control in high-speed optical coherence tomography based on a microelectromechanical mirror," Optics Communications **232,** 123-128 (2004).
3. S. Chang, Y. Mao, C. Flueraru, and S. Sherif, "Optical coherence tomography: technology and applications," in Y. Sheng, Y. Wang, and L. Zeng, eds. (SPIE, 2008), pp. 715606.
4. D. Huang, E. Swanson, C. Lin, J. Schuman, W. Stinson, W. Chang, M. Hee, T. Flotte, K. Gregory, C. Puliafito, and Fujimoto J., "Optical coherence tomography," Science **254,** 1178-1181 (1991).
5. B. Potsaid, I. Gorczynska, V. J. Srinivasan, Y. Chen, J. Jiang, A. Cable, and J. G. Fujimoto, "Ultrahigh speed spectral / Fourier domain OCT ophthalmic imaging at 70,000 to 312,500 axial scans per second," Optics Express **16,** 15149-15169 (2008).
6. T. E. Ustun, N. V. Iftimia, R. D. Ferguson, and D. X. Hammer, "Real-time processing for Fourier domain optical coherence tomography using a field programmable gate array," Rev. Sci. Instrum. **79,** 114301 (10 pp.) (2008).
7. T. S. Ralston, J. A. Mayen, D. Marks, and S. A. Boppart, "Real-time digital design for an optical coherence tomography acquisition and processing system," in *Three-Dimensional and Multidimensional Microscopy: Image Acquisition and*

Processing XI, Anonymous (International Society for Optical Engineering, 2004), pp. 159-170.

8. N. M. Shakhova, V. M. Gelikonov, V. A. Kamensky, R. V. Kuranov, and I. V. Turchin, "Clinical aspects of the endoscopic optical coherence tomography and the ways for improving its diagnostic value," in *Tenth International Laser Physics Workshop (LPHYS'01),* Anonymous (MAIK Nauka/Interperiodica Publishing, 2002), pp. 617-26.
9. J. Colston Bill W., M. J. Everett, L. B. Da Silva, L. L. Otis, P. Stroeve, and H. Nathel, "Imaging of Hard- and Soft-Tissue Structure in the Oral Cavity by Optical Coherence Tomography," Appl. Opt. **37,** 3582-3585 (1998).
10. C. Pitris, C. Jesser, S. A. Boppart, D. Stamper, M. E. Brezinski, and J. G. Fujimoto, "Feasibility of optical coherence tomography for high-resolution imaging of human gastrointestinal tract malignancies," J. Gastroenterol. **35,** 87-92 (2000).
11. M. E. Brezinski, G. J. Tearney, B. E. Bouma, J. A. Izatt, M. R. Hee, E. A. Swanson, J. F. Southern, and J. G. Fujimoto, "Optical Coherence Tomography for Optical Biopsy : Properties and Demonstration of Vascular Pathology," Circulation **93,** 1206-1213 (1996).
12. A. Podoleanu, J. Rogers, D. Jackson, and S. Dunne, "Three dimensional OCT images from retina and skin," Opt. Express **7,** 292-298 (2000).
13. C. Pitiris, M. E. Brezinski, B. E. Bouma, G. J. Tearney, J. F. Southern, and J. G. Fujimoto, "High Resolution Imaging of the Upper Respiratory Tract with Optical

Coherence Tomography . A Feasibility Study," Am. J. Respir. Crit. Care Med. **157,** 1640-1644 (1998).

14. A. F. Zuluaga, M. Follen, I. Boiko, A. Malpica, and R. Richards-Kortum, "Optical coherence tomography: A pilot study of a new imaging technique for noninvasive examination of cervical tissue," American Journal of Obstetrics and Gynecology **193,** 83-88 (2005).
15. Y. Yang, A. Dubois, X. Qin, J. Li, A. E. Haj, and R. K. Wang, "Investigation of optical coherence tomography as an imaging modality in tissue engineering," Phys. Med. Biol. **51,** 1649-1659 (2006).
16. Y. Yang, R. K. Wang, E. Guyot, A. E. Haj, and A. Dubois, "Application of optical coherence tomography for tissue engineering," in *Coherence Domain Optical Methods and Optical Coherence Tomography in Biomedicine IX,* Anonymous (SPIE-Int. Soc. Opt. Eng, 2005), pp. 18-23.
17. A. Sergeev, V. Gelikonov, G. Gelikonov, F. Feldchtein, R. Kuranov, N. Gladkova, N. Shakhova, L. Snopova, A. Shakhov, I. Kuznetzova, A. Denisenko, V. Pochinko, Y. Chumakov, and O. Streltzova, "In vivo endoscopic OCT imaging of precancer and cancer states of human mucosa," Opt. Express **1,** 432-440 (1997).
18. T. Xie, H. Xie, G. K. Fedder, M. Zeidel, and Y. Pan, "Endoscopic optical coherence tomography with a micromachined mirror," Microtechnologies in Medicine & Biology 2nd Annual International IEEE-EMB Special Topic Conference on208-211 (2002).

19. J. G. Fujimoto, S. A. Boppart, G. J. Tearney, B. E. Bouma, C. Pitris, and M. E. Brezinski, "High resolution in vivo intra-arterial imaging with optical coherence tomography," Heart; Heart **82,** 128-133 (1999).

20. P. Targowski, M. Góra, and M. Wojtkowski, "Optical Coherence Tomography for Artwork Diagnostics," Laser Chemistry **Volume 2006,** (2006).

21. B. J. Rouba, P. Karaszkiewicz, L. Tymińska-Widmer, M. Iwanicka, M. Góra, E. Kwiatkowska, P. Targowski, "Optical Coherence Tomography for Non-destructive infestations of structure of objects of art " in *9th International Conference on NDT of Art,* Anonymous (2008).

22. J. P. Dunkers, F. R. Phelan, D. P. Sanders, M. J. Everett, W. H. Green, D. L. Hunston, and R. S. Parnas, "The application of optical coherence tomography to problems in polymer matrix composites," Optics and Lasers in Engineering **35,** 135-147 (2001).

23. D. Stifter, K. Wiesauer, M. Wurm, E. Schlotthauer, J. Kastner, M. Pircher, E. Gotzinger, and C. K. Hitzenberger, "Investigation of polymer and polymer/fibre composite materials with optical coherence tomography," Measurement Science and Technology **19,** 074011 (2008).

24. E. A. Swanson, M. R. Hee, G. J. Tearney, and J. G. Fujimoto, "Application of optical coherence tomography in nondestructive evaluation of material microstructure," Pacific Rim Conference on Lasers and Electro-Optics, CLEO - Technical Digest326-327 (1996).

25. F. Feldchtein, G. Gelikonov, V. Gelikonov, R. Kuranov, A. Sergeev, N. Gladkova, A. Shakhov, N. Shakhova, L. Snopova, A. Terent'eva, E. Zagainova,

Y. Chumakov, and I. Kuznetzova, "Endoscopic applicationsof optical coherence tomography," Opt. Express **3,** 257-270 (1998).

26. G. J. Tearney, M. E. Brezinski, B. E. Bouma, S. A. Boppart, C. Pitris, J. F. Southern, and J. G. Fujimoto, "In Vivo Endoscopic Optical Biopsy with Optical Coherence Tomography," Science **276,** 2037-2039 (1997).
27. Y. Pan, H. Xie, and G. K. Fedder, "Endoscopic optical coherence tomography based on a microelectromechanical mirror," Opt. Lett. **26,** 1966-1968 (2001).
28. Z. Yaqoob, J. Wu, E. J. McDowell, X. Heng, and C. Yang, "Methods and application areas of endoscopic optical coherence tomography," J. Biomed. Opt. **11,** 063001 (2006).
29. J. M. Zara and C. A. Lingley-Papadopoulos, "Endoscopic OCT Approaches Toward Cancer Diagnosis," Selected Topics in Quantum Electronics, IEEE Journal of **14,** 70-81 (2008).
30. P. H. Tomlins and R. K. Wang, "Theory, developments and applications of optical coherence tomography," J. Phys. D **38,** 2519-2535 (2005).
31. A. F. Fercher, W. Drexler, C. K. Hitzenberger, and T. Lasser, "Optical coherence tomography - principles and applications," Reports on Progress in Physics **66,** 239-303 (2003).
32. M. Brezinski, *Optical Coherence Tomograpy- Principles and Applications* (Academic Press, 2006).
33. B. E. Bouma and G. J. Tearney, ed., *Handbook of Optical Coherence Tomography* (Marcel Dekker Inc., 2001).

34. A. F. Fercher, C. K. Hitzenberger, G. Kamp, and S. Y. El-Zaiat, "Measurement of intraocular distances by backscattering spectral interferometry," Optics Communications **117,** 43-48 (1995).

35. B. Cense, N. Nassif, T. Chen, M. Pierce, S. Yun, B. Park, B. Bouma, G. Tearney, and J. de Boer, "Ultrahigh-resolution high-speed retinal imaging using spectral-domain optical coherence tomography," Opt. Express **12,** 2435-2447 (2004).

36. Z. Hu, Y. Pan, and A. M. Rollins, "Analytical model of spectrometer-based two-beam spectral interferometry," Appl. Opt. **46,** 8499-8505 (2007).

37. K. Wang, Z. Ding, T. Wu, C. Wang, J. Meng, M. Chen, and L. Xu, "Development of a non-uniform discrete Fourier transform based high speed spectral domain optical coherence tomography system," Optics Express **17,** 12121-12131 (2009).

38. K. K. H. Chan and S. Tang, "High-speed spectral domain optical coherence tomography using non-uniform fast Fourier transform," Biomed. Opt. Express **1,** 1309-1319 (2010).

39. W. Drexler, "Ultrahigh-resolution optical coherence tomography," J. Biomed. Opt. **9,** 47-74 (2004).

40. K. Lee, K. P. Thompson, and J. P. Rolland, "Broadband astigmatism-corrected Czerny-Turner spectrometer," Opt. Express **18,** 23378-23384 (2010).

41. Q. Xue, S. Wang, and F. Lu, "Aberration-corrected Czerny-turner imaging spectrometer with a wide spectral region," Appl. Opt. **48,** 11-16 (2009).

42. Q. Xue, "Astigmatism-corrected Czerny-Turner imaging spectrometer for broadband spectral simultaneity," Appl. Opt. **50,** 1338-1344 (2011).

43. A. G. Podoleanu and R. B. Rosen, "Combinations of techniques in imaging the retina with high resolution," Progress in Retinal and Eye Research **27,** 464-499 (2008).

44. M. E. J. van Velthoven, D. J. Faber, F. D. Verbraak, T. G. van Leeuwen, and M. D. de Smet, "Recent developments in optical coherence tomography for imaging the retina," Progress in Retinal and Eye Research **26,** 57-77 (2007).

45. M. Chen, Y. Chen, and W. Hsiao, "Correction of field distortion of laser marking systems using surface compensation function," Optics and Lasers in Engineering **47,** 84-89 (2009).

46. S. H. Yun, G. Tearney, J. de Boer, and B. Bouma, "Motion artifacts in optical coherence tomography with frequency-domain ranging," Opt. Express **12,** 2977-2998 (2004).

47. Y. Nakamura, S. Makita, M. Yamanari, M. Itoh, T. Yatagai, and Y. Yasuno, "High-speed three-dimensional human retinal imaging by line-field spectral domain optical coherence tomography," Optics Express **15,** 7103-7116 (2007).

48. S. Lee and B. Kim, "Line-Field Optical Coherence Tomography Using Frequency-Sweeping Source," Selected Topics in Quantum Electronics, IEEE Journal of **14,** 50-55 (2008).

49. Y. Nakamura, S. Makita, M. Yamanari, Y. Yasuno, M. Itoh, and T. Yatagai, "Optimization of line-field spectral domain optical coherence tomography for in vivo high-speed 3D retinal imaging," in *Coherence Domain Optical Methods and Optical Coherence Tomography in Biomedicine XI,* Anonymous (SPIE - International Society for Optical Engineering, 2007), pp. 64291.

50. Y. Nakamura, J. Sugisaka, Y. Sando, T. Endo, M. Itoh, T. Yatagai, and Y. Yasuno, "Complex numerical processing for in-focus line-field spectral-domain optical coherence tomography," Japanese Journal of Applied Physics, Part 1 (Regular Papers, Short Notes & Review Papers) **46,** 1774-8 (2007).
51. Y. Nakamura, J. Sugisaka, Y. Yasuno, Y. Sando, T. Endo, M. Itoh, and T. Yatagai, "In-focus line field Fourier-domain optical coherence tomography by complex numerical method," in *Coherence Domain Optical Methods and Optical Coherence Tomography in Biomedicine X,* Anonymous (International Society for Optical Engineering, 2006), pp. 607916.
52. B. Grajciar, M. Pircher, A. Fercher, and R. Leitgeb, "Parallel Fourier domain optical coherence tomography for in vivo measurement of the human eye," Opt. Express **13,** 1131-1137 (2005).
53. T. Endo, Y. Yasuno, S. Makita, M. Itoh, and T. Yatagai, "Profilometry with line-field Fourier-domain interferometry," Opt. Express **13,** 695-701 (2005).
54. Y. Yasuno, Takashi Endo, S. Makita, G. Aoki, Y. Nakamura, M. Yamanari, M. Itoh, and T. Yatagai, "Dermatological Investigation by Three-Dimensional Line-Field Fourier Domain Optical Coherence Tomography," Lasers and Electro-Optics, 2005. CLEO/Pacific Rim 2005. Pacific Rim Conference on332-333 (2005).
55. T. Hillman and D. Sampson, "The effect of water dispersion and absorption on axial resolution in ultrahigh-resolution optical coherence tomography," Opt. Express **13,** 1860-1874 (2005).

56. A. Unterhuber, B. Povazay, K. Bizheva, B. Hermann, H. Sattmann, A. Stingl, T. Le, M. Seefeld, R. Menzel, M. Preusser, H. Budka, C. Schubert, H. Reitsamer, P. K. Ahnelt, J. E. Morgan, A. Cowey, and W. Drexler, "Advances in broad bandwidth light sources for ultrahigh resolution optical coherence tomography," Phys. Med. Biol. **49,** 1235-1246 (2004).
57. U. Sharma, E. W. Chang, and S. H. Yun, "Long-wavelength optical coherence tomography at 1.7 μm for enhanced imaging depth," Opt. Express **16,** 19712-19723 (2008).
58. A. V. Zyyagin, J. B. Fitzgerald, K. K. M. B. D. Silva, and D. D. Sampson, "Real-time detection technique for Doppler optical coherence tomography," Opt. Lett. **25,** 1645-7 (2000).
59. E. Goetzinger, M. Pircher, and C. K. Hitzenberger, "Polarization sensitive spectral domain optical coherence tomography," in *Optical Coherence Tomography and Coherence Techniques II, June 12, 2005 - June 16,* Anonymous (SPIE, 2005), pp. 1-4.
60. P. Meemon, K. Lee, S. Murali, and J. Rolland, "Optical design of a dynamic focus catheter for high-resolution endoscopic optical coherence tomography," Appl. Opt. **47,** 2452-2457 (2008).
61. A. D. Aguirre, P. R. Hertz, Y. Chen, J. G. Fujimoto, W. Piyawattanametha, L. Fan, and M. C. Wu, "Two-axis MEMS Scanning Catheter for Ultrahigh Resolution Three-dimensional and En Face Imaging," Opt. Express **15,** 2445-2453 (2007).

62. K. Aljasem, A. Werber, A. Seifert, and H. Zappe, "Fiber optic tunable probe for endoscopic optical coherence tomography," Journal of Optics A: Pure and Applied Optics **10,** 044012 (2008).

63. K. Aljasem, A. Werber, and H. Zappe, "Tunable endoscopic MEMS-probe for optical coherence tomography," in *2007 IEEE/LEOS International Conference on Optical MEMS and Nanophotonics, OMENS,* Anonymous (Institute of Electrical and Electronics Engineers Computer Society, 2007), pp. 8-9.

64. T. *Xie*, H. Xie, G. K. Fedder, and Y. Pan, "Endoscopic optical coherence tomography with new MEMS mirror," Electron. Lett. **39,** 1535-6 (2003).

65. P. H. *Tran*, D. S. Mukai, M. Brenner, and Z. Chen, "In vivo endoscopic optical coherence tomography by use of a rotational microelectromechanical system probe," Opt. Lett. **29,** 1236-8 (2004).

66. A. Ja*i*n, A. Kopa, Y. Pan, G. K. Fedder, and H. Xie, "A two-axis electrothermal micromirror for endoscopic optical coherence tomography," IEEE Journal of Selected Topics in Quantum Electronics **10,** 636-42 (2004).

67. K. H. Kim, B. H. Park, G. N. Maguluri, T. W. Lee, F. J. Rogomentich, M. G. Bancu, B. E. Bouma, J. F. de Boer, and J. J. Bernstein, "Two-axis magnetically-driven MEMS scanning catheter for endoscopic high-speed optical coherence tomography," Opt. Express **15,** 18130-18140 (2007).

68. A. Rollins, S. Yazdanfar, M. Kulkarni, R. Ung-Arunyawee, and J. Izatt, "In vivo video rate optical coherence tomography," Optics Express **Vol. 3,** 219-229 (1998).

69. B. Vakoc, G. Tearney, and B. Bouma, "OCT-guided laser therapy shows promise," (15 January 2009).

70. K. Kumar, J. C. Condit, A. McElroy, N. J. Kemp, K. Hoshino, T. E. Milner, and X. Zhang, "Fast 3D in vivo swept-source optical coherence tomography using a two-axis MEMS scanning micromirror," Journal of Optics A: Pure and Applied Optics **10,** 044013 (2008).

71. Y. Xu, J. Singh, C. S. Premachandran, A. Khairyanto, K. W. S. Chen, N. Chen, C. J. R. Sheppard, and M. Olivo, "Design and development of a 3D scanning MEMS OCT probe using a novel SiOB package assembly," J Micromech Microengineering **18,** 125005 (2008).

72. J. Singh, J. H. S. Teo, Y. Xu, C. S. Premachandran, N. Chen, R. Kotlanka, M. Olivo, and C. J. R. Sheppard, "A two axes scanning SOI MEMS micromirror for endoscopic bioimaging," J Micromech Microengineering **18,** 025001 (2008).

73. R. Leitgeb, C. Hitzenberger, and A. Fercher, "Performance of fourier domain vs. time domain optical coherence tomography," Opt. Express **11,** 889-894 (2003).

74. F. Fankhauser and S. Kwasniewska, ed., *Lasers in Ophthalmology—Basic, Diagnostic and Surgical Aspects A Review* (Kugler Publications, 2003).

75. Robert *Edward* Fischer, Biljana Tadic-Galeb, Paul R. Yoder, *Optical System Design* (McGraw-Hill Companies, 2008).

76. Joseph M. Geary, *Introduction to Lens Design with Practical ZEMAX Examples* (Willmann-Bell, Inc., 2002).

77. C.E. Webb and J.D.C. Jones, ed., *Handbook of Laser Technology and Applications* (Institute of Physics, 2004).

78. M. Lieb and A. Meixner, "A high numerical aperture parabolic mirror as imaging device for confocal microscopy," Opt. Express **8,** 458-474 (2001).

79. M. Kamal, S. Narayanswamy, and M. Packirisamy, "Optical design of a line-focused forward-viewing scanner for optical coherence tomography," Appl. Opt. **49,** 6170-6178 (2010).

80. Gerald F. Marshall, ed., *Handbook of Optical and Laser Scanning* (Marcel Dekker, Inc, 2004).

81. Leo Beiser, *Unified Optical Scanning Technology* (Wiley, 2003).

82. H. Ra, W. Piyawattanametha, M. J. Mandella, P. Hsiung, J. Hardy, T. D. Wang, C. H. Contag, G. S. Kino, and O. Solgaard, "Three-dimensional in vivo imaging by a handheld dual-axes confocal microscope," Optics Express **16,** 7224-7232 (2008).

83. N. D. Haig and T. L. Williams, "Psychometrically appropriate assessment of afocal optics by measurement of the Strehl intensity ratio," Appl. Opt. **34,** 1728-1740 (1995).

84. E. J. Fernandez and W. Drexler, "Influence of ocular chromatic aberration and pupil size on transverse resolution in ophthalmic adaptive optics optical coherence tomography," Optics Express **13,** 8184-8197 (2005).

85. M. Born and E. Wolf, *Principles of Optics* (Cambridge University Press, 1999).

86. M. Mujat, N. V. Iftimia, R. D. Ferguson, and D. X. Hammer, "Swept-source parallel OCT," in J. G. Fujimoto, J. A. Izatt, and V. V. Tuchin, eds. (SPIE, 2009), pp. 71681E.

87. S. Bourquin, P. Seitz, and R. P. Salathe, "Optical coherence topography based on a two-dimensional smart detector array," Opt. Lett. **26,** 512-514 (2001).

88. T. Matsuda, F. Abe, and H. Takahashi, "Laser printer scanning system with a parabolic mirror," Appl. Opt. **17,** 878-884 (1978).

89. A. Franks, K. Jackson, and A. Yacoot, "A parabolic mirror x-ray collimator," Measurement Science and Technology **11,** 484-488 (2000).

90. M. Kamal, N. Sivakumar, and M. Packirisamy, "Optical modeling of a line-scan optical coherence tomography system for high-speed three-dimensional endoscopic imaging," in R. Vallee, ed. (SPIE, 2009), pp. 738607.

91. M. Kamal, N. Sivakumar, and M. Packirisamy, "Design of a spectrometer for all-reflective optics-based line scan Fourier domain optical coherence tomography," in H. P. Schriemer and R. N. Kleiman, eds. (SPIE, 2010), pp. 775020.

92. M. Kamal, N. Sivakumar, and M. Packirisamy, "Design of spectrometer for high-speed line field optical coherence tomography," PN11-PN100-51 (SPIE, 2011) (in press).

93. M. Kamal, N. Sivakumar, and M. Packirisamy, "An off-axis cylindrical mirror focused line scanning with high imaging quality for optical coherence tomography application " J. opt. (Accepted August 22nd, 2011), Paper ID: JOPT/400149/PAP/148632.

94. M. Kamal, N. Sivakumar, and M. Packirisamy, "Optimized off-axis cylindrical mirror-focused line-scanning system for OCT imaging applications," J. Biomed. Opt. (2011), Paper ID-JBO 11373 (under review).

95. F. Lexer, C. K. Hitzenberger, W. Drexler, S. Molebny, H. Sattmann, M. Sticker, and A. F. Fercher, "Dynamic coherent focus OCT with depth-independent transversal resolution," Journal of Modern Optics **46,** 541-53 (1999).

96. A. Dubois, G. Moneron, K. Grieve, and A. C. Boccara, "Three-dimensional cellular-level imaging using full-field optical coherence tomography," Phys. Med. Biol. **49,** 1227-1234 (2004).

97. D. J. Schroeder, *Astronomical Optics* (Academic Press, 1999).

98. ZEMAX Development Corporation, "ZEMAX Optical Design Programs User's Guide," June 24, (2008**).**

99. W. R. Hendee and E. R. Ritenour, *Medical Imaging Physics* (Wiley-Liss Inc., New York, 2002).

100. B. Hermann, K. Bizheva, A. Unterhuber, B. Povazay, H. Sattmann, L. Schmetterer, A. F. Fercher, and W. Drexler, "Precision of extracting absorption profiles from weakly scattering media with spectroscopic time-domain optical coherence tomography," in Anonymous (Optical Society of America, 2004), pp. 1677-1688.

101. O. P. Kocaoglu, S. R. Uhlhorn, E. Hernandez, R. A. Juarez, R. Will, J. Parel, and F. Manns, "Simultaneous Fundus Imaging and Optical Coherence Tomography of the Mouse Retina," Invest. Ophthalmol. Vis. Sci. **48,** 1283-1289 (2007).

102. A. R. Tumlinson, J. K. Barton, J. McNally, A. Unterhuber, B. Hermann, H. Sattmann, and W. Drexler, "An achromatized endoscope for ultrahigh-resolution optical coherence tomography," in *Optical Coherence Tomography and*

Coherence Techniques II, June 12, 2005 - June 16, Anonymous (SPIE, 2005), pp. 1-7.

103. M. Subbarao, "Determining Distance from Defocused Images of Simple Objects," **89.07.20,** (1989).

104. P. N. Keliher and C. C. Wohlers, "Echelle grating spectrometers in analytical spectrometry," Anal. Chem. **48,** 333A-4, 336A, 338A, 340A (1976).

105. A. F. Fercher, "Optical coherence tomography – development, principles, applications," Zeitschrift für Medizinische Physik **20,** 251-276 (2010).

106. M. Choma, M. Sarunic, C. Yang, and J. Izatt, "Sensitivity advantage of swept source and Fourier domain optical coherence tomography," Opt. Express **11,** 2183-2189 (2003).

107. Y. Yasuno, T. Endo, S. Makita, G. Aoki, M. Itoh, and T. Yatagai, "Three-dimensional line-field Fourier domain optical coherence tomography for in vivo dermatological investigation," J. Biomed. Opt. **11,** 14014-1 (2006).

108. L. Kagemann, G. Wollstein, H. Ishikawa, R. A. Bilonick, P. M. Brennen, L. S. Folio, M. L. Gabriele, and J. S. Schuman, "Identification and Assessment of Schlemm's Canal by Spectral Domain Optical Coherence Tomography," Investigative Ophthalmology & Visual Science **09,** 4559 (2010).

109. E. J. Fernandez, A. Unterhuber, B. Povazay, B. Hermann, P. Artal, and W. Drexler, "Chromatic aberration correction of the human eye for retinal imaging in the near infrared," Optics Express **14,** 397-409 (2006).

110. S. Murali, P. Meemon, K. Lee, W. P. Kuhn, K. P. Thompson, and J. P. Rolland, "Assessment of a liquid lens enabled in vivo optical coherence microscope," Appl. Opt. **49,** D145-D156 (2010).

111. L. Beiser, *Laser Scanning Notebook* (SPIE Press, 1992).

112. E. Hecht, *Optics* (Addison-Wesley, 2002).

113. A. R. Tumlinson, B. Hofer, A. M. Winkler, B. Povazay, W. Drexler, and J. K. Barton, "Inherent homogenous media dispersion compensation in frequency domain optical coherence tomography by accurate k-sampling," Appl. Opt. **47,** 687-93 (2008).

114. P. Xi, K. Mei, T. Brauler, C. Zhou, and Q. Ren, "Evaluation of spectrometric parameters in spectral-domain optical coherence tomography," Appl. Opt. **50,** 366-372 (2011).

115. N. Shirazi, P. M. Athanas, and A. L. Abbott, "Implementation of a 2-D fast Fourier transform on an FPGA-based custom computing machine," in *Proceedings of 5th International Workshop on Field Programmable Logic and Applications,* Anonymous (Springer-Verlag, 1995), pp. 282-92.

116. X. Li, G. Shi, and Y. Zhang, "High-speed optical coherence tomography signal processing on GPU," Journal of Physics: Conference Series **277,** 012019 (7 pp.) (2011).